

University of Nevada

Reno

**Crustal Structure in the vicinity of Yucca Mountain**

A thesis submitted in partial fulfilment of the  
requirements for the degree of Master of Science,  
in Geophysics

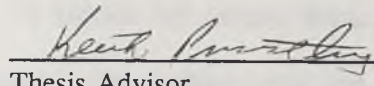
by

*Azmi Ismail*

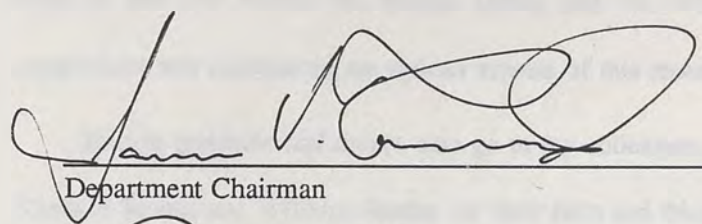
June 1986

Thesis  
2102

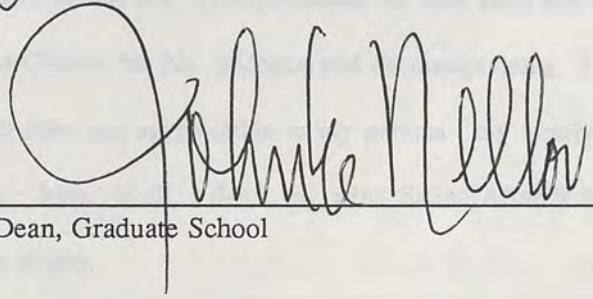
The thesis of Azmi Ismail is approved:



Thesis Advisor



Department Chairman



Dean, Graduate School

**University of Nevada  
Reno**

**June 1986**

## ACKNOWLEDGMENTS

I express my sincere thanks to Dr. Keith Priestley for the guidance and support throughout my graduate career and especially in this research project. I extend my appreciation to Dr. Ute Vetter, Dr. Robert Davis, and Dr. William Peppin for their valuable suggestions and discussions on various aspects of this research.

Sincere gratitude and thanks also go to my colleagues, Diane Martinelli, Craig dePolo, Kenneth Smith, and William Honjas for their help and friendship. My special thanks go to David Chávez for his guidance and encouragements. I especially wish to express, my sincere thanks and appreciation to my parents, my family and friends for their help and faith in me. Most of all, I thank my wife, Salina Affandi for her help, understanding and faith in my ability.

I thank the entire faculty and staff of the Seismological Laboratory, for an enriching experience.

Finally, I wish to acknowledge MARA (Malaysian Government agency) and the Nevada Nuclear Waste Project for financial support.

## ABSTRACT

The first part of the study is a review of the literature on the history of the Malay Peninsula and the development of the Malay race. The second part is a study of the Malay race in the Malay Peninsula and the Malay Archipelago. The third part is a study of the Malay race in the Malay Peninsula and the Malay Archipelago. The fourth part is a study of the Malay race in the Malay Peninsula and the Malay Archipelago.

**This thesis is dedicated to:**

**My Parents**

**Haji Ismail Abu Sittee**

**and**

**Hajjah Aminah Mohd. Yusoff**

TABLE OF CONTENTS

**ABSTRACT**

The travel times for five USGS refraction profiles in the vicinity of Yucca Mountain have been reparameterized in terms of delay time  $\tau$  and ray parameter  $p$  to obtain extremal velocity-depth bounds for the region. These bounds show a steep gradient in the shallow crust (depth  $< 5$  km) followed by a lower velocity gradient below 5 km. Specific structures along each profile, compatible with the extremal model are determined using two-dimensional ray-tracing and two-dimensional synthetic calculations. Variability in the data shows that the structure of the upper crust is highly heterogeneous. A thick, low-speed section is indicated by large delays across the Crater Flat-Prospector Pass caldera complex. A mid-crustal boundary is observed at Yucca Mountain and Skull Mountain. Other intra-crustal boundaries have also been observed between Yucca Mountain and Timber Mountain. Total crustal thickness is about 37-38 km with Moho velocity of  $7.9 \text{ km s}^{-1}$

## TABLE OF CONTENTS

<b>TITLE PAGE</b>	
<b>SIGNATURE PAGE</b> .....	i
<b>ACKNOWLEDGEMENTS</b> .....	ii
<b>DEDICATION</b> .....	iii
<b>ABSTRACT</b> .....	iv
<b>TABLE OF CONTENTS</b> .....	v
<b>INTRODUCTION</b> .....	1
<b>GEOLOGICAL AND TECTONIC SETTING</b> .....	3
<b>PREVIOUS GEOPHYSICAL WORKS</b> .....	7
<b>FIELD EXPERIMENTS</b> .....	9
<b>DATA ANALYSIS AND INTERPRETATION</b> .....	12
<b>DATA REDUCTION</b> .....	14
<b>LINE 4</b> .....	14
<b>LINE 1</b> .....	15
<b>LINE 2</b> .....	16
<b>LINE 3 WEST</b> .....	17
<b>LINE 3 EAST</b> .....	18
<b>TRAVEL-TIME ADJUSTMENTS FOR THE SHALLOW STRUCTURES</b> .....	20
<b>INTERPRETATION FROM TRAVEL TIME INVERSION OF <math>\tau(p)</math></b> .....	20
<b>DELAY-TIME METHOD</b> .....	20
<b>COMBINED DATA</b> .....	26
<b>ANALYSIS AND INTERPRETATION OF SYNTHETIC ARRIVALS</b> .....	26
<b>FINAL VELOCITY MODELS</b> .....	27
<b>LINE 1</b> .....	27
<b>LINE 2</b> .....	27
<b>LINE 3 WEST</b> .....	29
<b>LINE 3 EAST</b> .....	29
<b>LINE 4</b> .....	30
<b>DISCUSSION</b> .....	31
<b>SUMMARY AND CONCLUSIONS</b> .....	39
<b>LIST OF TABLES</b> .....	42
<b>LIST OF FIGURES</b> .....	49



## INTRODUCTION

Yucca Mountain, one of the three proposed nuclear waste repositories is located in southern Nevada, adjacent to the southwestern corner of the Nevada Test Site (NTS). Numerous geological and geophysical studies are being done to assess Yucca Mountain suitability as a nuclear waste site. During the period of 1980 to 1985, the U.S. Geological Survey (USGS) has recorded refraction data along a number of profiles in the vicinity of Yucca Mountain. Studies of the crustal structure in this region is one important element in assessing Yucca Mountain and its vicinity, as a potential site for the Nuclear Waste Repository.

Hoffman and Mooney (1984) published a preliminary report on the interpretation of (1980-1982) refraction data. In their interpretation, the USGS relied heavily on existing models and modified them to correlate with their seismic observations. The new models have been constrained by geologic and geophysical information. Hoffman and Mooney (1984) found that the greatest depth to the basement is beneath the eastern Crater Flat-western Yucca Mountain. The total crustal thickness calculated to be 35 km with intracrustal boundaries at 24 and 30 km. An additional boundary was identified at 15 km depth on the east-west profile across Yucca Mountain.

The purpose of this study is to reinterpret the data from the 1980-1982 USGS refraction experiments. Hoffman and Mooney (1984) have interpreted travel times by two-dimensional forward modeling. In this study, the travel time data will be interpreted using an inverse procedure, first proposed by Bessonova *et. al.*, (1974). This provides extremal velocity-depth bounds on the structures. These bounds will act as a guide in the two-dimensional ray-tracing of the travel time data and subsequently, in fitting the amplitudes of



the observations.

Yucca Mountain and NTS lie within the western portion of Nye County, Nevada, along the southwestern edge of Great Basin Province. A geologic map of the Yucca Mountain region is shown in Figure 2. This region is underlain by a variety of rocks distributed from Precambrian to Quaternary. According to Chappell (1972) most of the rocks of Precambrian and Early Paleozoic age in this region were deposited in a shallow water environment. This is in agreement with Stewart (1966) who states that the rocks of the Great Basin are continental-shelf deposits laid down in a westward thickening zone. The depositional processes are described within this environment. A quartzite and siltstone province to the east, and a siltstone, carbonate, and quartzite province to the west.

Outcrops of Precambrian rocks are widespread in the southern part of Nye County. These rocks typically consist of quartzite, siltstone, and calcareous shale or chert (Chappell, 1972). Paleozoic rocks ranging in age from Early Cambrian to Pennsylvanian, have a similar distribution to the Precambrian rocks. The Paleozoic sections are dominated by calcareous rocks that include predominantly limestone and dolomite, with lesser amounts of siltstone, shale and argillite. These sections are exposed at Bare Mountain (east of Yucca Mountain) and a wider distribution to the south of Yucca Mountain, in a region surrounding Spring Mountain. North of Spring Mountain, in the Clark Range (eastwest of Yucca Flat), there are widespread exposures of Middle to Upper Paleozoic rocks composed of argillite, dark calc. conglomerate, quartzite, shale and limestone (Chappell, 1972). These rocks are also deposited at Calico Hills and on the northern part of Bare Mountain.

## GEOLOGIC AND TECTONIC SETTING

Yucca Mountain and NTS lie within the southern portion of Nye County, Nevada, near the southwestern edge of Great Basin Province. A geologic map of the Yucca Mountain region is shown in Figure 2. This region is underlain by a variety of rocks distributed in age from Precambrian to Quaternary. According to Cornwall (1972) most of the rocks of Precambrian and Early Paleozoic age in this region were deposited in a shallow water miogeoclinal environment. This is in agreement with Stewart (1980) who states that the sediments in the Great Basin are continental-shelf deposits laid down in a westward thickening prism. Two depositional provinces are recognized within this environment. A quartzite and a siltstone province in the east, and a siltstone, carbonate, and quartzite province to the west.

Exposures of Precambrian rocks are widespread in the southern part of Nye County. These exposures typically compose of quartzite, siltstone, and micaceous shale or shist (Cornwall, 1972). Paleozoic rocks ranging in age from Early Cambrian to Pennsylvanian, have a similar distribution as the Precambrian rocks. The Paleozoic sections are dominated by sedimentary rocks that include predominantly limestone and dolomite, with lesser amount of sandstone, siltstone, shale and argillite. These sections are exposed at Bare Mountain (east of Yucca Mountain) and a wider distribution to the south of Yucca Mountain, in a region surrounding Spring Mountain. North of Spring Mountain, in the Eleana range (north-west of Yucca Flat), there are widespread exposures of Middle to Upper Paleozoic rocks composed of argillite, dark chert, conglomerate, quartzite, shale and limestone (Cornwall, 1972). These rocks are also exposed at Calico Hills and on the northern part of Bare Mountain.

Yucca Mountain and its two adjacent basins are composed of rocks and alluvium from Tertiary to Quaternary. In general, the basins in this region are characterized by Tertiary and Quaternary alluvial fans and playa lake deposits. They normally range in thickness from a layer greater than 600 m to a thin alluvial covering overlying rock-pediment surface (Cornwall, 1972).

Yucca Mountain is composed largely of Miocene and Pliocene rhyolitic ash-flow and ash-fall tuffs. From borehole logging (Spengler and Rosenbaum, 1980) that penetrated to depths of 150 m, geologic units consisting of nonwelded to densely welded rhyolitic ash-flow tuffs are found to be separated by thin beds of air-fall and reworked tuff. Pre-Tertiary rocks surrounding the Yucca mountain region, are buried beneath the thick Tertiary and Quaternary deposits (Snyder and Carr, 1982; Carr, 1984). Snyder and Carr (1982) suggested that intrusive bodies which fed the Tertiary intrusions, lie beneath this region. In Jackass Flats and Crater Flats, the surface geology indicates composition of alluvium of Quaternary age, with gradation of gravels from streams and fans near the mountain to sand and silts at the valley bottom. Within Crater Flat, there are exposures of basalt flows and cinder cones which are very young, with ages ranging from Pleistocene to Holocene. There are also some exposures of basalt flows on the western side of Skull Mountain which overlies the Timber Mountain tuff (Cornwall, 1972).

Yucca Mountain and its vicinity lie within the Walker Lane, which is a shear zone that extends along the southwestern border of Nevada (Stewart, 1980; Carr, 1984). This zone represents a transition between the Great Basin Province and the Sierra Nevada. It has different structural trends than the predominantly north-south trends of the Great Basin and the northwest trend of the Sierra Nevada. The Walker Lane has a diverse topography which, according to Stewart (1980), is probably related to large scale right-lateral

displacement. The time of initiation in this zone is difficult to estimate. However, Stewart (1984) has reported that the Walker Lane deformation probably began as early as late Early Jurassic. Stewart further suggested that most of the right-lateral deformation occurred approximately 11-15 m.y. ago. This conclusion is based on the evidence that 11 m.y. old volcanic rocks near the Las Vegas Valley Shear zone are relatively undeformed. This suggestion follows the conclusion of Carr (1984) that the deformation in Walker Lane ceased approximately 10-14 m.y. ago. Evidence of strong structural deformation are found in the rocks that are exposed at Bare Mountain. These rocks (Precambrian to late Paleozoic sedimentary rocks) have been deformed by folding in late Paleozoic and Mesozoic, followed by intense thrusting and right-lateral faulting in Mesozoic time and finally, by normal faulting during the late Tertiary to Holocene (Cornwall, 1972). This deformation at Bare Mountain is probably related to the right lateral displacement of the Walker Lane.

Other structural deformation in this region can be attributed to Basin and Range high-angle type faulting, gravity sliding, caldera subsidence, high-angle faulting caused by volcanic activity, and strike-slip faulting. Basin and Range normal faults on the east and west flanks of Bare Mountain have a relative downward movement into the valleys. These faults are considered post Paleozoic since the Paleozoic rocks on the east side of Bare Mountain are cut off abruptly in a linear fashion and also because of observations of undisturbed small alluvial fans overlying the scarp (Cornwall, 1972). North-trending normal faults in the Yucca Mountain are typically downdropped to the west into Crater Flat. Most of these fault movements have reactivated preexisting faults. From the combination of normal fault movements (downdropped to the east at Bare Mountain, and to the west on Yucca Mountain), one can postulate a graben-type collapse in the Crater Flat. Volcanic related faulting within Yucca Mountain has the last displacement occurring approximately 10 m.y.

ago, which coincides with the decrease in silicic volcanism in the late Miocene (Carr, 1984).

Volcanic activity surrounding the Yucca Mountain area has greatly influenced the Tertiary structure of this region. The earliest widespread volcanism within this region (radius 100 km of Yucca Mountain) erupted about 17-18 m.y. ago, though eruptions might have started  $\approx$ 26 m.y. ago (Carr, 1984). Major silicic eruptions occurred approximately 16 m.y. ago, north of Yucca Mountain. The rate of silicic volcanism reached its peak  $\approx$ 13-14 m.y. ago, with the last dated eruption occurring about 5 m.y. ago. Basaltic eruptions became predominant after the eruption of Timber Mountain-Oasis Valley caldera, about 10.5 m.y. ago.

According to Carr (1984), there are possibly three major caldera complexes within Yucca Mountain (Fig. 2-B). These complexes include the Crater Flat-Prospector Pass caldera, the Timber Mountain-Oasis Valley caldera complex and possibly a pre-Crater Flat Tuff caldera complex. The oldest of these is probably the pre-Crater Flat caldera as suggested by Carr (1984). The exact location of the caldera and its dimension is not well known, though it was proposed by Carr (1984) as located just west of Yucca Mountain; where it would be buried by a thick layer of Crater Flat Tuff members. He arrived at that conclusion by analyzing the relative thickness of the tuffs beneath Yucca Mountain and Crater Flat. And he also suggested an occurrence of a pre-Crater Flat Tuff volcano-tectonic subsidence that took place beneath Yucca Mountain that extended to the Paintbrush Canyon Fault system. His conclusion is supported by the similarity of the Paintbrush Canyon Fault system with the ring-fracture system of the Crater Flat-Prospector Pass caldera complexes (Fig. 3).

The Timber Mountain-Oasis Valley caldera complex lies north of Yucca Mountain. Eruptions of this caldera complex coincide with the peak in silicic volcanisms (13-14 m.y. ago). The Timber Mountain Tuff and tuffs from the silicic Crater-Flat eruptions make up the majority of the composition of Yucca Mountain. Activity in the Timber Mountain-Oasis Valley caldera ceased about 10.5 m.y. ago (Carr, 1984). The last known basaltic eruption occurred approximately 0.25-0.30 m.y. ago in the vicinity of Lathrop Wells, 15 km south of Yucca Mountain.

To summarize the recent volcanic activity in this region, eruptions began approximately 26 m.y. ago, with the rate of silicic eruptions reaching its peak about 13 m.y. ago. The latest silicic eruption occurred  $\approx$ 5 m.y. ago. Basaltic volcanism began about 12 m.y. ago during the Timber Mountain-Oasis Valley eruptions and the rate of eruptions has been fairly constant, with the last known basalt eruption occurring near Lathrop Wells.

### PREVIOUS GEOPHYSICAL WORKS

Extensive geophysical work has been published on Yucca Mountain and the Nevada Test Site. These works include seismic refraction and reflection surveys, gravity and aeromagnetic studies, well-logging analysis, seismicity studies, and three-dimensional modeling of the crust and mantle using teleseismic P-wave delay residuals.

Seismic reflection survey has been proven ineffective in this geologically complex region. Work done by McGovern (1983), to determine the shallow structure was hampered by the high noise environment. These noises originated from the highly absorptive and ringing nature of the highly fractured welded to non-welded volcanic tuff. No conclusion concerning the shallow structure except of the high noise environment of the vicinity, can be derived by interpreting reflection phases. Refraction surveys to determine the shallow

structure produced better results, though there were difficulties involved in obtaining good first arrivals in the data (Pankratz, 1982). Figure 4 shows a summary of the locations of the shallow refraction surveys conducted in the Yucca Wash area (northwestern corner of Jackass Flats and Yucca Mountain) and Calico Hills. The velocity structures indicated strong horizontal variations, that could result from faults that are parallel and perpendicular to the axis of the wash. These velocity models have been interpreted as a four-layer model. P-wave velocities in the first two layers range from 1-2.8  $\text{kms}^{-1}$ ; and the latter two layers have velocities of 2.1-4.8  $\text{kms}^{-1}$ . When these layer velocities were compared with geophysical drill-hole data, (UE 25-1, Fig. 4) (Pankratz, 1982), the greatest contrast in velocities occurred in layer 2. Basement velocities obtained from the profile at Calico Hills range from 4.5-5.3  $\text{kms}^{-1}$ .

Aeromagnetic studies revealed that most of the magnetic anomalies in this region are caused by volcanic units (Kane and Bracken, 1983). Occurrence of low magnetic anomalies in the southern part of Crater Flat coincides with the outcrops of Quaternary basalts of the Black Cone. Magnetic anomalies surrounding Yucca Mountain have a north-northeast trend that correlate to the vertical structural offset in the tuff unit underlying this region. Figure 5 illustrates a generalized magnetic contour map of the region.

Gravity lows have been observed in Crater Flat and parts of Yucca Mountain (Fig. 6). Interpretation done by Snyder and Carr, (1982) showed that low gravity anomalies in Crater Flat are caused by a thick layer of tuff, having a lower average density than the surrounding Paleozoic rocks. This thick layer of volcanic rocks extends to 2.5 km below sea-level, beneath Crater Flat and into parts of Yucca Mountain. The Paleozoic surface within this region, has a northeast to southwest trend as interpreted from regional gravity. This surface outcrops at Eleana Range, Calico Hills, and Bare Mountain.

From deep refraction data, the crustal thickness in the southern part of the Basin and Range Province is about 31-32 km, as compared to the average crustal thickness in the Basin and Range Province being 32-34 km (Prodehl, 1979).  $P_n$ -velocities determined from these surveys range from 7.5-7.8  $\text{kms}^{-1}$ . A summary of crustal thickness and average  $P_n$  velocities (Prodehl, 1979) is shown in Figure 7.

Results obtained from three-dimensional modeling of teleseismic P-wave residuals shows evidence of low velocity in the upper crustal structure near Pahute Mesa and Timber Mountain caldera (Monfort and Evans, 1982). The uppermost mantle in this region has velocities increasing towards the west. There is also an indication of a zone of high velocity in the center of NTS with velocities of 3%-4% faster than the average velocity. At greater depths ( $> 150$  km) the mantle is considered homogeneous based on only small changes in the velocities (average perturbation of  $\pm 1\%$ ) (Monfort and Evans, 1982).

Seismicity surrounding the Yucca Mountain area during the period of 1981 (Rogers *et. al.*, 1983) is shown in Figure 8. Most of the earthquakes were located in the western part of Skull Mountain. These earthquakes have hypocentral depths of less than 5 km, with average magnitudes of 2.0  $M_L$ . Reports on the seismicity done by Carr (1984) shows a relatively low seismic activity in the western part of NTS. From Figure 8 (seismicity during the period of 1981), and seismic activity summarized by Carr (1984), the Yucca Mountain area is considered aseismic, although records of seismicity prior to underground nuclear testing, have been restricted to earthquakes with magnitude greater than 4.0  $M_L$ .

## FIELD EXPERIMENTS

Among the studies which have been conducted in this region is a refraction experiment by the USGS during the period from 1980-1982. Five refraction lines were deployed



in the experiment to record seismic energy from four shot points. The location of these refraction lines are shown in Figure 9. These lines are all unreversed.

Three of the shot points were nuclear explosions, two located on Pahute Mesa and one in Yucca Flat. The fourth shot was a chemical blast near Beatty, Nevada. The average length of the profiles was 70-80 km. The first profile (Line 1), consisted of 19 recordings of a nuclear explosion at Pahute Mesa. This profile extended north-south from a distance of 42 km at Yucca Mountain to a distance of 62 km north of Lathrop Wells, Nevada. The second profile (Line 2), consisted of 20 recordings of a nuclear explosion at Yucca Flat, in the distance range of 38-60 km. The third profile consisted of recordings of a nuclear explosion along two profiles extended approximately north-south on the east and west side of Yucca Mountain. The east profile (Line 3 East), was the longest profile (33 stations) extending 110 km with the closest station at 42 km. It transversed over the Amargosa Desert to the Death Valley junction, California. The west profile (Line 3 West) had 26 stations, extending from 52 km to 87 km. This profile crossed Crater Flats and the southern tip of Bare Mountain to the California-Nevada border. The fourth profile (Line 4), consisted of 85 recordings of a chemical blast near Beatty, Nevada. This profile extended along an east-west line over a distance of 65 km. The profile crossed Bare Mountain, Crater Flats, Yucca Mountain, and Jackass Flats to the northern side of Skull Mountain. The average station spacing for the profiles described above is approximately 1.2 km per station. The most dense station spacing is in Line 4 (0.9 km/station) and the least dense is in Line 3 East (2.1 km/station).

All the seismograms were recorded on vertical component velocity transducers. These seismograms were later digitized at 200 samples per second. All the recorders were identical but were set at different gain settings depending on the distance to the source. The

natural period of all the geophones is 0.5 seconds with a motor constant of one volt per  $\text{cms}^{-1}$ . The instruments can be programmed to switch on automatically at a pre-designated time with a programmable recording window. Calibrations of the instruments were done automatically prior to the energy arrival time, and were recorded on cassette tapes. Figure 10 shows an example of the system response curve for the recording instruments. Technical details concerning the instrumentation and field operations can be obtained from Hoffman and Mooney, (1984).

Figure 11(A-E) shows the record section of each line. These record sections are trace normalized to the maximum amplitude, and reduced to  $6 \text{ kms}^{-1}$  to facilitate the correlation of similar phases in each record section.

In Figure 11-A, the traces recorded from shot point 1 have their first arrivals clipped up to distances of 55 km. Emergent arrivals in Line 2 were observed at distances between 49 km to 55 km (Fig 11-B). No obvious reflective phase was observed in the record section. However, on the record section from Line 3 West (Fig. 11-D) secondary arrivals were observed at 4-5 seconds reduced times at distance ranges of 70 km to 87 km. The same reflective phase was also observed at 85 to 110 km on Line 3 East (Fig. 11-C). These records all have good signal-to-noise ratio and were not clipped.

In all the lines except Line 4, there were no close recordings to determine the near surface velocities. Traces from Line 4 (Fig. 11-E), show travel time delays of 0.4 seconds to 0.5 seconds over Crater Flats, and Yucca Mountain. A reflective phase at distances of 50-65 km is observed in this record section. First arrivals at distance ranges of 20-35 km were highly emergent compared to the first arrivals of stations less than 10 km and arrivals at 40-50 km distance.

## DATA ANALYSIS AND INTERPRETATION

The general procedure in analyzing the Yucca Mountain refraction data is to use a linear inverse procedure to produce an average extremal velocity model for the region, using the combined data set consisting of the five refraction profiles. The average velocity model will provide a guide in determining the specific velocity model for each profile by analysis of travel time data, using trial-and-error two-dimensional ray-tracing; and by comparing the synthetic with the observed seismograms. All models for shallow structures are compared with two-dimensional gravity calculations.

The effects of lateral heterogeneities in the near surface structures are removed from the data sets before they are combined (refer to Appendix B). This is accomplished in an iterative manner by modeling the high frequency Bouguer gravity data, and by tracing rays through a two dimensional model of the near surface structure to match the scatter in the observed travel time.

The algorithm for the two-dimensional ray-tracing was developed by McMechan and Mooney (1980), using the zero-order asymptotic ray theory. Using this theory, head waves cannot be generated, but they can be approximated by inserting a thin layer between the boundaries having small positive velocity gradients. The program used to do the ray-tracing supports two-dimensional velocity models.

Theoretical gravity values are computed at evenly-spaced points using Talwani's (1959) polygon method. High frequency gravity data is obtained by estimating the regional (low frequency) effect of the gravity field by least-squares fit and removing this value from the observed data. Snyder and Carr (1982), reported a northeast-southwest trend of the

gravity high in the vicinity of Yucca Mountain. Since most of the gravity profiles roughly follow this direction, they are all corrected for the regional effect (except for the east-west profile).

The correction for the regional effect is made by subtracting from the observed gravity the value of the regional gravity for the same latitude and longitude. The regional gravity is assumed to be constant for all points in the area. The regional gravity is determined from the mean gravity for all points in the area. The regional gravity is determined from the mean gravity for all points in the area. The regional gravity is determined from the mean gravity for all points in the area. The regional gravity is determined from the mean gravity for all points in the area.

The gravity profiles are plotted on a grid of latitude and longitude. The profiles are plotted on a grid of latitude and longitude. The profiles are plotted on a grid of latitude and longitude. The profiles are plotted on a grid of latitude and longitude. The profiles are plotted on a grid of latitude and longitude.



Figure 1. Gravity profile of line A across a portion of the area shown in Figure 1.

The gravity profile of line A shows a general increase in gravity from west to east, with a local maximum near the center of the profile. The gravity values are approximately 0.25 mgals at the west end and 0.35 mgals at the east end.

## DATA REDUCTION

Arrival times for the first and later arrivals, with their associated errors, are determined using an iterative computer routine. The uncertainties in the arrival times are estimated by bracketing the earliest and the latest time for the specific energy arrival. The arrival time is defined as the arithmetic average of the two extreme times. The average picking errors for Lines 1, 2, 3 East, 3 West, and 4 are 0.05 seconds, 0.08 seconds, 0.07 seconds, 0.08 seconds, and 0.05 seconds respectively. Generally, the picking errors increased from  $\pm 0.02$  seconds at close stations to  $\pm 0.19$  seconds at larger distances, since arrivals are emergent at further distances. The travel time data set used in this analysis consists of the arrival times with their estimated errors versus the shot-point receiver distance with a distance error of 1.5 meters (Hoffman and Mooney, 1984).

The starting model for the shallow velocity structures is based on a simplified version of Hoffman and Mooney's interpretation of Line 4 (1984). This model is chosen as a starting model since it crosses all the other refraction lines. This will provide constraints on the near surface structures. Density models for different profiles are expressed as G1, G2, G3W, G3E, G4, and velocity models R1, R2, R3W, R3E, and R4 correspond to Line 1, Line 2, Line 3 West, Line 3 East and Line 4 respectively.

### LINE 4

Gravity modeling and two-dimensional ray-tracing of refracted and super-critical rays are used to derive the shallow structures along Line 4.

The gravity profile of Line 4 shows a gravity high near Bare Mountain, a gravity low

at Crater Flat, and a gravity high at Skull Mountain (G4, Fig. 12-E). The gravity highs are related to the outcrops of Paleozoic sedimentary rocks (Healey et al., 1980) and the gravity low is associated with the Crater Flat caldera complex (Carr, 1984). The depth of the caldera is approximately 2 km to 3 km. Materials with density of  $2.25 \text{ gcm}^{-3}$  are used to model the caldera fills. The densities used in this model and other subsequent models are based on density relationships from Snyder and Carr (1982), with known geologic units in this region.

The velocity model R4 (Fig. 12-E) is composed of 4 layers with lateral velocity gradients. The top layer has average velocities ranging from  $2.0 \text{ kms}^{-1}$  to  $3.65 \text{ kms}^{-1}$ . The second has average velocities of  $4.05 \text{ kms}^{-1}$  to  $5.75 \text{ kms}^{-1}$ , and in the third layer average velocities range from  $5.75 \text{ kms}^{-1}$  to  $6.23 \text{ kms}^{-1}$ . The fourth layer has velocities ranging from  $6.23 \text{ kms}^{-1}$  to  $6.35 \text{ kms}^{-1}$ . The velocity model R4 shows a highly variable structure beneath Crater Flat, Yucca Mountain, and Bare Mountain. Depth to layer 2 is shallowest at Bare Mountain and deepest at Yucca Mountain. The depression beneath Crater Flat correlates with the large observed travel time delays. Ray paths and travel times across Jackass Flats (distance of 35-50 km) are relatively uniform. The resulting velocity-density relationship for Line 4 is tabulated in Table 5.

Analysis of the shallow structures in the other profiles are constrained to the number of layers in R4 and G4. Deviations from the number of layers used in this analysis are attributed to the lateral heterogeneities within each layer.

#### LINE 1

The station in Line 1 closest to the source is 43 km and thus R1 (Fig. 12-A) is not constrained at smaller distance ranges. Model R1 shows an increase in thickness in the

second layer from 38 km to 45 km distance. This distance range corresponds to the change in the geology and structure, from Yucca Mountain to Jackass Flats. Lateral velocities in layer 1 along the length of the profile range from  $1.8 \text{ kms}^{-1}$  to  $2.4 \text{ kms}^{-1}$ , in layer 2 from  $4.0 \text{ kms}^{-1}$  to  $5.7 \text{ kms}^{-1}$ , and in layer 3 from  $5.3 \text{ kms}^{-1}$  to  $6.35 \text{ kms}^{-1}$ .

R1 is used to constrain the number of layers in the gravity model, G1. The densities of each layer in the gravity model are restricted to  $1.8\text{-}1.9 \text{ gcm}^{-3}$  in layer 1,  $2.2\text{-}2.5 \text{ gcm}^{-3}$  in layer 2, and densities greater or equal to  $2.6 \text{ gcm}^{-3}$  in layer 3. There are certain areas where G1 deviates from R1. These deviations result from local variations which are not considered by the two-dimensional ray-tracing modeling. At distances of 40-50 km, a strong local variation exists in the gravity data, which can be explained by a layer with a lower density contrast at 0.6 km below the surface, and a layer at depth 3 km to 4 km below sea-level with density of  $2.5 \text{ gcm}^{-3}$ . The resulting relationships between the velocity and density are tabulated in Table 1.

## LINE 2

The gravity and travel time fits for Line 2 are shown in Figure 12-B. In general, the results of the theoretical calculations of the travel time and gravity for Line 2 agree with the corresponding observed data. Ray-tracing along Line 2 indicates a decrease in the thickness of the alluvium at 40 km to 50 km distance. This decrease is also observed in the gravity model G2 although the amounts of thinning of the alluvium in R2 and G2 are not equal. Thinning of layer 1 is attributed to the effects of the higher density and velocity of Little Skull Mountain since the refraction line is deployed near the western corner of Little Skull Mountain.

Analysis of the gravity model G2, shows another decrease in alluvium thickness at 8-20 km distance, corresponding to the location of Mine Mountain 17 km along the profile where there are exposures of Paleozoic sedimentary rocks (Healey et al., 1980).

Alluvium in Yucca Flat has a density which is  $0.1 \text{ gcm}^{-3}$  ( $1.8 \text{ gcm}^{-3}$ ) lower than that at Jackass Flats ( $1.9 \text{ gcm}^{-3}$ ). This difference in density can be removed by increasing the thickness of the alluvium in Yucca Flat. However, preference over the  $0.1 \text{ gcm}^{-3}$  density difference is desirable in order to obtain similar layer thicknesses in G2 and R2. Table 2 contains the resulting velocity-density relationship of R2 and G2.

#### LINE 3 WEST

The residual gravity of Line 3 West indicates the presence of strong local anomalies, evident at 75 km to 80 km distance with approximately 20 mgals change in gravity (Fig. 12-C). The travel time fit with the observed data has less scatter than the gravity fit as shown in Figure 2-C.

Model R3W indicates a basin-like structure with the thickening of layer 1 having a maximum at approximately 45 km distance. G3W indicates an additional layer of density of  $2.0 \text{ gcm}^{-3}$  between layer 1 and layer 2, and it seems to thicken at 30 km distance along the profile. The highest elevation along the profile corresponds to the general area of North Timber Peak which is situated in the Timber Mountain area. This additional layer ( $2.0 \text{ gcm}^{-3}$ ) is probably related to the volcanic debris resulting from the Timber Mountain Tuff eruptions and the collapse of the caldera (Carr, 1984). At distances of 75 km to 90 km, in G3W, there are strong heterogeneities in layer 1, which correspond to thinning of the same layer in R3W. These distances coincide with Precambrian outcrops (Cornwall, 1967) near the California-Nevada border. For the resulting velocity-density relationship in Line 3



West, refer to Table 3.

### LINE 3 EAST

Figure 12-D illustrates the models and the fits by gravity and ray-tracing modeling of Line 3 East. The travel time fit is generally good up to distances of 87 km beyond which observed times scatter strongly. The theoretical fit to the observed gravity is not as good as in Line 1 or Line 2.

Layer 2 in R3E thickens abruptly at distances of 35 km to 50 km and then gradually thins. G3E shows a similar geometry, but a layer of higher density of  $2.4 \text{ gcm}^{-3}$  is needed to accommodate the observed data (Fig. 11-E). This extra layer thins out as the thickness of layer 2 decreases. G3E also indicates that at the end of the profile, the depth of layer 1 increases to approximately 3 km.

A positive anomaly in G3E at 55 km to 80 km distance is not evident in R3E. A possible explanation for the discrepancy is that the station spacing along this portion of the line is the least for the whole line. Table 4 shows the resulting velocity-density relationship of Line 3 East.

### TRAVEL-TIME ADJUSTMENTS FOR THE SHALLOW STRUCTURES

The layer velocities in each model are assumed to have low or zero vertical velocity gradients. This leads to an estimation of a laterally heterogeneous layer with vertical homogeneities. This estimation will aid in the  $\tau(p)$  analysis which assumes the structures consist of flat lying layers. Thus, all times will be adjusted vertically to eliminate (to first order) variations assumed to be caused by lateral heterogeneities. Discussion of the delay-

time or the tau-p method is described in the next section.

The depth to the datum is defined to be a layer of average density of  $2.6 \text{ gcm}^{-3}$ , with average velocity ranging from  $5.5 \text{ kms}^{-1}$  to  $6.3 \text{ kms}^{-1}$ . This range of velocities and densities corresponds to the values in layer 3 of the velocity models. The travel time data are corrected for the lateral variations of layer 1 and 2, by replacing these two layers with materials from layer 3. The data set is then corrected to an average elevation of 1 km above sea-level, the average elevation of all the stations. The computation for correcting the lateral heterogeneities is accomplished by determining the travel times of each receiver and the source from the surface elevation to the datum plane  $t_d$  ( $t_d$  = travel times reduced to datum plane), and subtracting this value from the observed travel times ( $t_o$ ). The travel time of each receiver and the source from the datum to the average elevation with layer 3 velocities  $t_u$  ( $t_u$  = time from datum plane to average elevation), is then added to the observed travel times. The resulting corrected times  $t_c$ , is thus:

$$t_c = t_o - (t_d + t_u)$$

The depth to the datum ranges from 2 km to 3.5 km.

After each profile is corrected for the near surface heterogeneities, the travel time data are assumed to represent the data sets for earth models with homogeneous horizontal layers.

## INTERPRETATION FROM TRAVEL TIME INVERSION OF $\tau(p)$

The corrected travel times from all 5 profiles are combined resulting in a more complete data set. A comparison between the corrected and the uncorrected travel times shows a significant decrease in scattering at distances between 40 km to 60 km (Figure 13).

### DELAY-TIME METHOD

The  $\tau(p)$  inversion method was first developed by Bessonova *et. al.* (1974), and later modified by Kennett (1976), Kennett *et. al.* (1976), and Garmany *et. al.* (1979). The travel time data are reparameterized in terms of the  $\tau(p)$  where  $\tau$  is the delay time, and  $p$  is the ray parameter. One of the advantages of reparameterizing the data into  $\tau(p)$  is that the delay time function ( $\tau(p)$ ) is linearly related to the earth structure. This linearity can be exploited by using linear programming to find the extremal velocity depth bounds. Another feature that is inherent in  $\tau(p)$  is that it is a single-valued monotonically decreasing function, unlike the general travel time curve, which has multiple values in the presence of travel time triplications. In the presence of low velocity zones, the  $\tau(p)$  suffers a negative discontinuity. Kennett *et. al.* (1976) have suggested that such a discontinuity could be used as an indication of the presence of low velocity layer. The inversion of  $\tau(p)$  produces extremal velocity bounds which contain all the realizable velocity models that are consistent with the observed data. However, not all velocity models within the bounds are realizable velocity models.

### COMBINED DATA

Reparameterization of the travel-time combined data produces a wide but smoothly varying  $\tau(p)$  envelope which indicates a smooth varying average velocity structure.  $T(p)$ ,  $X(p)$ , and cross-over constraints are used in the inversion of the combined data. The  $T(p)$  and  $X(p)$  constraints are coarsely applied, since the  $T(p)$  and  $X(p)$  are sensitive to first order errors in  $p$  (Orcutt *et. al.*, 1980) (Figs. 14B, and 14C). The  $T(p)$  and  $X(p)$  data constrain arrivals with a constant slowness  $p$  to arrive within certain range of time and distance. The cross over constraint imposes the condition that two consecutive travel time branches cross each other within a certain distance. The resulting extremal bounds for the average velocity structure are well constrained for the upper structures, but they swell considerably for deeper structures (Fig. 14-A). The upper limit of the extremal bounds shows characteristics of velocity steps as opposed to the lower limit, which indicates a gradual change in velocity with depth.

Next, a one dimensional velocity model is derived iteratively using one-dimensional ray tracing. This one-dimensional model represents the average deeper velocity for the region. The model contains four segments of velocity gradients. The first segment has a velocity gradient of  $0.133 \text{ sec}^{-1}$ . The next segment of the velocity model contains a relatively high velocity gradient of  $0.242 \text{ sec}^{-1}$  which extends from 2.3-5.6 km depth. The deeper structures ( $> 5.6$  km depth) have a lower velocity gradients than the upper structures. The velocity model extends to approximately 20 km depth with an average velocity gradient of  $0.006 \text{ sec}^{-1}$ .

The data from the five profiles are then interpreted separately to compare any deviations from the average model.

The extremal bounds for Line 1 are poorly constrained for the deeper structures. The depth of the lower bound extends to approximately 13 km, whereas the upper bound only

extends to approximately 2.5 km (Fig. 15-A). The specific velocity model for Line 1 has a relatively high velocity gradient in the upper 1.5 km ranging from 5  $\text{kms}^{-1}$  below the surface to 6  $\text{kms}^{-1}$  at depths of 1.5 km. This specific velocity model is obtained by tracing rays through a one-dimensional structure. Only observed first arrivals are used, since the traces in Line 1 are clipped.

In a comparison to the average velocity model, the velocity gradients in the upper structures are higher and extend to a shallower depth than the average model. At depths of approximately 5 to 10 km, the specific velocity model of Line 1 has a velocity gradient of 0.03  $\text{sec}^{-1}$  which is lower than the velocity gradient (0.045  $\text{sec}^{-1}$ ) of the average model.

Line 2 has travel time data that cover a wider range than Line 1. Furthermore, the amplitudes in Line 2 are not clipped. However, due to lack of close travel time data, the extremal bounds are not well constrained. The  $\tau(p)$  of Line 2 are inverted using  $T(p)$  and  $X(p)$  constrains (Fig. 15-B). The depth of the lower bound extends to approximately 15 km with the depth of the upper bound extending to 5 km. The resulting extremal bounds are wide at greater depths.

The specific velocity model for Line 2 is obtained by iteratively matching the observed reflection times. The additional information on the reflection times has helped in defining the shallower structures not constrained by the first arrivals. A velocity step occurs at depths of 0.45 to 0.6 km with velocity of 5.34  $\text{kms}^{-1}$ . This velocity step is obtained by modeling the reflection times in Line 2. This reflective phase is observed at distances of 40 to 50 km at approximately 1 second reduced time (reduced at 6  $\text{kms}^{-1}$ ) (Fig. 11-B). The velocity model for Line 2 has a series of velocity gradients of 0.225  $\text{sec}^{-1}$ , 0.044  $\text{sec}^{-1}$  and 0.020  $\text{sec}^{-1}$  in increasing depth. The highest velocity gradient of 0.225  $\text{sec}^{-1}$  corresponds to depths of 1.2 to 3 km with velocity of 5.9  $\text{kms}^{-1}$  to 6.35  $\text{kms}^{-1}$  respectively. At these

depths, the velocity gradient corresponds to the highest velocity gradient of  $0.242 \text{ sec}^{-1}$  in the average model. At depths of 7 to 12 km, the velocity model of Line 2 has the least average velocity gradient of  $0.020 \text{ sec}^{-1}$ .

Comparing the velocity gradient at this depth range to that of the average model, the velocity gradient is found to be 55% lower than the average velocity model. No comparison can be made for lower velocity structures since the profile distance is insufficiently long to sample the deeper velocities.

The extremal bounds in Line 3 West have been constrained with T(p) and X(p) constraints (Fig. 15-C). The bounds show a high velocity gradient in the upper 3 to 5 km. However for deeper velocity structures the bounds are poorly constrained.

The specific velocity model for Line 3 West is obtained by incorporating secondary arrivals to constrain the deeper structures. The velocity model has a high velocity gradient of  $0.525 \text{ sec}^{-1}$  for the upper structure which is in good agreement with the extremal bounds. At a depth of 2 km, the velocity gradient decreases to  $0.019 \text{ sec}^{-1}$ . The velocity at this depth changes from  $6.45 \text{ kms}^{-1}$  at 2 km to  $6.6 \text{ kms}^{-1}$  at 10 km deep. Reflective phases are used to model a velocity boundary at 23 km depth and also to model the depth to the Moho; which is approximately 39 km (Fig. 15C).

A comparison of the velocity model of Line 3 West with the average velocity model shows deviations both in the upper 5 km and deeper structures. However, both models show high velocity gradients for the upper structures. The velocity model of Line 3 West has a higher velocity in its shallow structures (Fig. 15-C) than the average model (Fig. 14-A). However, this is the reverse for the deeper structures, where the average model has a significantly higher velocity than the model from Line 3 West.

The extremal bounds of Line 3 East are the least constrained among the data set (Fig. 15-D). The upper bound is unconstrained even with the addition of  $T(p)$  and  $X(p)$  data. The travel time data coverage in this line is approximately 62 km, but the data all lie approximately on the same travel time branch. This reduces the number of  $\tau(p)$  points for inversion. The average bounds are used to provide additional constraints for the upper velocity bounds. With this addition, well constrained bounds of realizable velocities are produced. The bounds show a constriction at a velocity of approximately  $6 \text{ km s}^{-1}$  with depth ranging from 1.7 km to 3.8 km. However, at deep structures, the extremal velocity bounds swell considerably.

The specific velocity model for Line 3 East is derived by modeling the first and later arrivals. The later arrivals are recognized as Moho reflections  $P_m P$ , where the Moho is defined from the model to be 35 km depth. The velocity model has a high velocity gradient for the upper structure ( $0.45 \text{ sec}^{-1}$ ) followed by a lesser velocity gradient at depths below 2 km.

The velocity structure of the upper 5 km crust in Line 3 East has higher velocities values than the average model. Below this depth, the velocity gradients of both the average model and Line 3 East model are similar.

The extremal bounds of Line 4 are better constrained than the bounds of other lines. These bounds have been constrained using  $T(p)$ ,  $X(p)$  and cross-over constraint (Fig. 15-E). The cross-over constraint is added resulting a narrower bound for the upper 5 km. A velocity discontinuity is observed in the extremal bounds as a result of the cross-over constraint. The bounds get wider at deeper structures even though the travel time coverage of Line 4 is the most extensive.

The specific velocity model of Line 4 does not, however show the velocity discontinuity as observed in the extremal bounds. The velocity model consists of velocity gradients, with the highest velocity gradient of  $0.325 \text{ sec}^{-1}$  occurring at depths of 2 km (velocity of  $5.75 \text{ kms}^{-1}$ ) to depths of 4 km (velocity of  $6.4 \text{ kms}^{-1}$ ). A reflective phase is used to define a boundary at 15 km depth, where a small change in the velocity gradient occurs from  $0.05 \text{ sec}^{-1}$  to  $0.04 \text{ sec}^{-1}$ . By using the additional information from reflection travel times, the specific velocity model of Line 4 extends deeper than is defined by the extremal bounds. Figure 4-E indicates the depth of 15 km which is constrained by the extremal bounds.

The upper 4 km of the velocity model of Line 4 correlate well with the average velocity model. At intermediate depth, which extends from 4.5 km to 14.5 km, the average velocity model has a higher velocity than the velocity model of Line 4. For depths greater than 15 km no definitive comparison can be made, since the deeper velocity structures of Line 4 are not well constrained even by reflective travel times.



## ANALYSIS AND INTERPRETATION OF SYNTHETIC ARRIVALS

Calculations of synthetic seismogram sections are done using the approach of McMechan and Mooney (1980). This method uses the same algorithm from the two-dimensional ray tracing described previously. Synthetic arrivals are calculated using the modification of the asymptotic ray theory which is based on assumptions that the wave field can be decoupled into an infinite number of elementary waves (May and Hron, 1978). These elementary waves correspond to the individual rays which are computed along all possible ray-paths between the source and receiver.

The zero-order asymptotic ray theory is an approximation of the asymptotic ray theory. The construction of the synthetic arrivals is based on:

- (i) the information of the travel time of the ray,
- (ii) calculations of its complex amplitude, and
- (iii) the source function. (Cerveny, 1979)

The final velocity models are obtained by considering both the observed travel times and the amplitude behaviors.

The final velocity models are created by the combination of the shallow and deeper structures of each line. Two-dimensional ray tracing is employed to match the arrival times of both the principal and secondary arrivals. Comparisons of the observed and synthetic amplitudes are done in two ways: (1) the synthetic amplitudes are compared with the observed amplitudes within the trace, and (2) the relative change in the amplitude along the record section is compared with the relative change in the synthetic section. This process is done iteratively to fit the observed travel times and the observed amplitudes. Figure 16(A-

E) illustrates the ray diagram and the comparison between the observed and synthetic record sections. The observed record sections are plotted with amplitudes scaled to  $1/\text{distance}$  to correct for the geometrical spreading. The final models that are used to obtain the fits are shown in Figure 17(A-E).

## FINAL VELOCITY MODELS

### LINE 1

The final velocity model for Line 1 is shown in Figure 17-A. The bold lines indicate places where the rays turn. A mid-crustal boundary is defined at depths of 20 km. This boundary is defined using travel time from a reflected phase. The fit to the observed travel time (Fig. 16-A) seems to be in good agreement with the calculated times. The upper structures in Line 1 show good correlation between the calculated and the observed times (43 km to 53 km). At distances of 60 km and further however, the fit is not very good. The total thickness of the upper structure in Line 1 is about 5-6 km.

The amplitudes of the first arrivals in Line 1 are clipped up to distances of 53 km, but a reflective phase at distances between 55 km to 62 km corresponds to the calculated times for the boundary at 20 km depth (Fig. 17-A). A comparison of the synthetic seismograms for Line 1 does not provide additional information since the observed amplitudes are clipped. But the relative amplitudes for the reflective phase in the observed seismograms are higher than the first arrival amplitudes (Fig. 16-A).

### LINE 2

Figure 16-B illustrates the ray tracing diagram, record section and the synthetic sec-

tion of Line 2. Using reflective phases observed at 35 to 45 km and 50 to 60 km, two boundaries are observed at depths of 14 km and 24 km respectively (Fig. 17-B). The calculated travel times for rays that are reflected off these boundaries are on the average, in good agreement with the observed times. Rays refracted at depths of 2 to 5 km below the surface in layer 3, are used to match the first arrivals in the observed times. Travel time fits of the calculated first arrivals are in general in good agreement with the observed times except at distances between 45 to 48 km. Here, the calculated times are approximately 0.2 seconds later than the observed times.

The observed record section in Figure 16-B shows that first arrival amplitudes for traces between 45 to 52 km are relatively smaller than the amplitude of the same phase at other distances. Reflective phases are also shown in the figure with their associated picks. The synthetic section has a high amplitude at 'a' (53-56 km) and 'b' (38-41 km). These high amplitude phases correspond to first arrival amplitudes at 40 km and at 56 to 58 km on the observed sections. The relative amplitudes of 'b' are higher than the amplitudes of 'a'. This is in good agreement with the observed amplitudes. The synthetic reflective phases do not show high amplitudes as seen in the observed sections. The lower observed amplitudes at 45 to 52 km correspond to the relatively lower synthetic amplitudes.

The velocities in layer 1 range from  $2.3 \text{ kms}^{-1}$  at the surface to  $4.0 \text{ kms}^{-1}$  at the bottom of the layer (Fig. 17-B and Table 6-B). Layer 2 velocities range from  $4.0 \text{ kms}^{-1}$  in the Amargosa Desert to  $5.8 \text{ kms}^{-1}$  in the Jackass Flats. The velocity gradient decreases as depth increases from 2 to 3 km. A velocity contrast of 0.5 to  $0.1 \text{ kms}^{-1}$  is used to calculate the synthetic arrival for the reflective phase. The thickness of layer 4 is 10 km and it has a velocity gradient of  $0.02 \text{ sec}^{-1}$ . Layer 5 also has a thickness of 10 km, but has a lower velocity gradient of  $0.01 \text{ sec}^{-1}$ . The velocity below layer 5 is  $6.8 \text{ kms}^{-1}$ .

### LINE 3 WEST

An intra-crustal boundary is apparent at depths of 21 km in the final velocity model of Line 3 West. The depth of the Moho, as defined from reflection times, is 37 km (Fig. 17-C). The calculated reflective arrival are in good agreement with observed times with a maximum error of  $\pm 0.05$  sec between the observed and calculated times. The travel time fit of the calculated first arrivals also correlates well with the observed times throughout the record section.

A comparison of the reflective amplitudes from the 21 km deep boundary in the observed section is lower than the amplitudes of the reflective phase from the Moho. The same trend is also observed in the synthetic section with the reflective amplitudes from the Moho being considerably higher (Fig. 16-C). The high reflective amplitude from the Moho is modeled as wide-angled reflection which results from a build-up in reflective energy near the critical angle.

The final velocity model (Fig. 17-C and Table 6-C) has a typical higher velocity gradient in the upper 5-6 km, followed by a decrease in the velocity gradient in layer 4. The boundary at 21 km deep has a velocity contrast of  $0.1 \text{ kms}^{-1}$  where the velocity changes from  $6.2 \text{ kms}^{-1}$  above the interface to  $6.3 \text{ kms}^{-1}$  below the interface. A velocity contrast of  $1.1 \text{ kms}^{-1}$  is used to model the wide-angled reflections from the Moho. The thickness of the lower crust (layer 5) is approximately 15 km. Layer 4 has a thickness of 15 to 16 km.

### LINE 3 EAST

A reflective phase in Line 3 East at 4 to 5 seconds reduced time is interpreted as Moho reflections (Fig. 16-D). The depth of the Moho is 38 km as determined from the

two-dimensional ray tracing. Two other intra-crustal boundaries are observed at 28 km and 31 km (Fig. 17-D). In general, the observed travel time and the calculated reflective and first arrival times are in good agreement.

The amplitudes of the reflections from the Moho in the observed record section are higher than the first arrivals (Fig. 17-D) whereas, the intra-crustal reflections in the synthetic section have a relatively smaller amplitude than the corresponding observed amplitudes.

#### LINE 4

A ray diagram of Line 4 (Fig. 17-E) shows a mid-crustal boundary at depths of 13 km. First arrivals across Bare Mountain are very well correlated and at distance ranges greater than 55 km, there is some scatter in the travel time fit. Scattering in the observed data indicates that the arrivals are highly emergent.

The observed record section (Fig. 17-E) shows higher amplitudes at ranges of 47 to 60 km. At Yucca Mountain, very low energy is observed in the seismograms. The synthetic section (Fig. 17-E) shows high amplitude first arrivals at Bare Mountain and low amplitude first arrivals in the vicinity of Yucca Mountain. High energy arrivals from the reflective phase is modeled using wide-angle reflections. The velocity contrast needed to generate the wide-angle reflections is  $0.2 \text{ kms}^{-1}$ . The final model of Line 4 shows a layer of thick low velocity materials at 20 to 30 km distance (Fig. 17-E).

## DISCUSSION

The surface geology in the vicinity of Yucca Mountain is typically characterized by Paleozoic and Cenozoic sedimentary rocks and alluvium (Healey *et. al.*, 1980). Studies in the Yucca Mountain area have shown that a northerly trend of basin and range type faults is characterized by high angle normal faults (Carr, 1984). However, the shallow velocity models obtained in this study do not have the resolution to identify these structural features (Figs. 17(A-E)). This is because most of these types of faults probably become flatter at greater depths, and they do not penetrate deep into the crust (Eaton *et. al.*, 1977). However, gross features are identified in the shallow crustal model, such as a segment of the Crater Flat-Prospector Pass Caldera complex which probably is filled with a layer of low velocity material (G4, R4; Fig. 12-E). Other identified regional features include thickening of sediments or alluvium in a southerly direction towards the Amargosa Desert and the absence of roots for Yucca Mountain, Bare Mountain and Skull Mountain (Figs. 17(A-E)). The most noticeable thickening of sediments occurs on Line 2 where the thickness is 2.5 km. The thinnest layer of alluvium occurs at Bare Mountain, and this thin layer of sediments underlies a layer of high velocity material, producing significantly earlier first arrivals as indicated by the record section in Figure 16-E.

The total thickness of the shallow structure at Yucca Mountain area is about 3-4.5 km. This thickness represents the top two layers which collectively, have a high velocity gradient. These layers have velocities that range from  $2.1 \text{ kms}^{-1}$  near the surface (Line 1; Table 6A) to a maximum velocity of  $5.7 \text{ kms}^{-1}$  at the bottom of the layer (Line 3 East; Table 6-D). According to lithologic studies from drill-holes at Yucca Mountain (Spengler and Rosenbaum, 1980; Snyder and Carr, 1982) and shallow refraction studies (Pankratz,

1982), the second layer represents the Eleana formation. Velocities of  $4.5\text{-}5.3 \text{ km s}^{-1}$  with average densities of  $2.6 \text{ g cm}^{-3}$  have been reported by these studies. The velocities (Tables 6A-E) and densities for layer 2 from the gravity models (Tables 1-5) show a wider range, from  $4.0\text{-}5.80 \text{ km s}^{-1}$  and  $2.2\text{-}2.5 \text{ g cm}^{-3}$  respectively. Occurrence of small velocity inversions are possible in the shallow structures, especially in the top layer, due to the existence of volcanics in the sediments. Sediments which normally have a lower velocity than volcanic materials will produce a velocity inversion. This phenomenon is not observed in the velocity models, but the possibility cannot be eliminated.

In the section travel time inversion, the deeper velocity structures are compared with the average velocity depth function. In general, large deviations from the average velocity model occurred in the upper 10 - 12 km. At greater depths, the deviations were relatively smaller. These deviations indicate strong variations as a result of structural and lithologic variations in the upper 10 - 12 km of the crustal structure in the vicinity of Yucca Mountain. This supports the general conclusion of lateral heterogeneities in this area which result from occurrences of grabens and valleys, typical in this region. Smaller deviations in the deeper crust support the argument regarding the lack of deeper extent of these grabens or roots into the crust. The existence of these deviations and the fact that at depths greater than 15 km the mean velocity gradient is comparatively low, indicate a general homogeneity of deeper layers in terms of velocity and structure.

The deeper structures in the vicinity of Yucca Mountain contain a lower velocity gradient than the shallow structures with smaller lateral velocity variations. Velocity distributions for the north-south lines do not differ significantly, except for velocities in Line 2. The velocity model of Line 2 has progressively higher velocities at the 10 - 20 km depth range. The east-west velocity model of Line 4 also has considerably higher velocities at

this depth range. An apparent velocity of  $6.8 \text{ kms}^{-1}$  is used at 13 km depth to match the reflective amplitudes.

The deeper velocity structures contain a mid-crustal boundary and several intra-crustal boundaries as observed in Figures 17-(A-E). The velocity model of Line 4 (Fig. 17-E) contains a mid-crustal boundary at depths of 13 km as defined by reflected times. This boundary can be related to the boundary at depth of 14 km in Line 2 (Fig. 17-B). The velocity at the 13 km boundary ( $6.55 \text{ kms}^{-1}$ ) in Line 4 is closely correlated with the velocity at the 14 km boundary in Line 2 ( $6.55 - 6.6 \text{ kms}^{-1}$ ). These velocities correspond to the velocities above the interface. Velocities below the interface do not agree to each other; the velocity from Line 4 ( $6.8 \text{ kms}^{-1}$ ) is higher than the velocity from Line 2 ( $6.6 \text{ kms}^{-1}$ ). These observed boundaries in both Lines 1 and 4 lie beneath Mine Mountain and Yucca Mountain respectively (Fig. 18(a)).

Other boundaries at different depths are also observed in the final velocity models. Velocity models from Line 1 (Fig. 17-A) and Line 3 West (Fig. 17-C) have intra-crustal boundaries at 20-21 km depth. The distances at which the rays are reflected from this boundary correspond to 28-33 km away from shot point 1 in Line 1, and 35 - 43 km from shot point 3 in Line 3 West (Fig. 18(b)). The velocities above and below this boundary are identical to velocities in models derived from Line 1 and Line 3 West (Tables 6-A, and 6-C). These correlations (depth and velocity) result in the interpretation that the boundary model of Line 1 is identical to the boundary found in Line 3 West. Further to the east on Line 2, another reflector is observed at depths of 24 km. Compressional wave velocities at this boundary are higher than those found in Line 1 and Line 3 West. If these boundaries are connected, they will form a plane reflector with an apparent dip of  $8^\circ$  towards the east. Deeper reflectors are observed at depth of 28 km and 31 km in Line 3 East. These



reflectors are located beneath Yucca Mountain (Fig. 18 (c,d)). Even though these reflectors are only 3 km apart, the reflective phases that identified them are quite distinctive, as is evident in Figure 16-D. These boundaries have all been observed by Hoffman and Mooney (1984), except the boundary on Line 2 (Fig. 17-B).

The total crustal thickness as determined from secondary arrivals is 38 km from Line 3 East and 37 km from Line 3 West, both of which refers to a location beneath Yucca Mountain (Fig. 18(e)). The crustal thickness for this region agrees fairly well with Prodehl's result (1979). He reported the mean crustal thickness in this region is about 35 km which thins towards Ludlow, California. His analysis was based on an interpretation of a reversed seismic refraction profile from NTS to Ludlow. Pakiser and Hill (1963) reported a crustal thickness of 31 km, which is significantly less than the value determined in this study. They also interpreted a broadening of the crust from NTS northward, to a thickness of 36 km at Eureka and Elko, Nevada based on a seismic refraction profile from NTS to southern Idaho.

The profiles from Line 3 East and Line 3 West are of insufficient length to observe any refracted arrivals from the Moho. However, compressional wave velocities of the Moho discontinuity as determined from the reflected arrivals and amplitude analysis indicate a velocity of  $7.9 \text{ kms}^{-1}$ . This velocity agrees very well with other reported Moho ( $P_n$ ) velocities;  $7.84 \text{ kms}^{-1}$  (Pakiser and Hill, 1963),  $7.8 - 8.2 \text{ kms}^{-1}$  (Prodehl, 1970) and  $7.5 - 7.8 \text{ kms}^{-1}$  (Prodehl, 1979). In view of the fact that the  $P_n$  velocities in this study were obtained using reflected times and constrained by amplitude correlation, variations in the  $P_n$  velocities are surprisingly small. A fence diagram is constructed in Figure 19 showing the relationship of the velocity models from each of the profiles discussed here.

Amplitude analysis in this study is done by comparing the observed and theoretical amplitude along a single trace and along the record section. Exact correlation in magnitude for the observed and calculated is not expected since calculations for the theoretical amplitudes are not exact, but merely an approximation.

Seismograms towards the later parts of the record sections tend to have a higher energy in terms of amplitudes than the seismograms at closer distances (Line 3 East and Line 4, Figs. 16-D and E) Recording stations that record the high amplitude seismograms are located on thick alluvium. These sites correspond to areas of low altitude in Jackass Flats and Amargosa Desert (Line 4 and Line 3 East respectively; Fig. 9).

Isolated strong amplitude seismograms are observed in Line 3 West (80-85 km; Fig. 16-C), Line 2 (approximately 58 km; Fig. 16-B) and Line 4 (5-10 km; Fig. 16-E). These isolated cases may be the result of interference, focussing or site amplification. Local focussing effect may explain the high amplitude observed in Line 2. Inspection of the adjacent traces suggests that energy has been redirected towards the recording station at 58 km (Line 2; Fig. 16-B), resulting in the observation of low amplitudes at these traces. Similar explanation can be used for the observation of high amplitudes for seismograms recorded at 80,84 and 85 km range in Line 3 West (Fig. 15-C) and at 5 and 10 km range in Line 4 (Fig. 16-E). Local focussing and defocussing can be caused by near-surface structures such as cusps, valleys or any irregularities in the immediate vicinity of the recording site. Another possibility is site effect. Tucker and King (1984) have observed sediment amplifications of a factor of 2 in valleys.

Apart from the isolated cases of strong amplitudes, groups of recordings with strong amplitudes are also observed. These recordings occur at Line 2 (38-45 km; Fig. 16-B), Line 3 East (66-110 km; Fig. 16-D) and at Line 4 (47-57 km; Fig. 16-E). Sections in Line

2 and Line 4 intersect at Jackass Flats, between Shoshone Mountain to the north and Skull Mountain to the south. The amplitude changes in Lines 2, 3 East and 4 are abrupt as opposed to the synthetic modeling (Figs. 17-B, D, and E). The velocity models cannot predict this observed phenomenon. Irregularity in the interface surface, causing focussing and defocussing may be possible for isolated cases but it is unlikely since the synthetic section predicts high amplitude without introducing any irregularity to the interface. However, with the addition of site effects (higher impedance contrast) on a larger scale, with focussing and defocussing effects may be possible to explain the high amplitudes observed (King and Tucker, 1984).

Another seismic feature that is observed in the data set is diffraction. These diffractions are obvious in the divergence of the ray paths in the ray diagram of Line 4, at Bare Mountain and Yucca Mountain (Fig. 16-E) and in Line 2 at Skull Mountain (Fig. 16-B). Diffracted waves are typically caused by structures having dimensions less than or equal to the wavelength of the seismic wave.

Amplitude analysis has provided additional information in refining the interpreted velocity models in terms of velocity gradients. Although amplitude comparisons have been analyzed qualitatively, amplitudes are particularly sensitive to velocity gradients and only the finest structural details will affect the absolute amplitude. In addition, this analysis may be presented as a reconnaissance for future strong ground motion studies to check the hypothesis of site effects in Jackass Flats in comparison to site effects at Yucca Mountain.

A comparison between the preliminary model obtained by Hoffman and Mooney (1984) and the model obtained in this study shows no major difference. Good correlation between these two models occur in the shallow structure. Using *P*-wave delay times from fan-arrays and gravity contour maps, Hoffman and Mooney concluded that there exists a

thick layer of low velocity material at the surface, in the vicinity of Crater Flats and Yucca Mountain. This layer gets moderately thick under Jackass Flats and thins considerably beneath Bare Mountain and Skull Mountain. The crustal model obtained in this study agrees fairly well with their interpretation (Fig. 17-E). However, the thickness of the layer at Skull Mountain is greater than the thickness reported by Hoffman and Mooney. This discrepancy is probably caused by the picking errors of the first arrivals, since recordings at that distances (55 - 65 km) have highly emergent arrivals. Velocity comparisons between these models indicate that on the average, their assigned velocities are slightly less than those assigned in this study. Differences in the velocities can be explained by several factors. Firstly, layer depth can be traded off by changing the velocity within the layer. By increasing the thickness of a layer, the travel times can be set constant by decreasing the layer velocity. Another possibility is error in picking the arrival time and using different velocity distribution (Telford *et. al.*, 1976, Fig. 4.21).

In terms of deeper structures, Hoffman and Mooney had identified a reflection from a mid-crustal boundary at 15 km,  $\pm$  2 km below Yucca Mountain. They have identified two additional intra-crustal boundaries below Yucca Mountain at depths of 24 and 30 km. These boundaries seem to correspond very well to the boundaries determined in this study. However, they did not observe any additional intra-crustal boundary below Yucca Mountain (28 km, Line 3 East). No comparison can be made regarding the mid-crustal boundary at Mine Mountain (14 km deep, Fig. 6-B), since they did not interpret the data from that particular line. They have interpreted the total crustal thickness using Moho reflections to be 35 km thick. This is 2 - 3 km less than the value obtained in this study. Considering errors that may have been introduced in picking reflected arrivals and the inconsistency in recognizing the arrival of the reflected phase for different pickers, the above results agree

fairly well with each other. **SUMMARY AND CONCLUSION**

The crustal structure in the vicinity of Yucca Mountain is interpreted using seismic refraction profiles recorded by the USGS during the period of 1960-1982. The data comprised of recordings of nuclear explosions downwind in the northern part of NTS (north-south profile) and a recording of a chemical explosion at Beatty, Nevada (east-west profile). The refraction experiment was done as part of an on-going investigation of Yucca Mountain as one of the three potential sites for a geological nuclear waste repository.

The general procedure in analyzing the crustal structure in this area makes use of several forward methods and inverse method of travel-time inversion of  $t_p$ . Forward methods include two-dimensional ray-tracing, gravity modeling and amplitude analysis of selected arrivals. The interpretation and analysis procedure is divided into three stages. The first stage is to determine the shallow structure (upper 3-4 km) and makes travel-time adjustments to correct for the shallow structure. The second stage involves travel-time inversion using the delay-time method. At this stage, deeper structures are determined using the assumption that the structure consist of homogeneous flat lying layers. This assumption is reasonable since gross horizontal geologic correlation is justified when considering bulk crustal structure. The third and final stage of the data analysis and interpretation is to combine the shallow structures (from stage 1) and deeper structures (from stage 2) to form a two-dimensional model where rays are traced through by trial and error to match the observed travel-times. Synthetic arrivals are then calculated from theoretical travel-times to fit the observed amplitude arrivals in an iterative manner.

Shallow velocity models obtained in Stage 1 on each of the two profiles, generally show good correlation with their corresponding gravity models. Some variations occur at

## SUMMARY AND CONCLUSION

The crustal structure in the vicinity of Yucca Mountain is interpreted using seismic refraction profiles recorded by the USGS during the period of 1980-1982. The data comprised of recordings of nuclear explosions detonated in the northern part of NTS (north - south profile) and a recording of a chemical explosion at Beatty, Nevada (east - west profile). The refraction experiment was done as part of an on-going investigation of Yucca Mountain as one of the three potential sites for a geological nuclear waste repository.

The general procedure in analyzing the crustal structure in this area makes use of several forward methods and inverse method of travel-time inversion of  $\tau(p)$ . Forward methods include two-dimensional ray-tracing, gravity modeling and amplitude analysis of selected arrivals. The interpretation and analysis procedure is divided into three stages. The first stage is to determine the shallow structure (upper 3-4 km) and makes travel-time adjustments to correct for the shallow structure. The second stage involves travel-time inversion using the delay-time method. At this stage, deeper structures are determined using the assumptions that the structures consist of homogeneous flat lying layers. This assumption is conceivable since gross horizontal geologic stratification is justified when considering bulk crustal structures. The third and final stage of the data analysis and interpretation is to combine the shallow structures (from stage 1) and deeper structures (from stage 2) to form a two-dimensional model where rays are traced through by trial and error to match the observed travel-times. Synthetic arrivals are then calculated from theoretical travel-times to fit the observed amplitude arrivals in an iterative manner.

Shallow velocity models obtained in Stage 1 on each of the five profiles, generally show good correlation with their corresponding gravity models. Some variations occur at

places where there are strong local heterogeneity. The density models are obtained by modeling high frequency gravity data which would indicate gravity anomalies resulting from near-surface structures.

In the second stage, a comparison of the velocity model from each profile with the average model indicates, to some extent, the layer homogeneity. From the deviations, it can be concluded that heterogeneity occurs in the upper 10-12 km with strong lateral variations in the upper 5 km. Below this depth, the layers are more homogeneous, since deviations from the average model are minimal.

Synthetic analysis provides additional information for the velocity models in each layer, since amplitudes are sensitive to velocity gradients. It is hypothesized that site effects, focussing and defocussing at the vicinity of the recorder, all contribute to the amplitude amplifications in the sediments. Strong local variations produced diffraction waves at Yucca Mountain and at Bare Mountain (Line 4). Amplitude analysis also provides a means of reconnaissance for future studies of strong ground motion in Yucca Mountain and Jackass Flats.

The crustal structure in the vicinity of Yucca Mountain shows heterogeneities in its upper part and becomes more uniform as depth increases. Depth to the basement is maximum at Crater Flat within the Prospector Pass-Crater Flats caldera complex. The depth of the caldera is approximately 3 km and it is filled with a thick layer of low velocity material. A mid-crustal boundary at 13-14 km deep correlates with a boundary having the same layer velocity near Skull Mountain. Other boundaries are observed at approximately 20 km, 28 km, and 31 km. Studies by Prodehl (1979) show no indication of any mid-crustal boundaries in the NTS region. Total crustal thickness is between 37-38 km with Moho velocity of  $7.9 \text{ km s}^{-1}$ .

In a comparison with a preliminary interpretation of this data set from Hoffman and Mooney (1984), a similarity is observed at the depths and in the number of crustal boundaries. However, they did not observe a reflector at 14 km in Line 2. Generally, no major deviation occurs between both models in terms of velocity and crustal thickness. Their total crustal thickness was reported as 35 km, which is slightly less than the thickness determined in this study.

Table 1. Velocity-density cross-sections for different sections in Line 1.

Table 2. Velocity cross-sections for each line: (A) Line 1; (B) Line 2; (C) Line 3.

Width (km) Line 1: 100; Line 2: 100; Line 3: 100.



LIST OF TABLES

- Table 1. Velocity-density relationship for shallow structures in Line 1.
- Table 2. Velocity-density relationship for shallow structures in Line 2.
- Table 3. Velocity-density relationship for shallow structures in Line 3 West.
- Table 4. Velocity-density relationship for shallow structures in Line 3 East.
- Table 5. Velocity-density relationship for shallow structures in Line 4.
- Table 6. Velocity specification in each layer for: (A) Line 1; (B) Line 2; (C) Line 3 West; (D) Line 3 East; (E) Line 4. Line 6.

Layer	Density (kg/m <sup>3</sup> )	Velocity (cm/sec)
1	1.18 - 2.2	1 - 2.5
2	1.2 - 2.5	2.5 - 5.0
3	2.5	5.0 - 10.0

Layer	Density (kg/m <sup>3</sup> )	Velocity (cm/sec)
1	1.18 - 2.2	1 - 2.5
2	2.2	2.5 - 5.0
3	2.5	5.0 - 10.0

UNIVERSITY OF CALIFORNIA  
 LIBRARY

Table 1

Layer	Density (g/cc)	Velocity (km/sec)
1	1.8 - 1.9	1.8 - 2.4
2	2.2 - 2.5	4.0 - 5.7
3	2.6	5.3 -

Table 2

Layer	Density (g/cc)	Velocity (km/sec)
1	1.8 - 2.1	2.1 - 3.5
2	2.3 - 2.5	4.0 - 5.7
3	2.6	5.8 -

Table 3

Layer	Density (g/cc)	Velocity (km/sec)
1	1.9 - 2.0	2.0 - 2.5
2	2.3	4.0 - 5.5
3	2.6	5.1 -

Table 4

Layer	Density (g/cc)	Velocity (km/sec)
1	1.8 - 1.9	1.8 - 2.3
2	2.3 - 2.4	4.0 - 5.7
3	2.6	5.1 -

Table 5

Layer	Density (g/cc)	Velocity (km/sec)
1	1.9	2.0 - 3.65
2	2.25 - 2.4	4.05 - 5.75
3	2.6	5.73 -

Table 6-A

Layer	Horizontal distance (km)				
	0.0	40.0	50.0	60.0	65.0
	Velocity (km/sec)				
1	2.4	2.2	2.4	2.5	2.1
	2.5	2.7	2.7	2.7	2.3
2	5.3	5.2	5.4	5.4	5.0
	5.4	5.3	5.6	5.6	5.5
3	5.45	5.40	5.85	5.70	5.65
	5.50	5.80	5.90	6.10	6.10
4	6.10	6.10	6.10	6.10	6.10
	6.20	6.20	6.20	6.20	6.20
5	6.30	6.30	6.30	6.30	6.30
	8.30	8.30	8.30	8.30	8.30

Table 6-B

Layer	Horizontal distance (km)					
	0.0	38.0	40.0	45.0	50.0	60.0
	Velocity (km/sec)					
1	2.2	2.2	2.4	2.5	2.2	2.2
	3.0	3.2	3.5	2.8	2.5	2.4
2	5.5	5.5	5.6	5.5	5.0	4.0
	5.7	5.7	5.8	5.8	5.5	5.0
3	6.20	6.20	6.10	6.20	6.10	6.10
	6.25	6.30	6.35	6.35	6.35	6.35
4	6.30	6.35	6.4	6.4	6.4	6.4
	6.55	6.55	6.6	6.6	6.6	6.6
5	6.60	6.60	6.60	6.60	6.60	6.60
	6.75	6.75	6.75	6.75	6.75	6.75
6	6.80	6.80	6.80	6.80	6.80	6.80
	8.30	8.30	8.30	8.30	8.30	8.30

Table 6-C

Layer	Horizontal distance (km)				
	0.0	40.0	62.0	75.0	90.0
	Velocity (km/sec)				
1	2.4	2.4	2.6	2.3	2.3
	2.3	2.5	2.8	2.5	2.5
2	5.0	5.0	5.3	5.3	5.3
	5.3	5.3	5.5	5.6	5.6
3	5.35	5.40	5.70	5.75	5.65
	5.50	5.70	6.10	6.10	6.10
4	6.1	6.1	6.2	6.2	6.2
	6.20	6.20	6.20	6.20	6.20
5	6.30	6.30	6.30	6.30	6.30
	6.80	6.80	6.80	6.80	6.80
6	7.90	7.90	7.90	7.90	7.90
	8.30	8.30	8.30	8.30	8.30

Table 6-D

Layer	Horizontal distance (km/sec)					
	0.0	45.0	50.0	60.0	95.0	110.0
	Velocity (km/sec)					
1	2.4	2.2	2.5	2.5	2.2	2.2
	2.3	3.0	3.35	3.0	2.5	2.5
2	4.9	4.2	5.7	5.7	5.0	5.0
	5.0	4.5	5.75	5.80	5.5	5.5
3	5.30	5.70	5.80	5.90	5.80	5.80
	5.50	5.90	6.10	6.20	6.20	6.20
4	6.10	6.10	6.25	6.25	6.25	6.25
	6.30	6.30	6.30	6.30	6.30	6.30
5	6.40	6.40	6.40	6.40	6.40	6.40
	6.60	6.60	6.60	6.60	6.60	6.60
6	6.70	6.70	6.70	6.70	6.70	6.70
	6.90	6.90	6.90	6.90	6.90	6.90
7	7.90	7.90	7.90	7.90	7.90	7.90
	8.30	8.30	8.30	8.30	8.30	8.30



## LIST OF FIGURES

- Figure 1. General geologic map of the Nevada and western United States. The area of interest is enclosed in the box. (From Prodehl, 1979).
- Figure 2-A. Generalized geologic map of region of refraction survey (Healey and Miller 1962).
- Figure 2-B. Relationship between calderas in the Yucca Mountain area. (From Carr, 1984).
- Figure 3. Geologic cross-section across Crater Flat and Yucca Mountain (location of B-B' refer to Figure 2). (From Snyder and Carr, 1982).
- Figure 4. Location of shallow refraction profiles and drill holes (Pankratz, 1982).
- Figure 5. Aeromagnetic Yucca Mountain and vicinity. (From Boynton and Vargo, 1963).
- Figure 6. Gravity anomaly contour map of Yucca Mountain and vicinity (Healey and Miller, 1962).
- Figure 7. Contour map of  $P_n$  velocity and crustal thickness from deep refraction experiments (Prodehl, 1979). Dashed lines indicate contour lines for crustal thickness, and the solid line indicate contour line of  $P_n$  velocity ( $7.8 \text{ kms}^{-1}$ ).
- Figure 8. Location of earthquakes recorded by USGS Denver (1981).
- Figure 9. Location of the seismic refraction profiles in this study.
- Figure 10. System response curve (recorder and seismometer response). (From Sutton, 1984).
- Figure 11. Record section of data collected from each line. Traces are plotted normalized to maximum amplitude and reduced to  $6 \text{ kms}^{-1}$ . (A) Line 1 (B) Line 2 (C) Line 3



East (D) Line 3 West (E) Line 4

Figure 12. Shallow velocity and density structures from ray-tracing and gravity modeling.

(A) line 1 (B) Line 2 (C) Line 3 West (D) Line 3 East (E) Line 4.

Figure 13. A comparison between corrected and corrected travel time data with the travel time fit for the average velocity model drawn through the corrected data.

Figure 14. (A) Extremal velocity bounds for the combined data (bold lines) with the average model. (B)  $T(p)$ ; (C)  $X(p)$ ; and cross over constraints ( $0.1516 < p < 0.1859$  (s/km);  $1 < T < 5$  (sec);  $7 < X < 27$  (km) ) used in the inversion.

Figure 15. Extremal velocity-depth bounds (bold) with specific velocity models for (A) Line 1 (B) Line 2 (C) Line 3 West (D) Line 3 East (dashed line indicate average extremal bounds) (E) Line 4

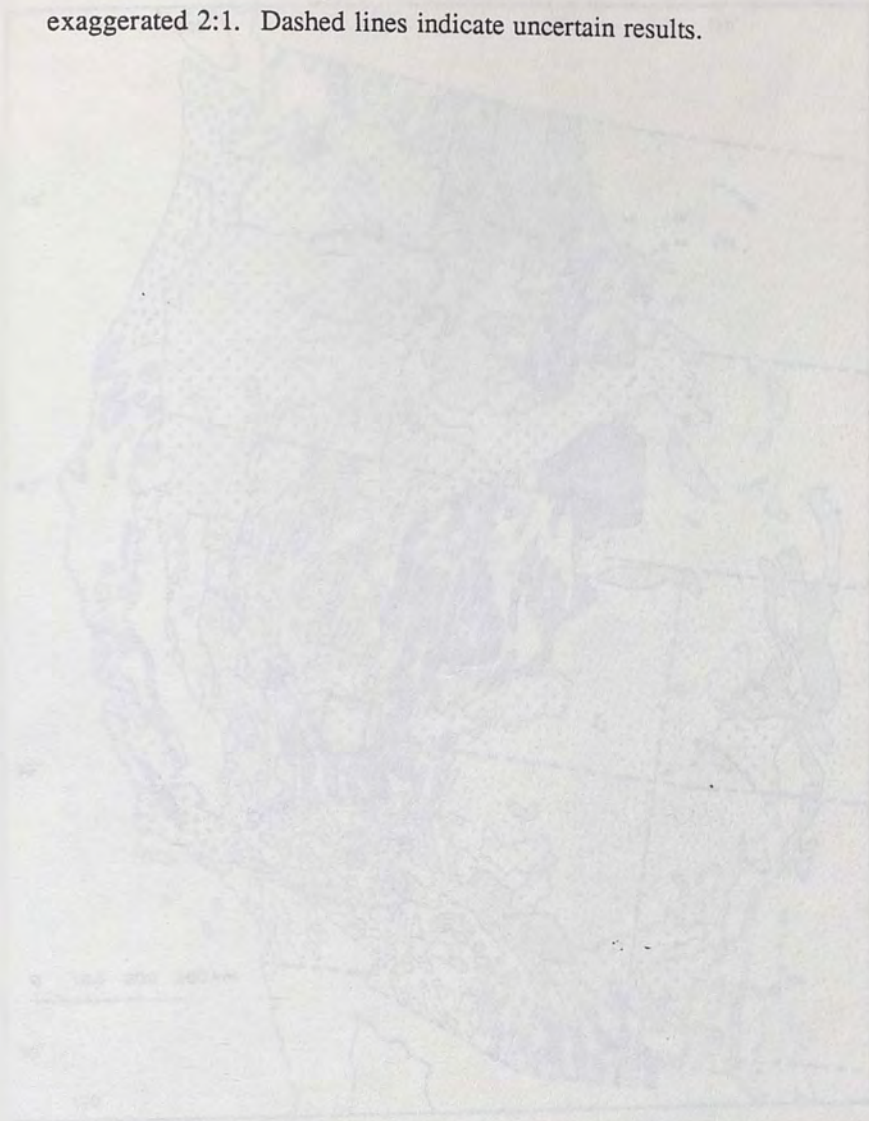
Figure 16. Combination of ray-diagram, record section (amplitude scaled to 1/distance) and synthetic section for: (A) Line 1 (B) Line 2 (C) Line 3 West (D) Line 3 East (E) Line 4

Figure 17. Final velocity models from: (A) Line 1 (B) Line 2 (C) Line 3 West (D) Line 3 East (E) Line 4. Velocity specifications in each layers are given in Table 6(A-E).

Figure 18. Simplified map showing the relationships of refraction lines and location of boundaries at (a) mid-crustal boundary at 13-14 km (b) intra-crustal boundary at 20-21 km (c) possible additional boundary at 24 km (d) deep crustal boundaries at 28 and 31 km (e) reflection from Moho.

Figure 19. Velocity fence diagram under Yucca Mountain viewed from S 40° W, from the Pacific towards North east. Enlargement from box in Figure 18. The depth is

exaggerated 2:1. Dashed lines indicate uncertain results.

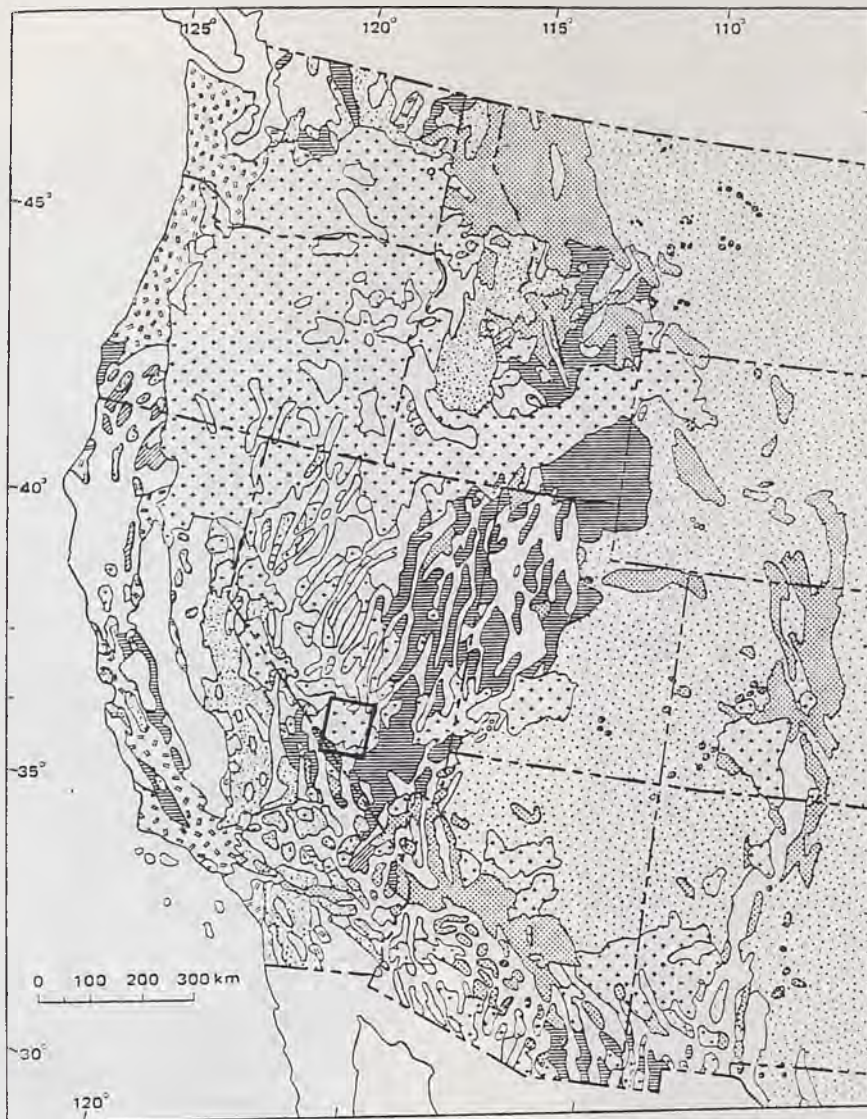


EXPLANATION

- Contour interval 100 feet
- Water divide of the range
- Principal drainage basins
- Secondary drainage basins
- Highway
- Railroad
- City
- County seat
- State boundary

FIGURE 1

nnvu^s f ujniri



## EXPLANATION

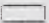



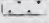


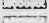
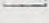
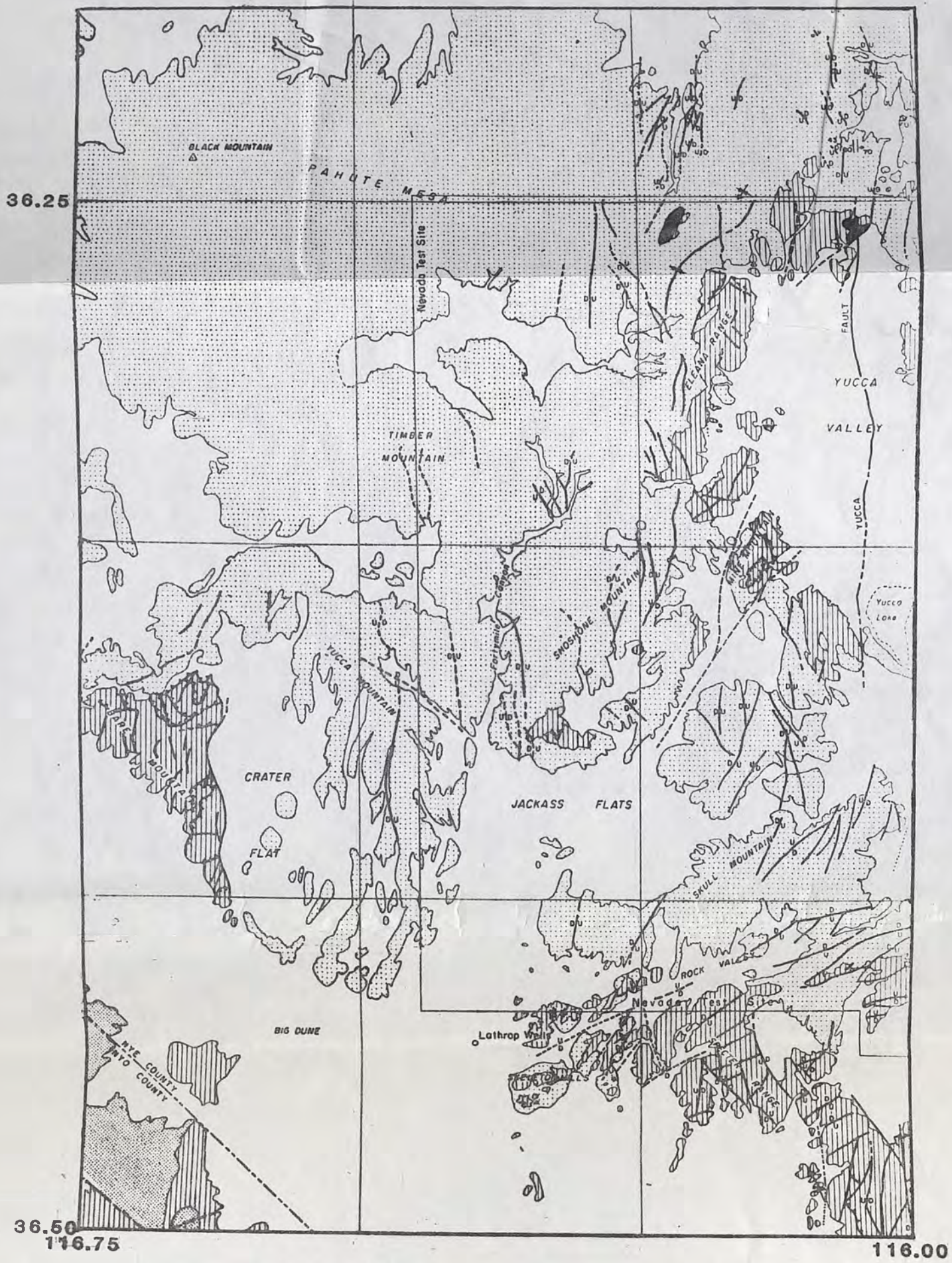
-  Terrestrial basin fill of Tertiary and Quaternary age
-  Marine deposits of Tertiary age
-  Miogeosynclinal deposits and shelf deposits of Paleozoic and Mesozoic age
-  Eugeosynclinal deposits of Paleozoic and Mesozoic age
-  Terrestrial volcanic rocks of Tertiary and Quaternary age
-  Granitic and other intrusive rocks of Mesozoic and Tertiary age
-  Ultramafic rocks
-  Precambrian rocks
-  Platform deposits overlying basement rocks of Precambrian age

FIGURE 1



EXPLANATION

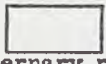




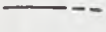
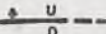





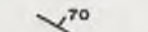
- |  |  |
|--|--|
| <p> Quaternary rocks</p> <p> Tertiary rocks</p> <p> Mesozoic(?) rocks</p> <p> Paleozoic and Precambrian rocks</p> <p> Precambrian crystalline rocks</p> <p> Contact<br/>Dashed where inferred</p> <p> Fault, showing dip<br/>Dashed where inferred or concealed.<br/>U, upthrown side; D, downthrown side</p> | <p> Strike slip fault<br/>Arrows show direction of relative movement</p> <p> Thrust fault<br/>Sawteeth on upper plate. Dashed where inferred or concealed</p> <p> Anticline<br/>Dashed where inferred</p> <p> Syncline<br/>Dashed where inferred</p> <p> Overturned syncline<br/>Showing direction of plunge. Dashed where inferred</p> <p> Strike and dip of beds</p> |
|--|--|



FIGURE 2 - A

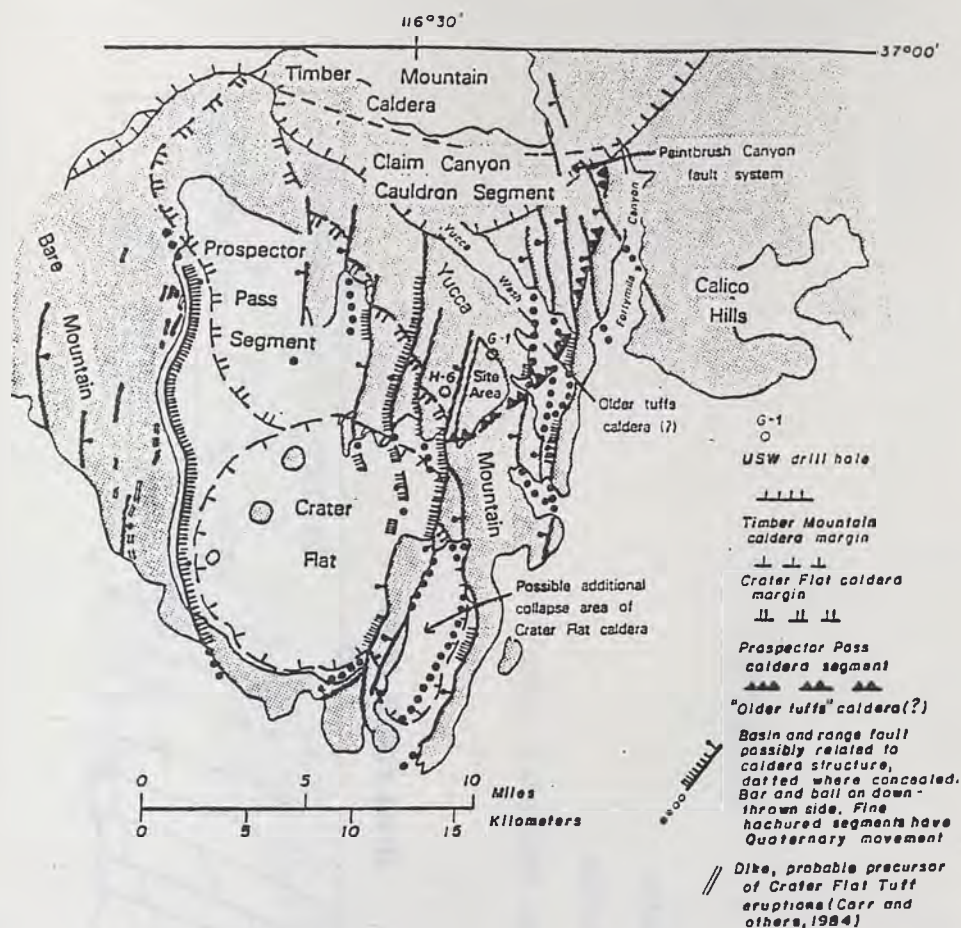
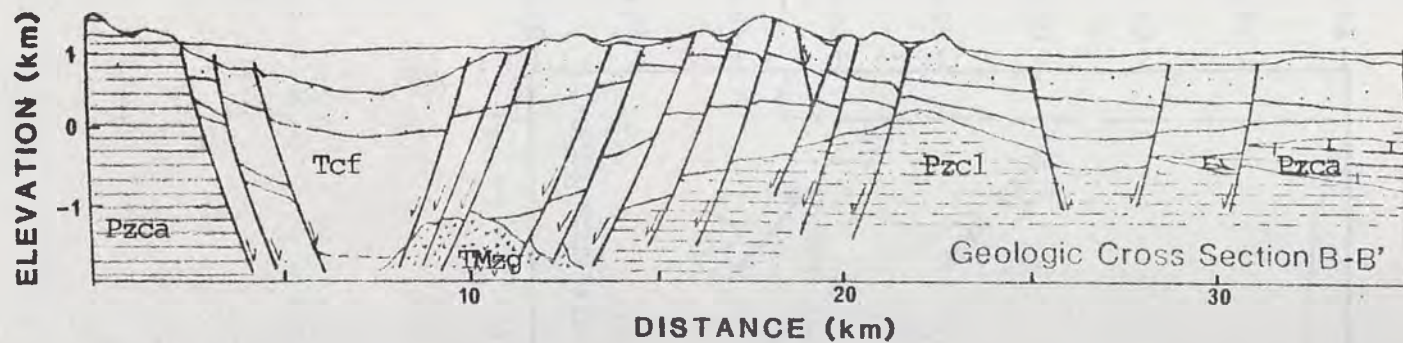


FIGURE 2-B



EXPLANATION

- Pzca Lower and middle Paleozoic carbonate rocks
- Pzcl Upper Paleozoic clastic rocks
- TMzg Mesozoic of Tertiary granite
- Tcf Crater Flat Tuff

FIGURE 3

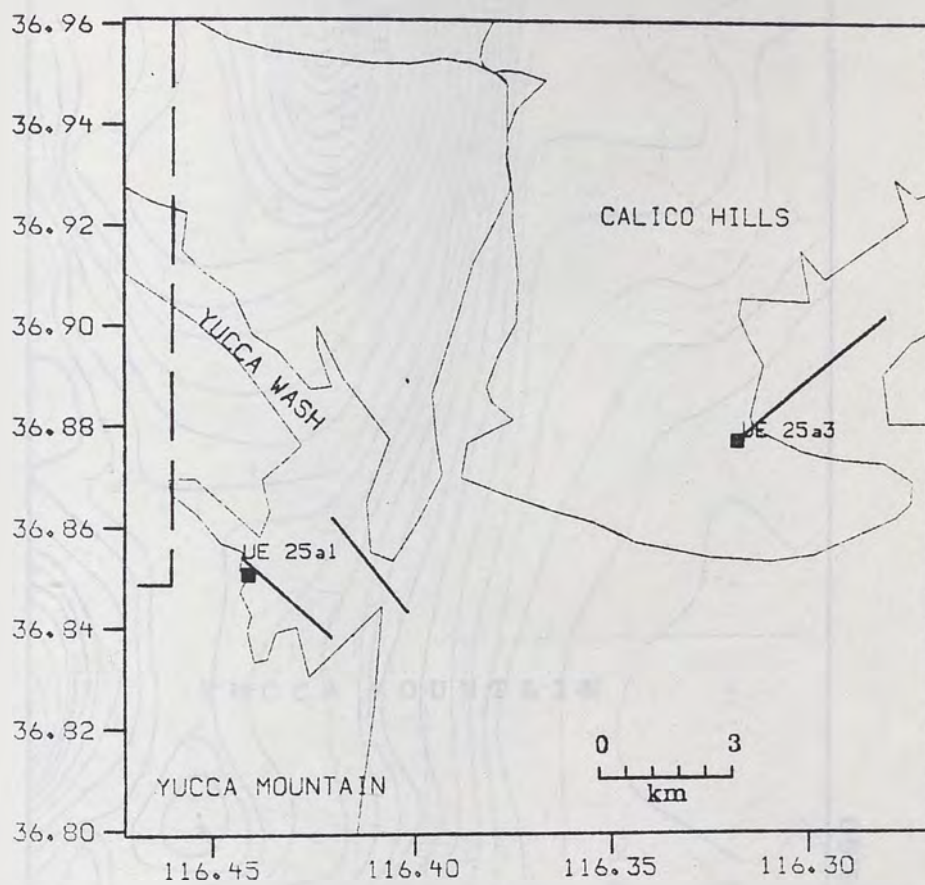


FIGURE 4

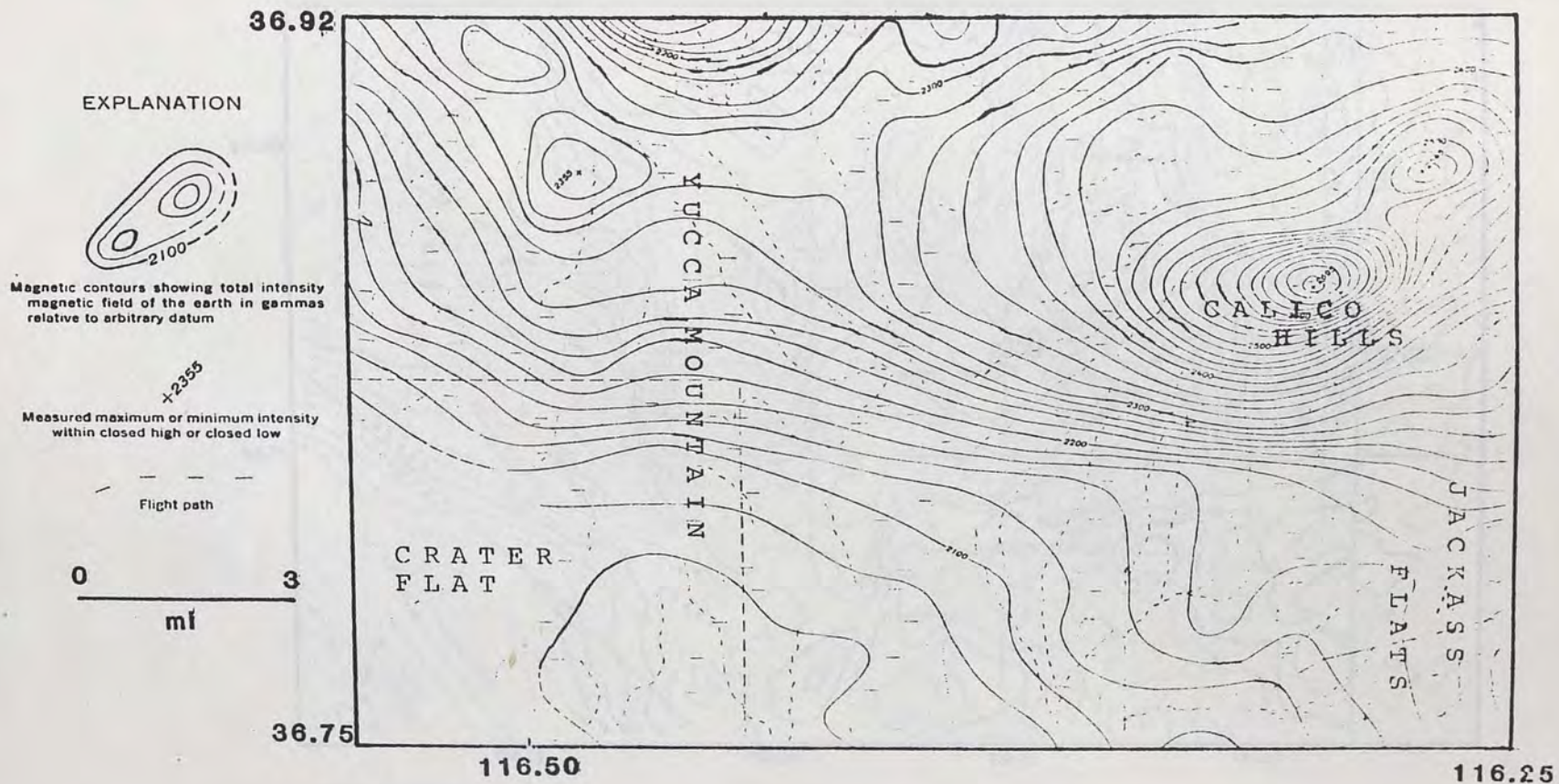
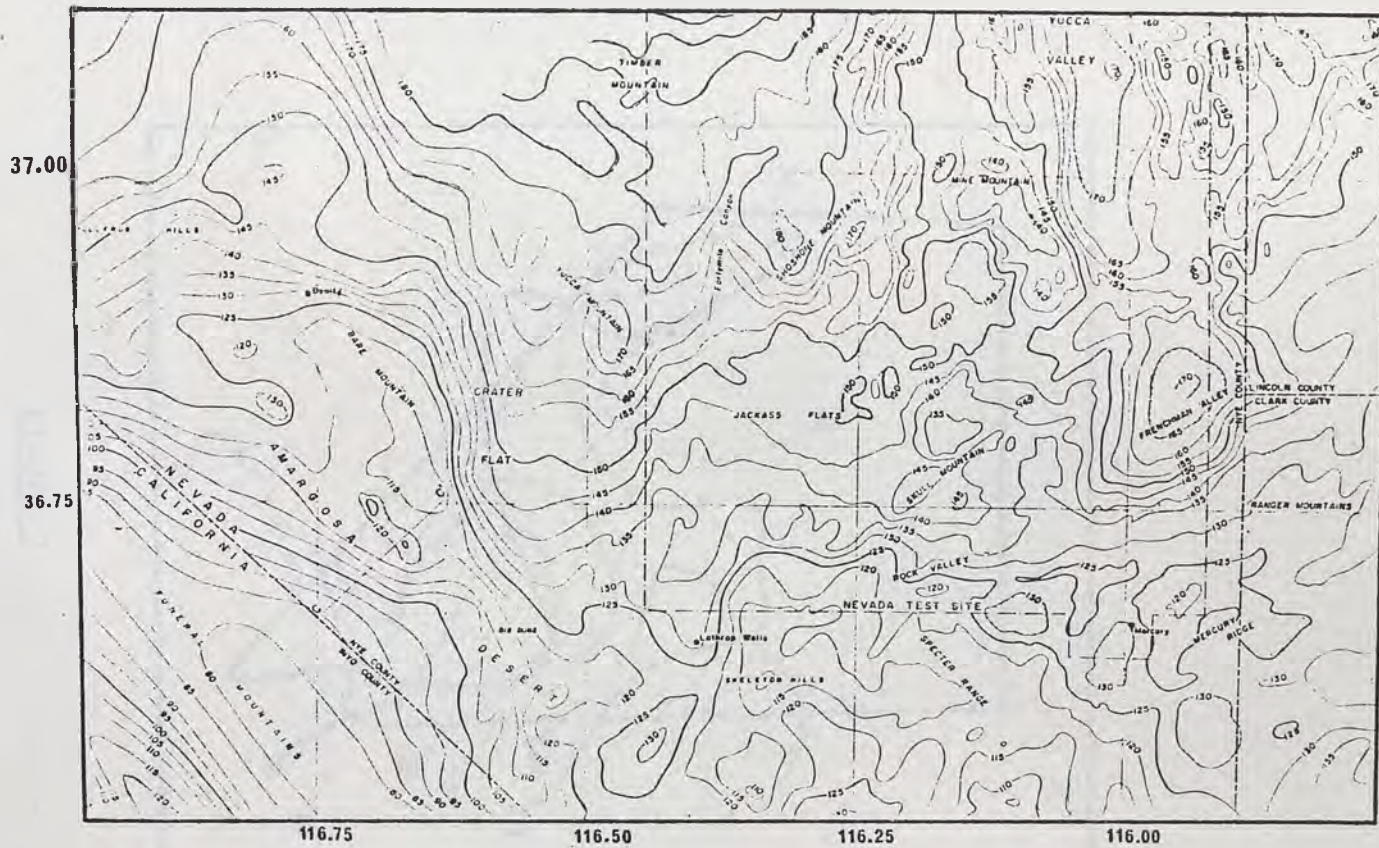


FIGURE 5





EXPLANATION

—— 140 ——

Gravity contour (5 mgals interval)

FIGURE 6

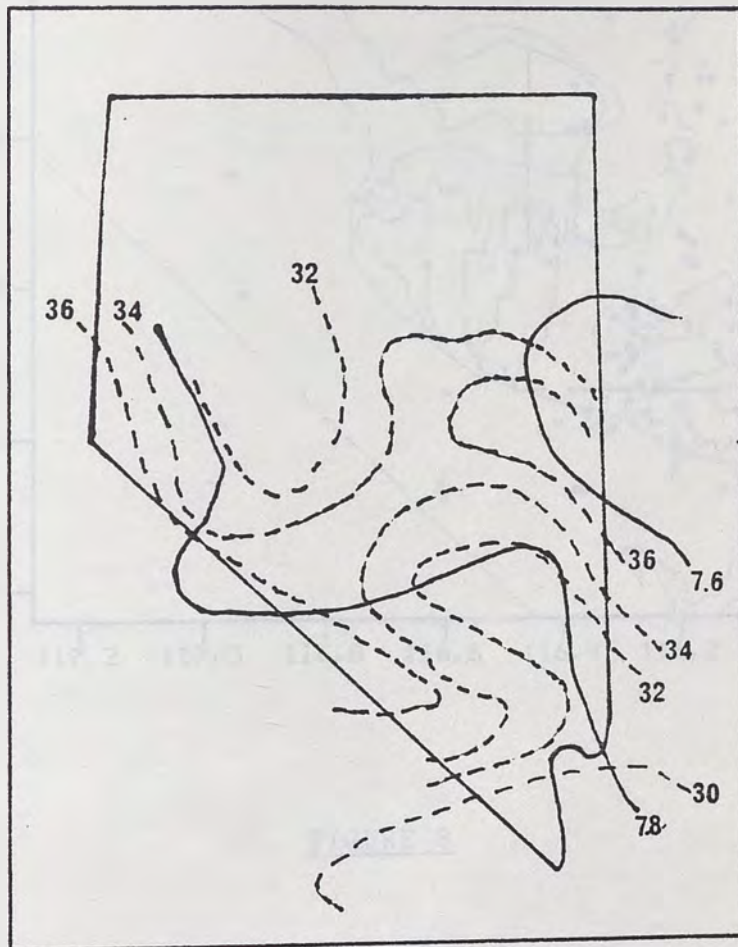


FIGURE 7

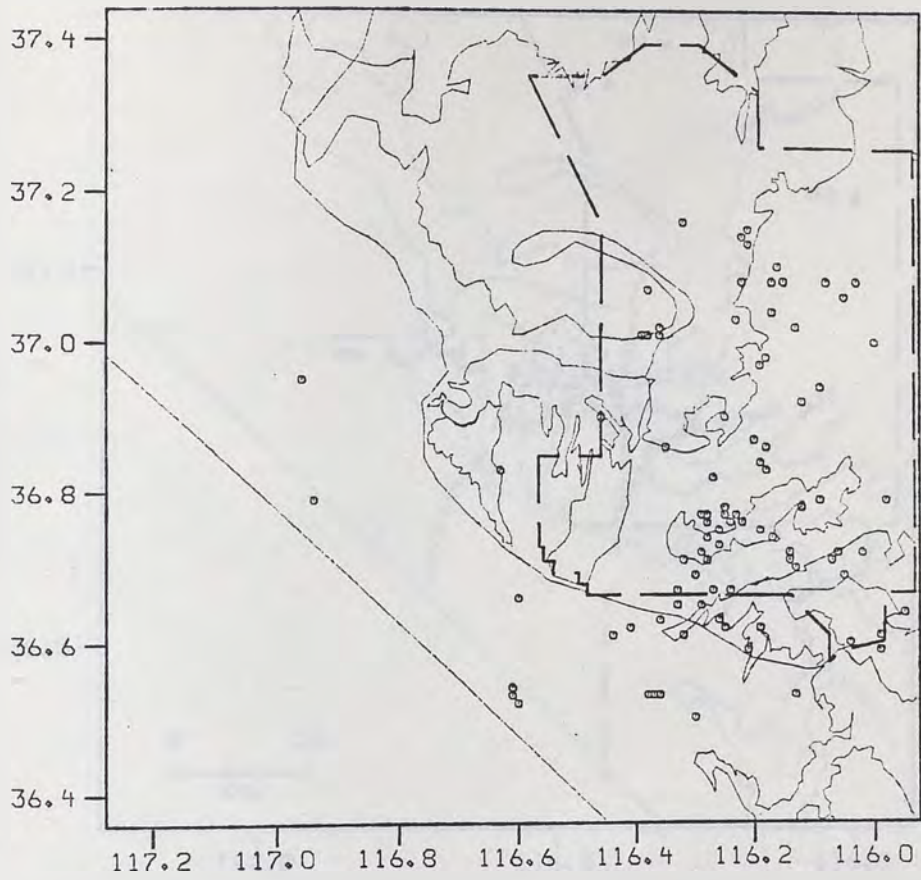


FIGURE 8

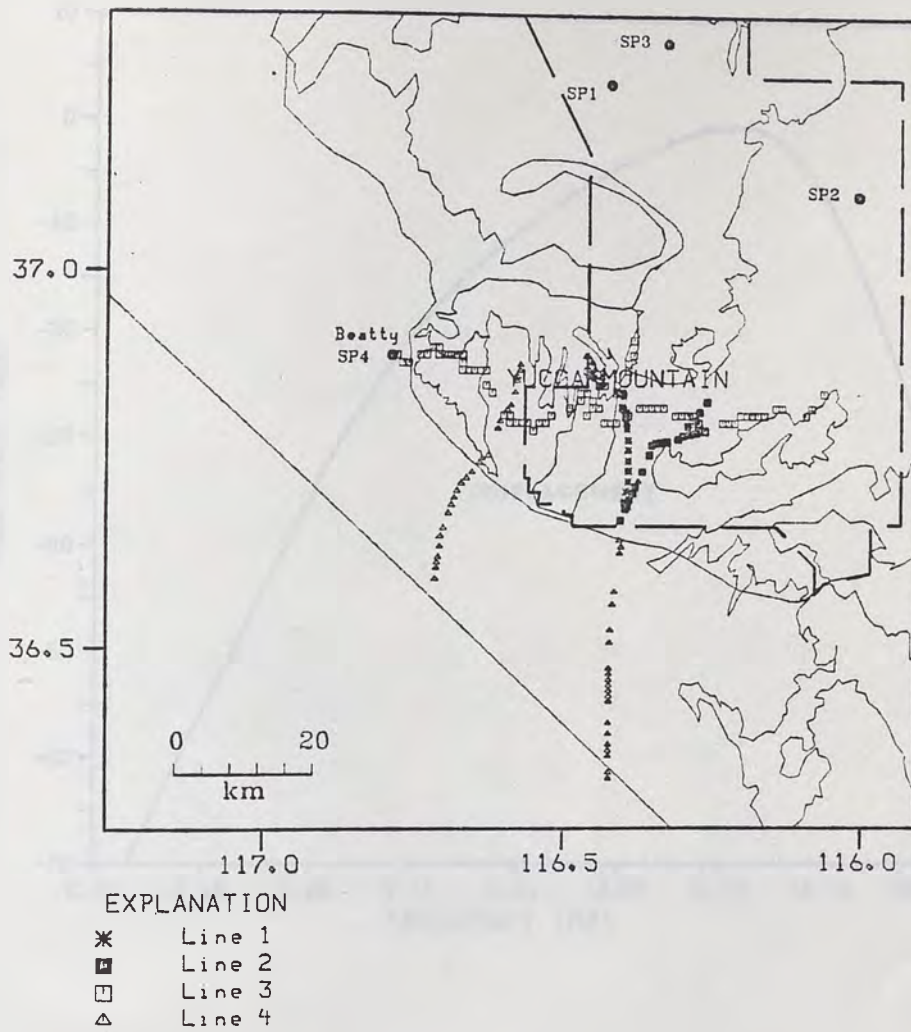


FIGURE 9

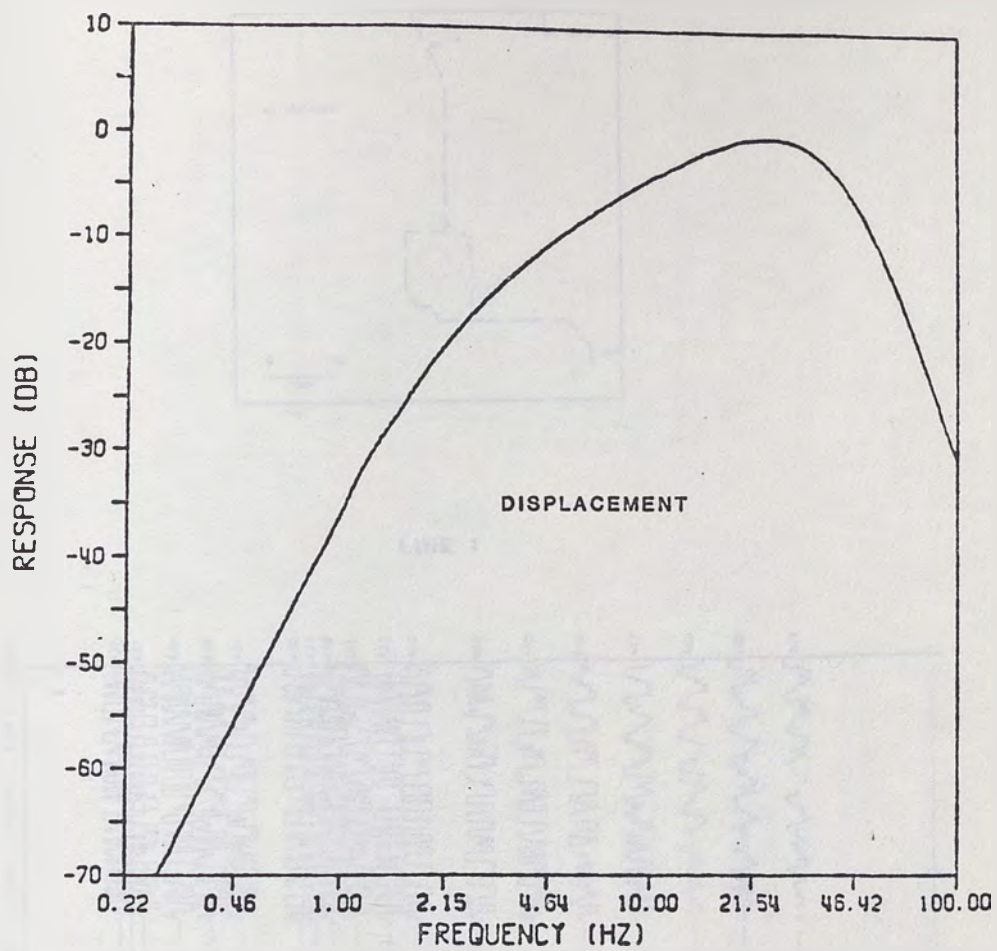
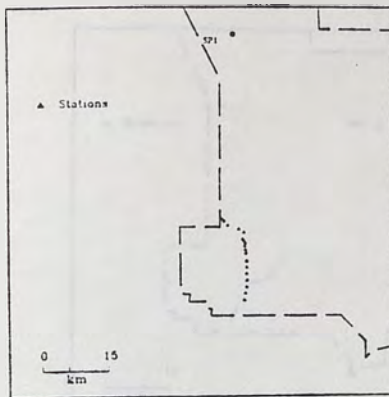


FIGURE 10



LINE 1

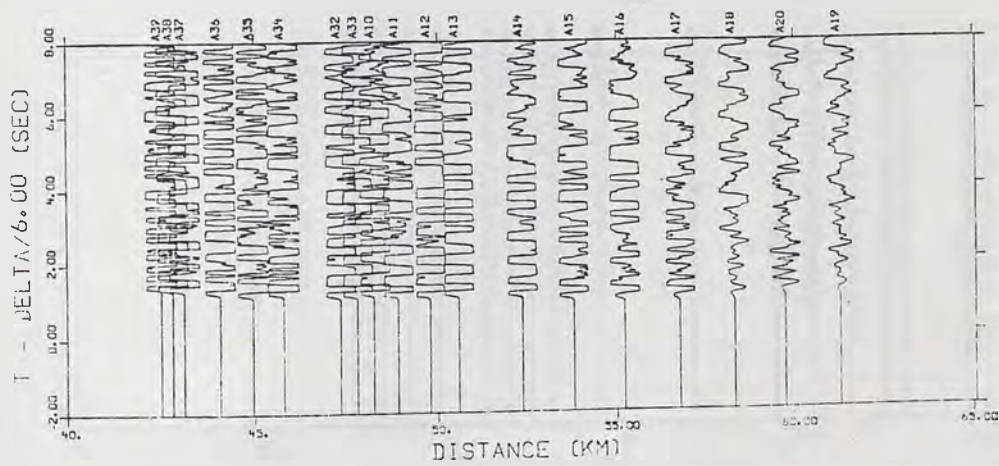


FIGURE 11-A

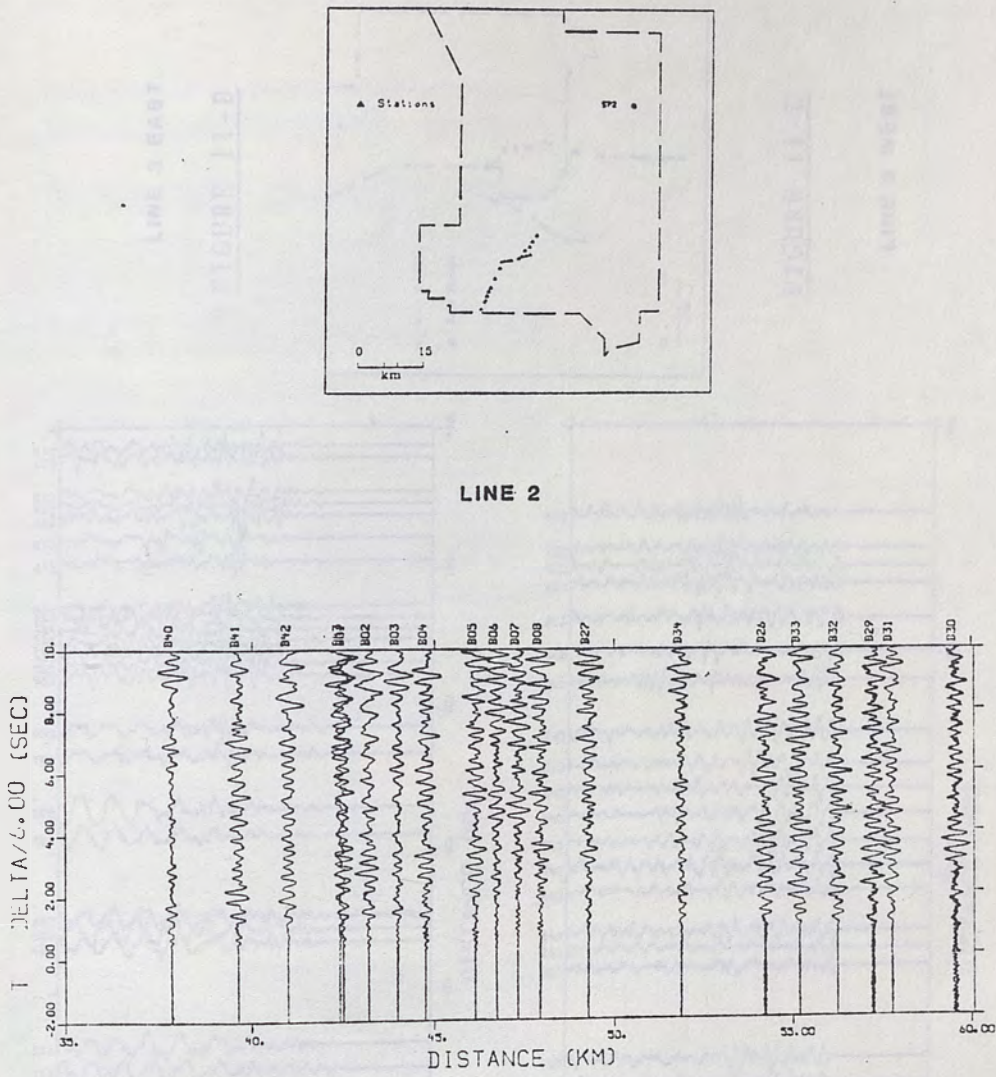
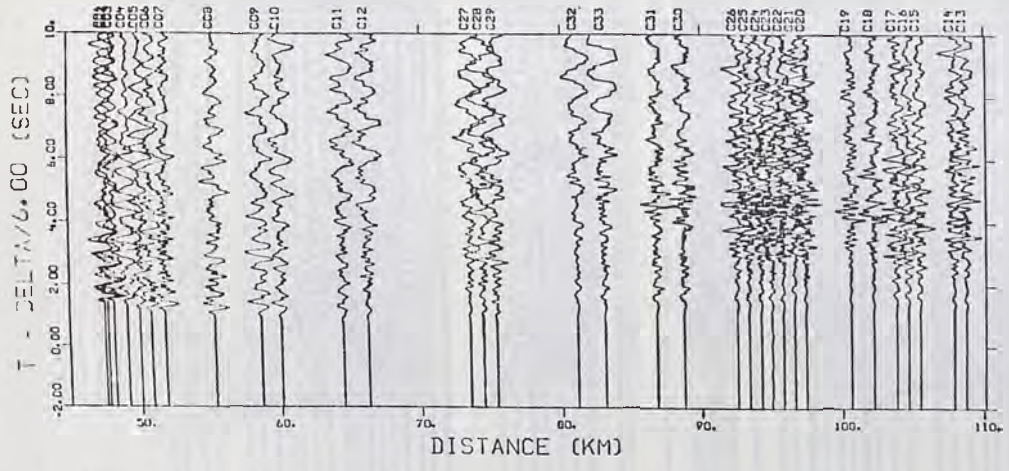


FIGURE 11-B



LINE 3 EAST

FIGURE 11-D

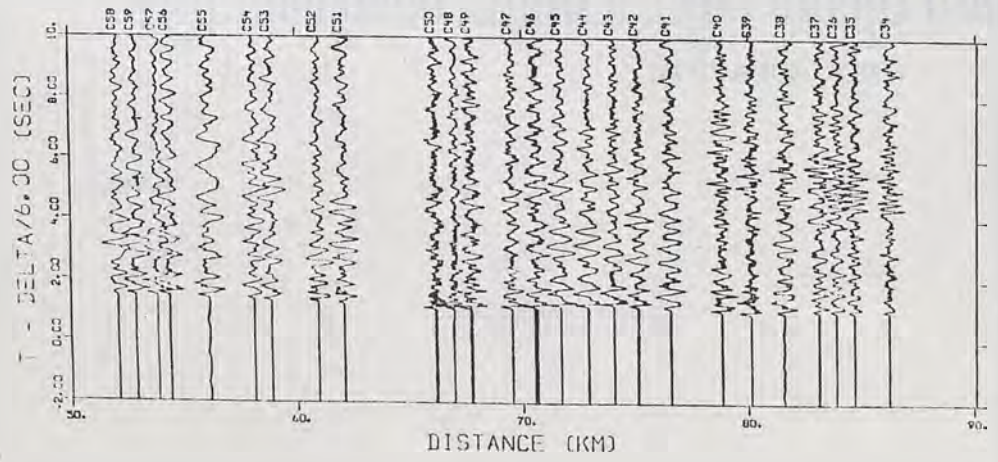
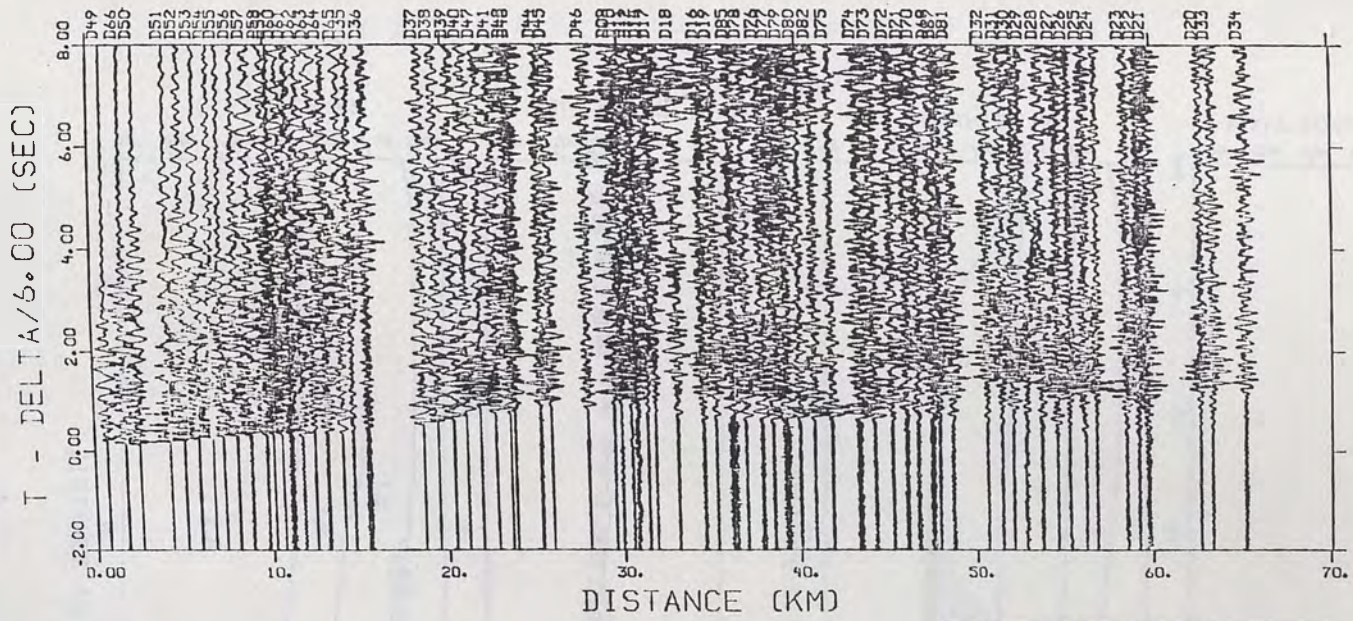


FIGURE 11-C

LINE 3 WEST

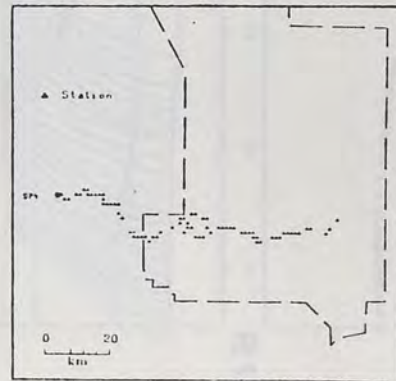






LINE 4

FIGURE 11-E



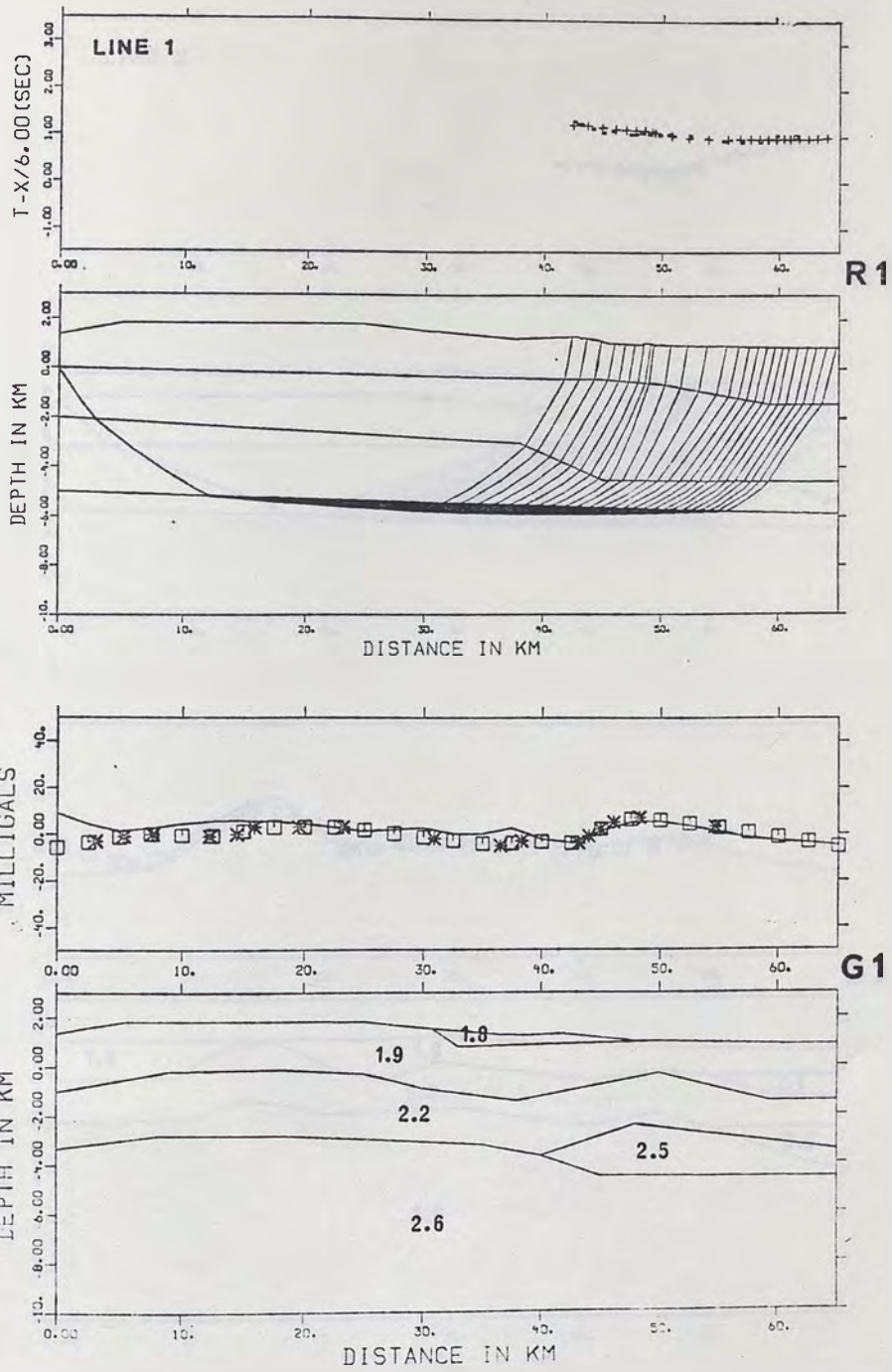
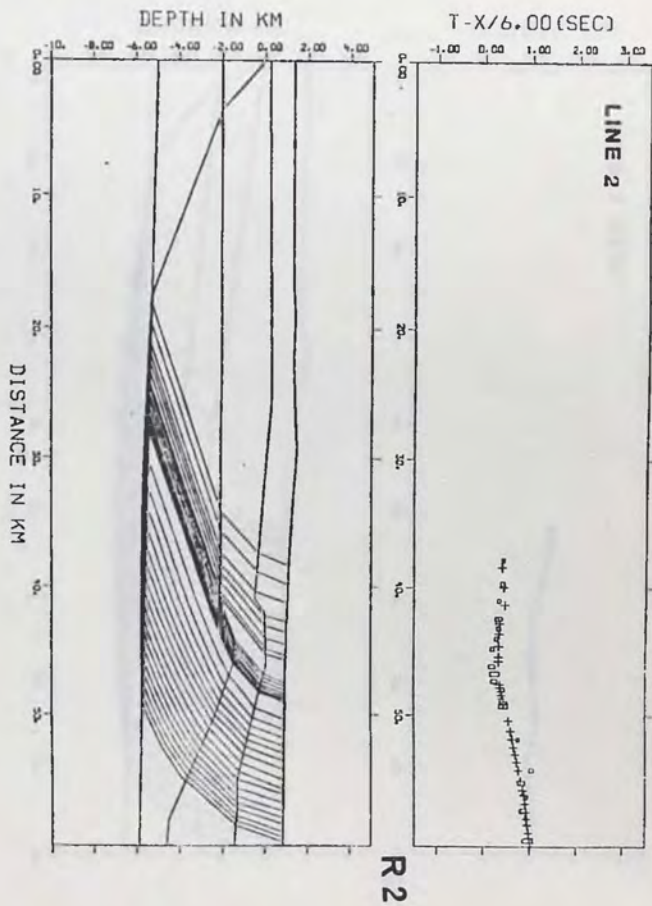
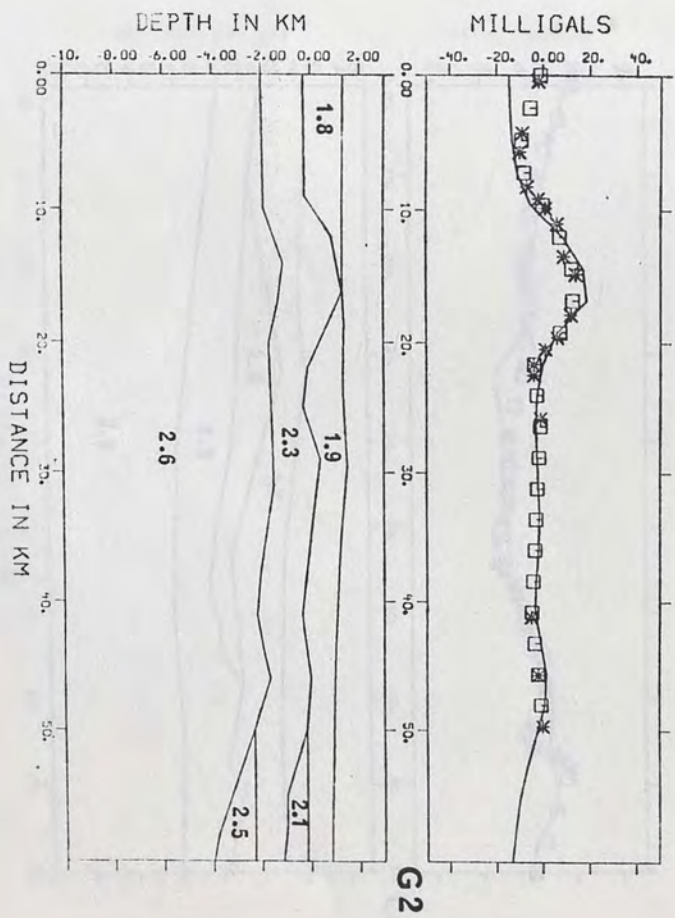


FIGURE 12-A



R2



G2

FIGURE 12-B

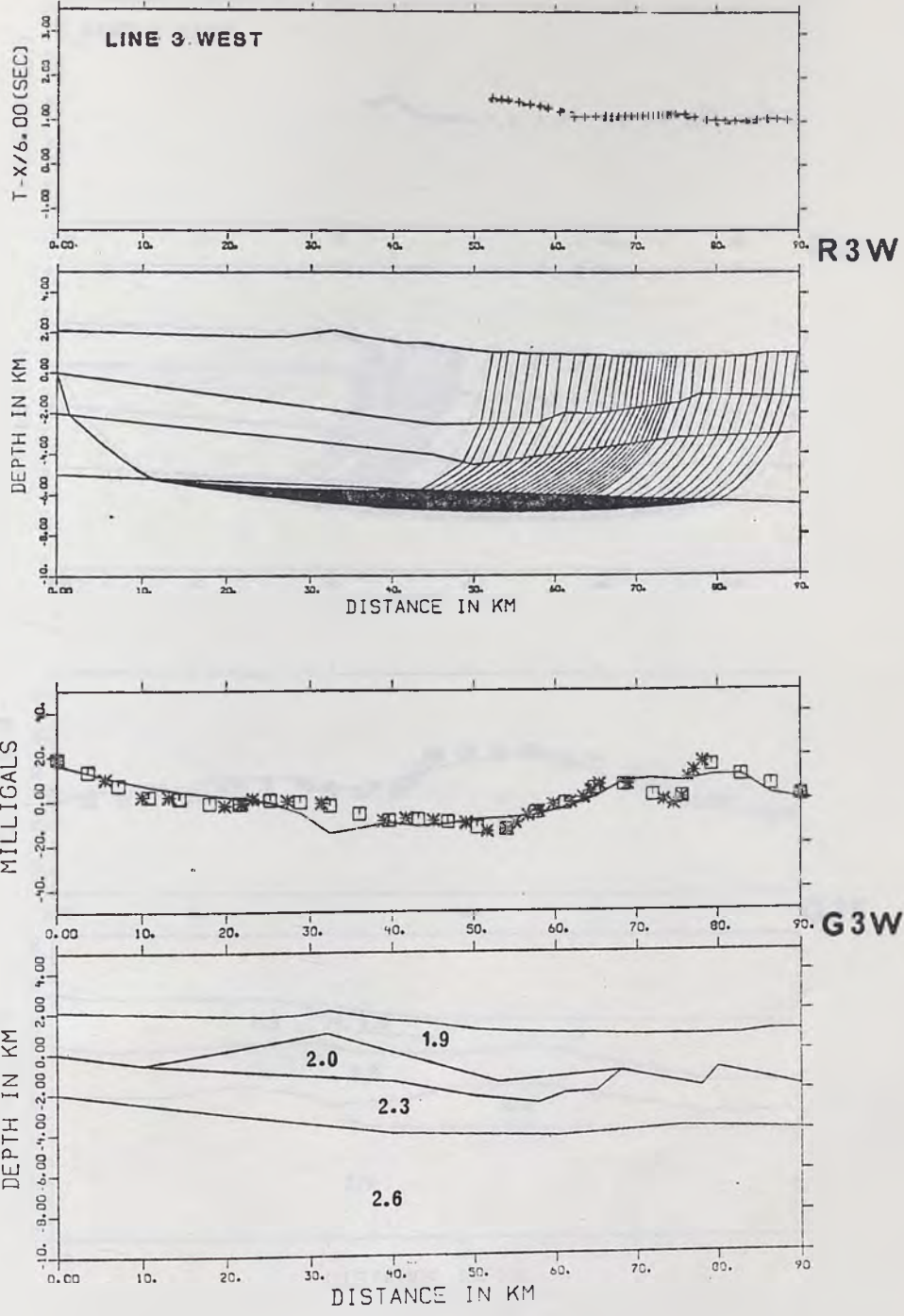


FIGURE 12-C

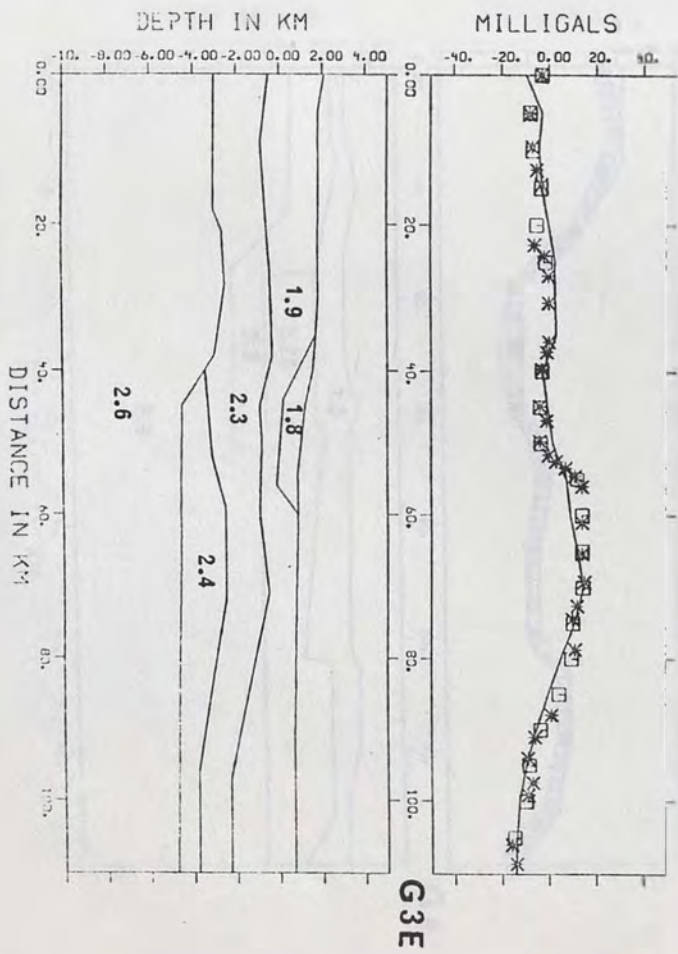
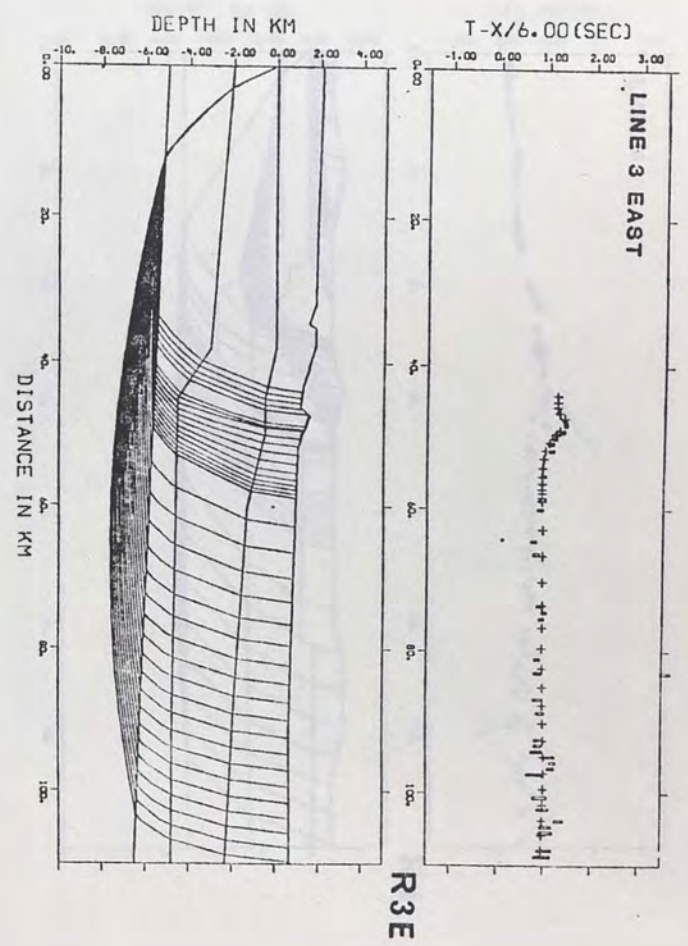


FIGURE 12-D



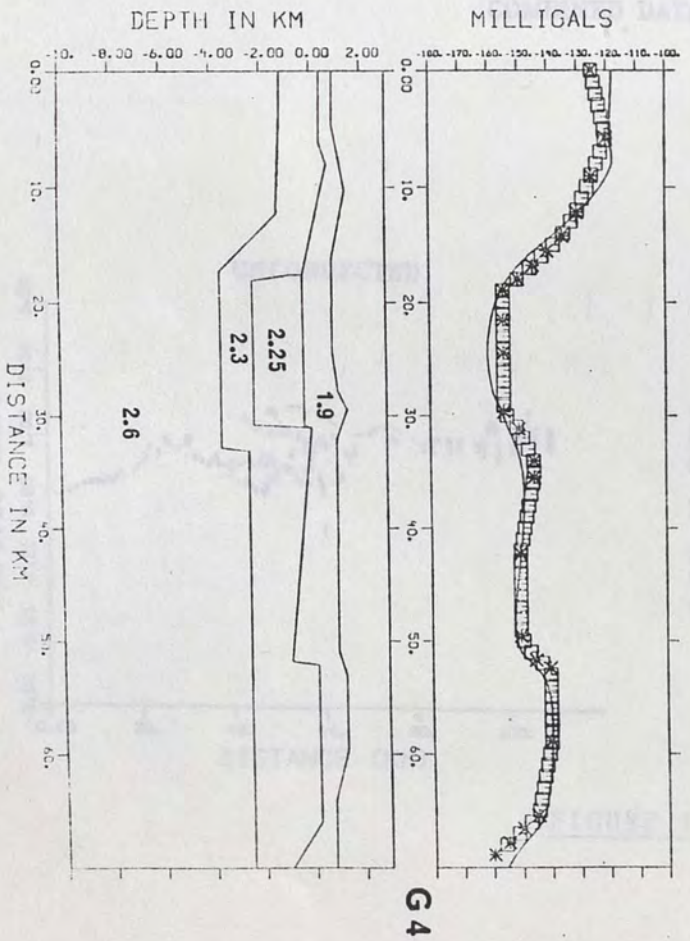
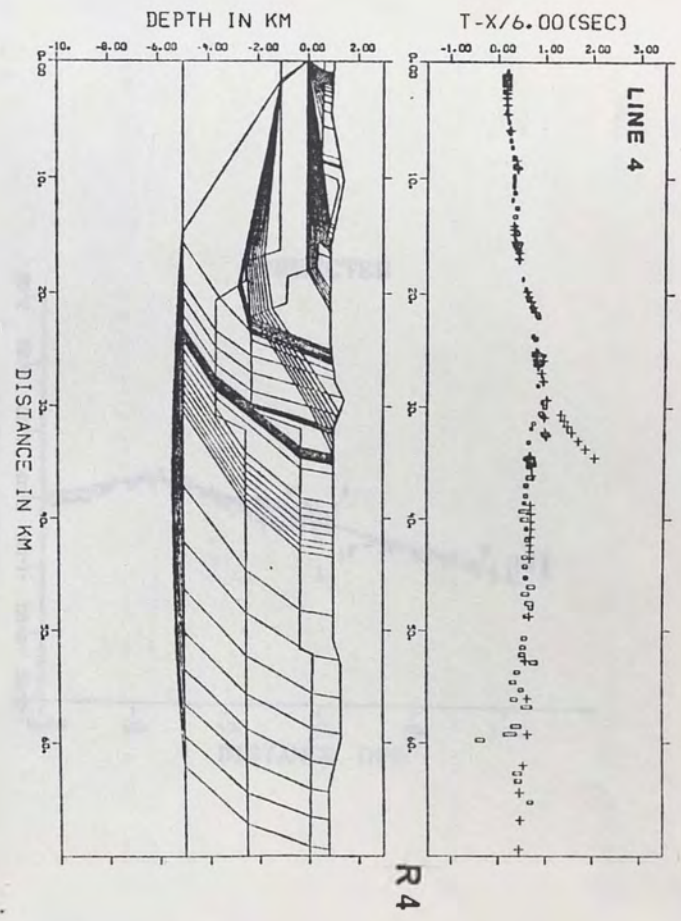


FIGURE 12-E



COMBINED DATA

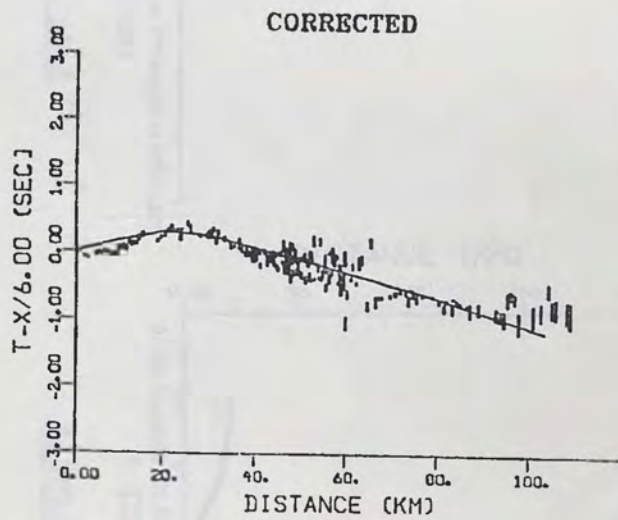
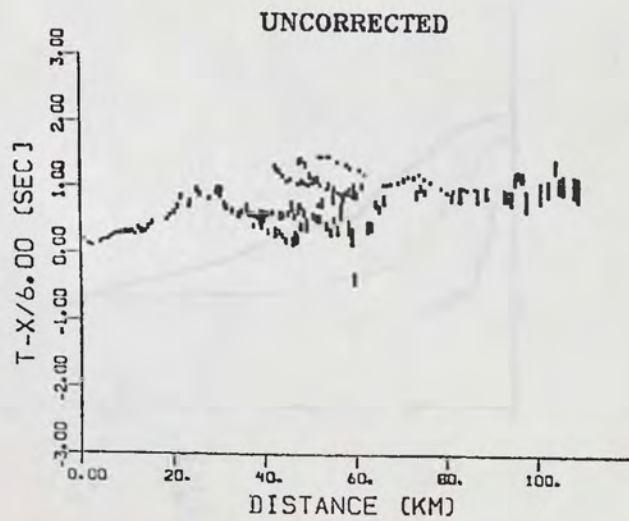


FIGURE 13

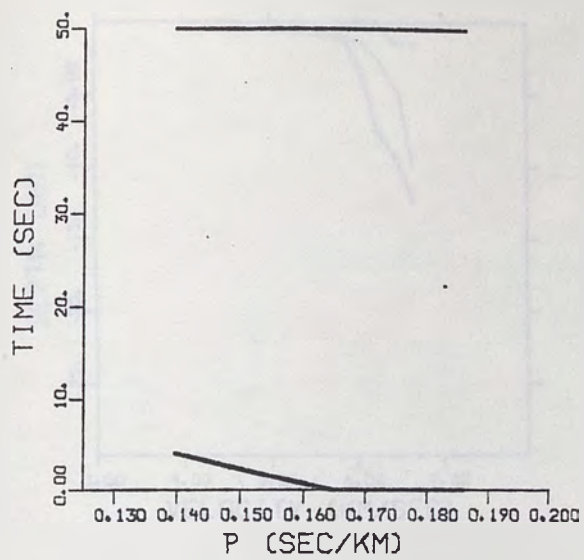


FIGURE 14-B

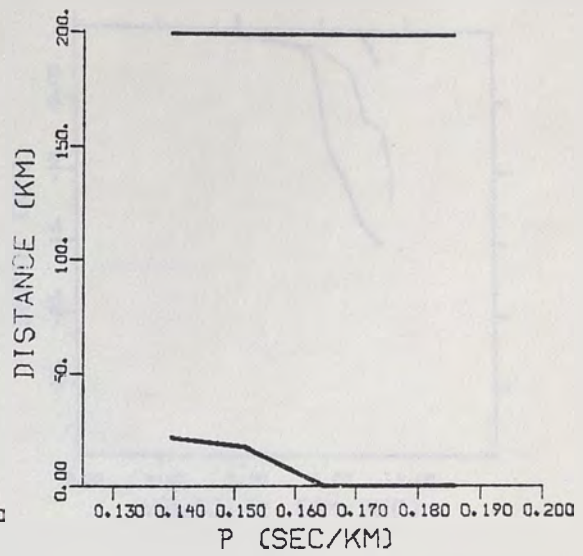


FIGURE 14-C

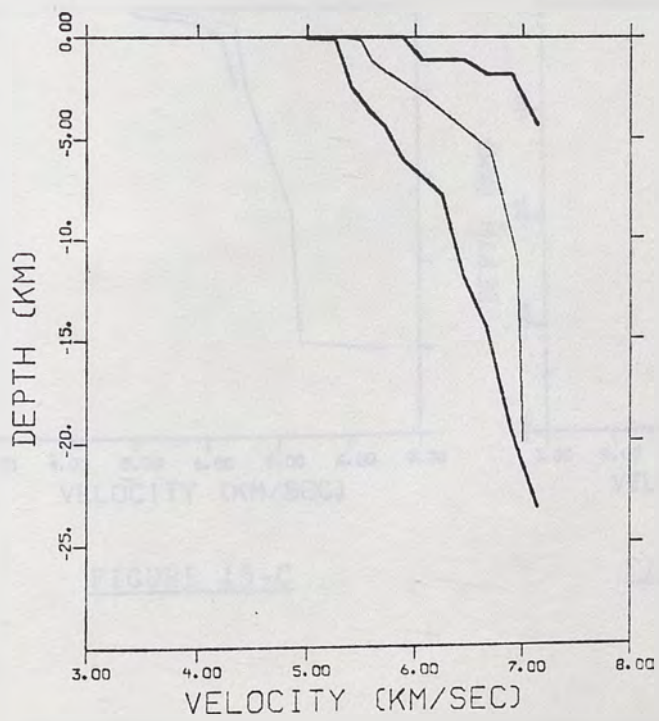


FIGURE 14-A



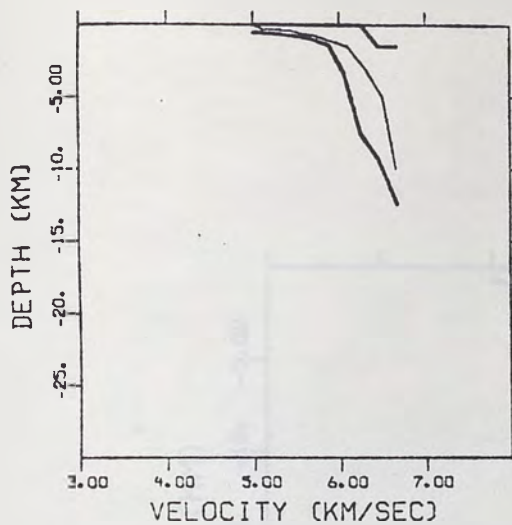


FIGURE 15-A

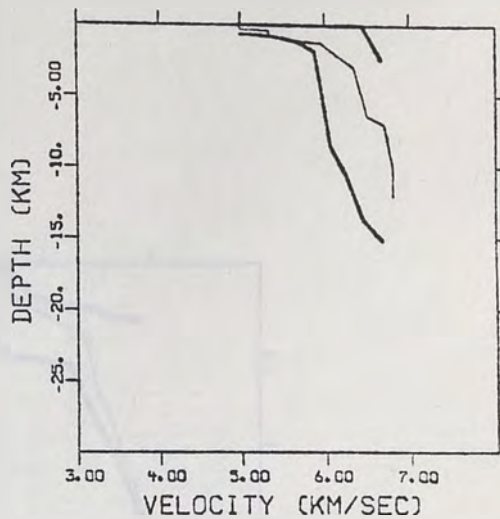


FIGURE 15-B

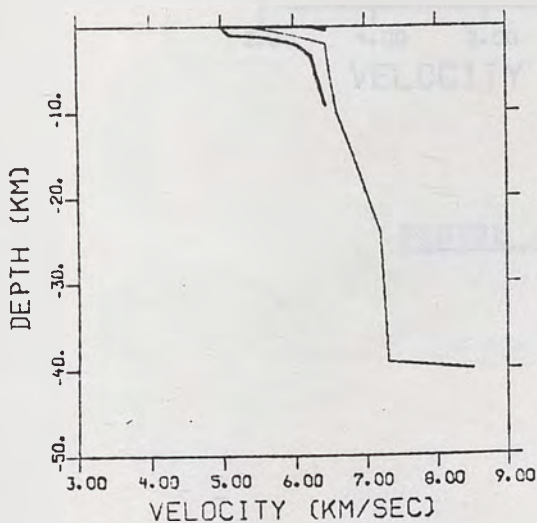


FIGURE 15-C

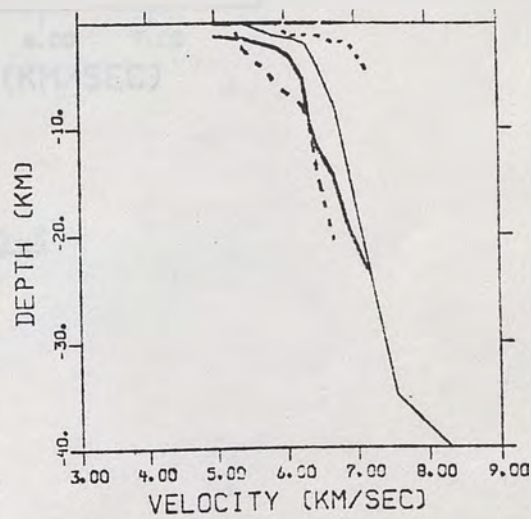


FIGURE 15-D

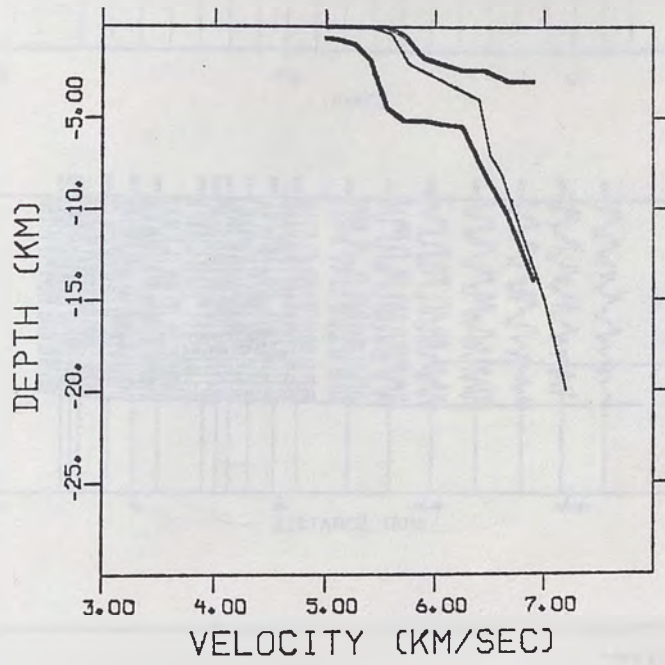


FIGURE 15-E

FIGURE 15-A





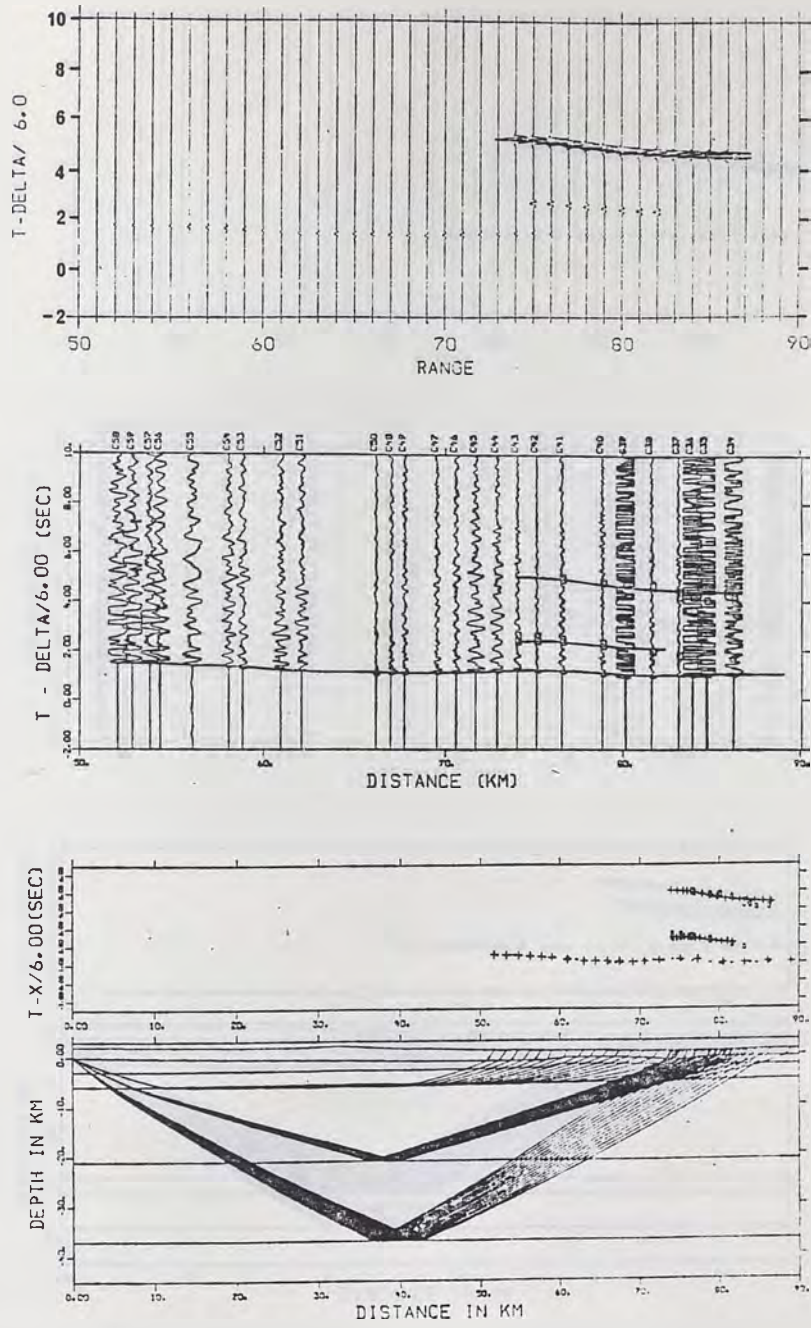


FIGURE 16-C



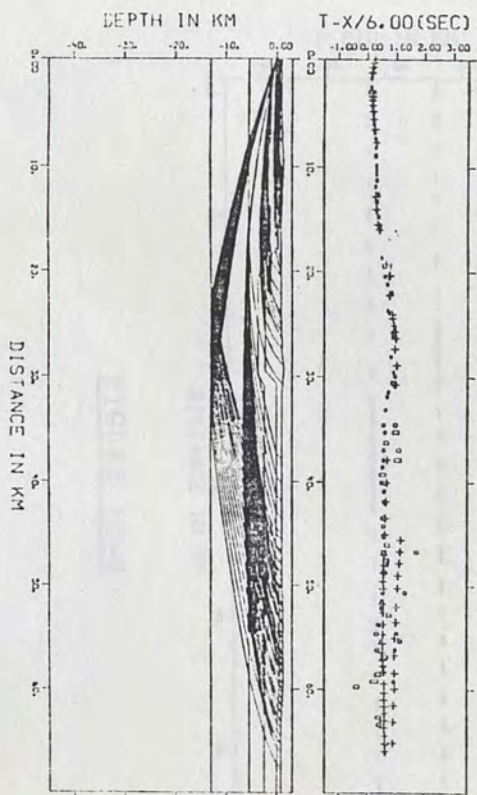
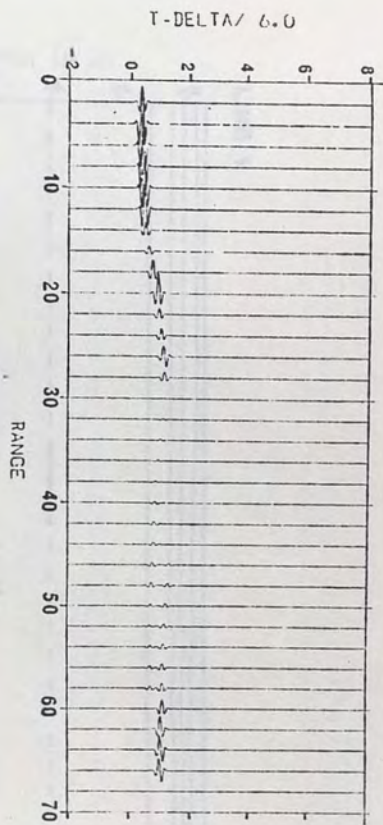
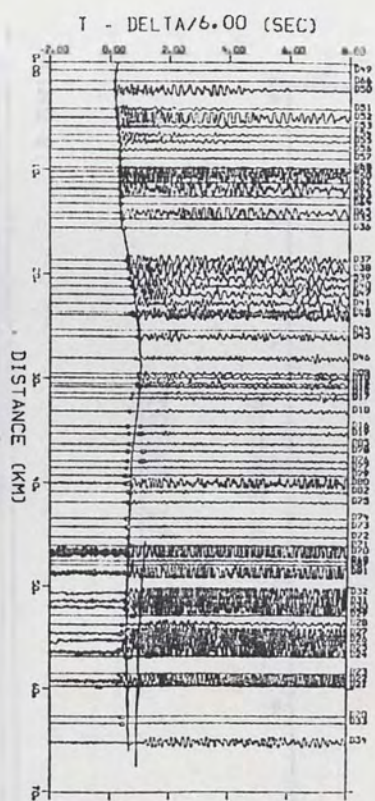


FIGURE 16-E



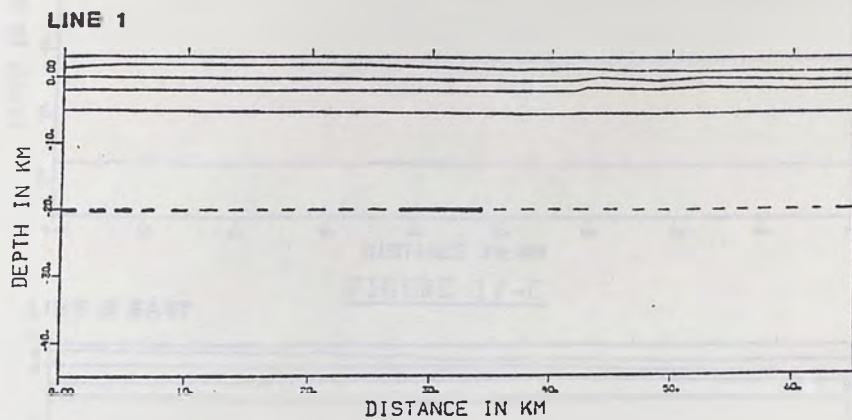


FIGURE 17-A

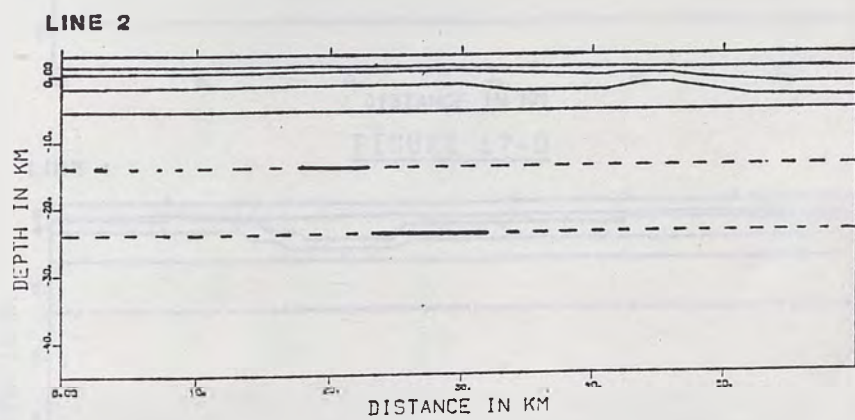


FIGURE 17-B



LINE 3 WEST

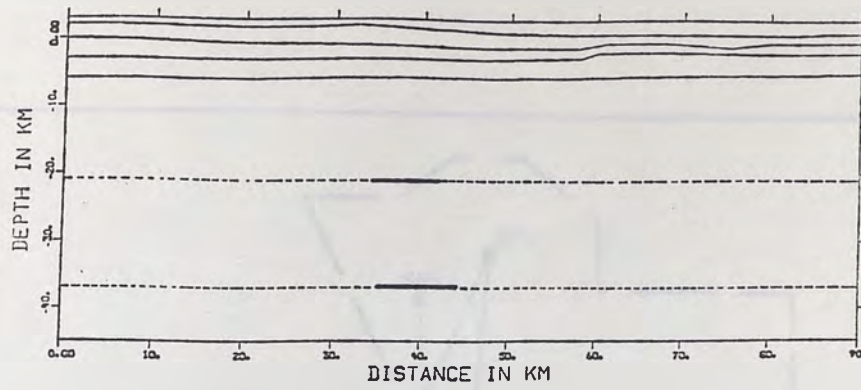


FIGURE 17-C

LINE 3 EAST

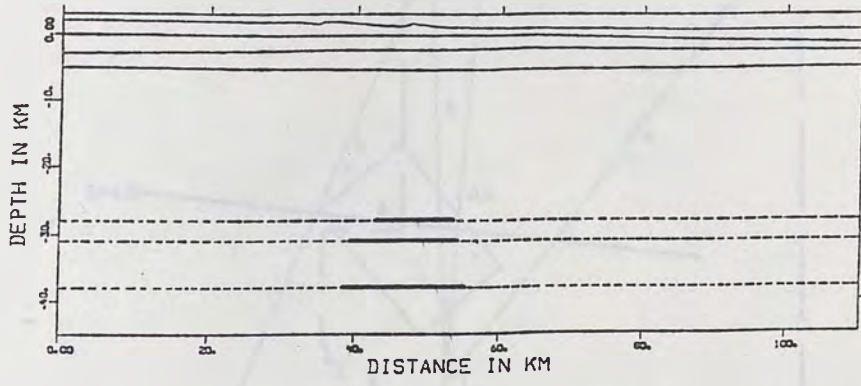


FIGURE 17-D

LINE 4

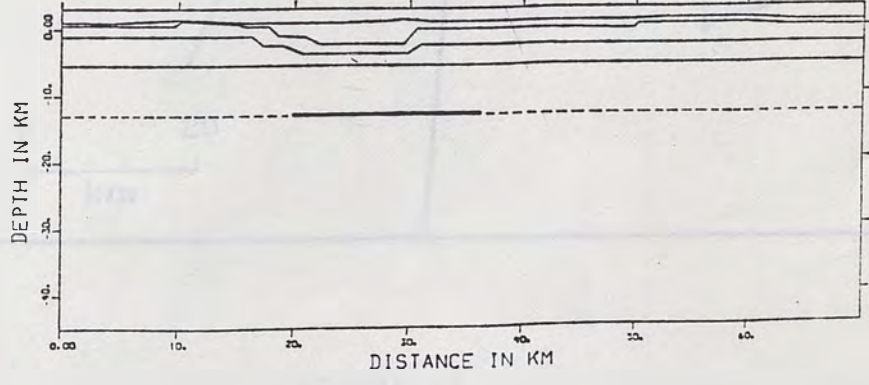


FIGURE 17-E

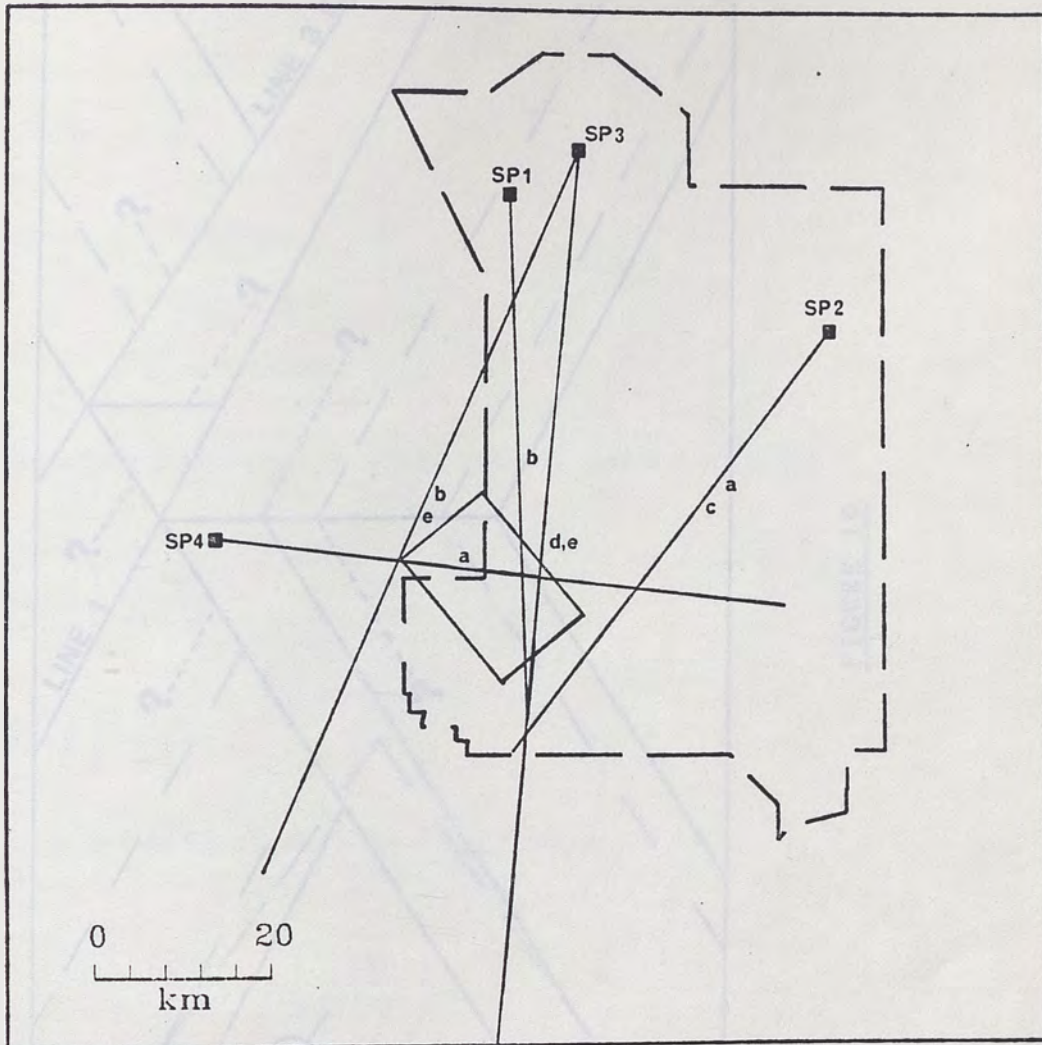


FIGURE 18

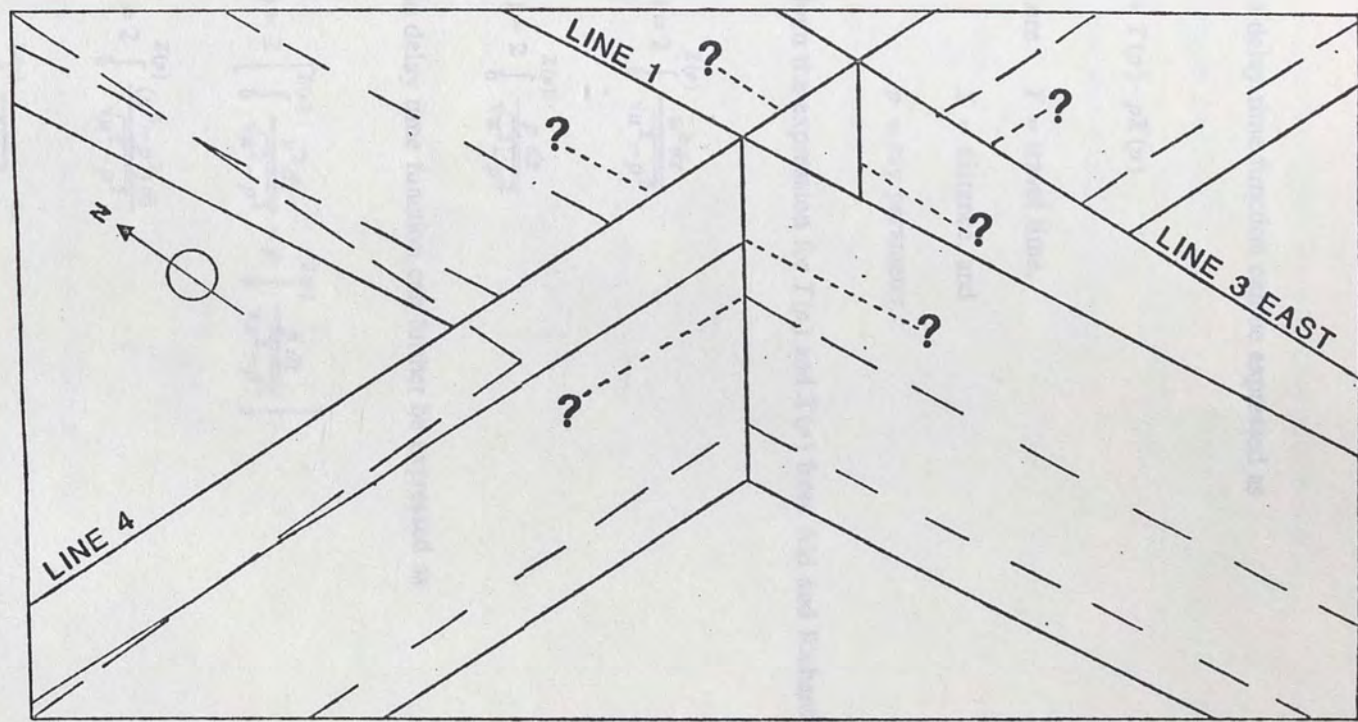


FIGURE 19

## APPENDIX A

The delay time function can be expressed as

$$\tau(p) = T(p) - pX(p)$$

where  $T$  = travel time,

$X$  = distance, and

$p$  = ray parameter.

Given the expression for  $T(p)$  and  $X(p)$  from Aki and Richards (1980) as

$$T(p) = 2 \int_0^{Z(p)} \frac{u^2 dz}{\sqrt{u^2 - p^2}}$$

$$X(p) = 2 \int_0^{Z(p)} \frac{p dz}{\sqrt{u^2 - p^2}}$$

the delay time function can further be expressed as

$$\begin{aligned} \tau(p) &= 2 \left[ \int_0^{Z(p)} \frac{u^2 dz}{\sqrt{u^2 - p^2}} - p \int_0^{Z(p)} \frac{p dz}{\sqrt{u^2 - p^2}} \right] \\ &= 2 \int_0^{Z(p)} \frac{(u^2 - p^2) dz}{\sqrt{u^2 - p^2}} \\ &= 2 \int_0^{Z(p)} \sqrt{u^2 - p^2} dz \end{aligned} \tag{A.1}$$

The inversion of  $\tau(p)$  in terms of linear programming to obtain  $Z(u)$  requires that a linearity exists between  $\tau(p)$  and  $Z(u)$ .

To obtain the linearity, the  $\tau(p)$  of (A.1) can be simplified by

(i) changing the variable of integration to  $u$ , i.e.  $u(z)$ .

Define at  $z = 0, u(0) = u_0$

and at  $z = z(p), u(z(p)) = p$

with  $dz = du \left( \frac{dz}{du} \right)$

This implies that

$$\tau(p) = 2 \int_{u_0}^p \sqrt{u^2 - p^2} \left( \frac{dz}{du} \right) du \quad (\text{A.2})$$

where  $u_0$  = surface slowness, and

$p$  = horizontal slowness

(ii) Integration by parts, recall:

$$\left[ \int x dy = xy - \int y dx \right] \text{ then,}$$

$$\tau(p) = \left[ \sqrt{u^2 - p^2} Z(u) \right]_{u_0}^p - 2 \int_{u_0}^p \frac{Z(u) u du}{\sqrt{u^2 - p^2}}$$

and reversing the limits of integration to get

$$\tau(p) = 2 \int_p^{u_0} \frac{Z(u) u du}{\sqrt{u^2 - p^2}} \quad (\text{A.3})$$

Define a new variable  $\eta = \sqrt{u^2 - p^2}$  (vertical slowness)

$$d\eta = \frac{u \, du}{\sqrt{u^2 - p^2}}$$

$$\eta \, d\eta = u \, du$$

Substitute the new variable into [A.3] to get

$$\begin{aligned} \tau(p) &= 2 \int_p^{u_0} \frac{Z(u) \eta \, d\eta}{\eta} \\ &= 2 \int_p^{u_0} Z(\eta^2 + p^2) \, d\eta \end{aligned}$$

Now, consider the approach used by Dorman (1979), where  $Z(u)$  is constructed by integration of  $\frac{dz}{du}$ .

$$Z(u) = \int_{u_0}^u \left( \frac{dz}{du} \right) du$$

Define  $\frac{dz}{du} = \sum_i w_i f_i(u)$  (Orcutt, 1980), where

$w_i$  = layers of constant slowness  $\frac{dz}{du}$  between  $u_{i-1}$  and  $u_i$ , and

$$f_i(u) = \begin{cases} 1 & u_i < u < u_{i-1} \\ 0 & \text{elsewhere} \end{cases}$$

Thus, from [A.2]

$$\tau(p) = 2 \int_{u_0}^p \sqrt{u^2 - p^2} \left( \frac{dz}{du} \right) du$$

substitute  $\frac{dz}{du}$  into the above expression.

$$\tau(p) = 2 \int_{u_0}^p \sqrt{u^2 - p^2} \sum_i w_i f_i(u) \, du$$

$$= \sum_i w_i 2 \int_{u_0}^p \sqrt{u^2 - p^2} f_i(u) du$$

$$= \sum_i w_i h_i(p)$$

where  $h_i(p) = 2 \int_{u_{i-1}}^{\max(u_i, p)} \sqrt{u^2 - p^2} du$

Using integration tables, and define  $u_{\max} = \max(u_i, p)$  by Orcutt (1980).

$$h_i(p) = u_{\max} \sqrt{u_{\max}^2 - p^2} - u_{i-1} \sqrt{u_{i-1}^2 - p^2} - p^2 \ln \left[ \frac{u_{\max} + \sqrt{u_{\max}^2 - p^2}}{u_{i-1} + \sqrt{u_{i-1}^2 - p^2}} \right]$$

Following similar procedure for  $X(p)$ , by changing variable of integration,

$$X(p) = 2 \int_0^{z(p)} \frac{p dz}{\sqrt{u^2 - p^2}}$$

Let  $u = u(z)$ ; then  $dz = du \left( \frac{dz}{du} \right)$

$$X(p) = 2p \int_{u_0}^{z(p)} \frac{du}{\sqrt{u^2 - p^2}} \left( \frac{dz}{du} \right)$$

substitute  $\frac{dz}{du} = \sum_i w_i f_i(u)$

$$X(p) = 2p \int_{u_0}^{z(p)} \frac{du}{\sqrt{u^2 - p^2}} \sum_i w_i f_i(u)$$

$$= \sum_i w_i 2p \int_{u_0}^p \frac{du}{\sqrt{u^2 - p^2}} f_i(u)$$

$$= \sum_i w_i g_i(p)$$

where 
$$g_i(p) = 2p \int_{u_{i-1}}^{u_{\max}} \frac{du}{\sqrt{u^2 - p^2}}$$

From integration tables:

$$g_i(p) = 2p \ln \left[ \frac{u_{\max} + \sqrt{u_{\max}^2 - p^2}}{u_{i-1} + \sqrt{u_{i-1}^2 - p^2}} \right]$$

Thus, a matrix relationship between the data and model is expressed as:

$$D = A \Omega$$

where:

$D$  = data matrix

$$= (\tau(p_1), x(p_1), \tau(p_2), x(p_2), \dots, \tau(p_n), x(p_n))^T$$

$$\Omega = (w_1, w_2, w_3, w_4, \dots, w_m)^T, \text{ and}$$

$$A = \begin{bmatrix} h_1(p_1), \dots, h_m(p_1) \\ g_1(p_1), \dots, g_m(p_1) \\ \dots \\ \dots \\ h_1(p_n), \dots, h_m(p_n) \\ g_1(p_n), \dots, g_m(p_n) \end{bmatrix}$$

where  $n$  = number of  $\tau(p)$  points, and

$m$  = number of layers of constant slowness,  $(\frac{dz}{du})$ .

The depth  $d$  to some slowness as defined by (Orcutt, 1980; MacKenzie *et al.*, 1982) is

thus:



$$d = \sum_1^i (u_i - u_{i-1}) w_i = \Delta u \cdot \Omega$$

Using linear programming the maximum and minimum depth to a given slowness can be computed by changing the sign of  $u$  (Orcutt, 1980).

## APPENDIX B

In this appendix the validity of the delay time inversion method is tested. Three models are constructed for this purpose.

M1, the first model consists of 3 layers over a half-space (Fig. B-1). The second model, M2, is made up of 3 layers with a dip of 4 degrees in the second boundary (Fig. B-2). The third model, M3, has lateral heterogeneities in layer 1 and 2. Each model has positive velocity gradients in each layer. The travel time data for the three models are calculated using two-dimensional ray-tracing. The travel time curve is then digitized at 2 km spacing. M2 and M3 have two sets of travel time data for each end of the profile. The spread for M3 extends to 100 km distance and for both M2 and M3 to 200 km distance.

The data sets consist of digitized travel time data as shown in Figures B-4, B-5 and B-6. Only first arrivals are used since they are easily identified in real data. Time errors and distance errors are assigned to the travel time data sets in order to simulate errors found in the real data. Time errors increase from 0.05 seconds at close ranges to 0.15 seconds at further distances. Distance errors of 0.1524 km correspond to distance errors found in the real data used in this study.

The travel time data are then reparameterized in terms of  $\tau(p)$  functions (the  $\tau(p)$  envelope picked are shown in Fig. B-7; I, II and III). The  $\tau(p)$  envelopes in Figure B-7; (I) and (II) indicate no gaps in  $\tau$  and  $p$ . This means there is no evidence of a low velocity zone (Bessonova *et. al.*, 1974; Kenneth *et. al.*, 1976). The  $\tau(p)$  envelopes of Figure B-7 (III) differs from the previous  $\tau(p)$  envelopes (Figs. B-7 and B-8) in the existence of gaps in both  $\tau$  and  $p$ . According to Bessonova *et. al.* (1974), gaps in  $\tau$  and  $p$  cannot prove the absence of low velocity zone.

The  $\tau(p)$  functions defined in terms of picked points in Figure B-7 (I, II and III) for the three models are inverted to determine the velocity-depth functions separately. Time-distance constraints are used in all three inversions. These constraints together with the  $\tau(p)$  points form the input parameters for the inversion program. Time-distance constraints are given as pairs of time limits and distance limits for an observed travel time branch, determined from the travel time curves (Figs. B-4, B-5 and B-6). The time and distance constraints are shown graphically for the three models (M1, M2 and M3) in Figure B-8. In addition to the time-distance constraints, cross-over constraint is used in the inversion of M1. This constraint forces the first two travel time branches of M1 (Fig. B-4) to intersect at distances between 10 km and 5 km, with travel times between 3.1 seconds and 4.6 seconds.

The resulting velocity-depth bounds for M1, M2, and M3 are illustrated in Figure B-9 (I, II, and III). The extremal velocity bounds for M1 show a tight constraint at shallow depths (effect of cross-over constraint) and wider bounds at greater depths. The calculated velocity-depth function for M1 lies within the extremal bounds indicating the validity of this method (Fig. B-9 (I)) for flat lying models. In Figure B-9 (II), the extremal bounds are wider with occurrence of velocity steps in the upper bounds. Since the extremal bounds are derived from a dipping layer model (M2), the bounds contained both the extreme velocity-depth functions for downdip and updip; and thus explained the occurrence of the wider bounds. Extremal bounds are shown in Figure B-9 (III), this is the extreme case among the three inversions. In this case, the assumption of flat lying structures implicit in the  $\tau(p)$  method is not justified when deriving the velocity bounds. The bounds are wide and poorly constrained at deeper depths.

To evaluate the consistency of the tau-p method, average velocity-depth functions as a function of velocity are derived from the three extremal bounds. These average velocity-depth functions are determined by taking the average depth for velocities from the upper and lower bounds. These derived functions are illustrated in Figure B-10 (I, II, and III) as bold lines. The velocity-depth functions ( $V_a(z)$ ) from the models (M1, M2, and M3) are also drawn in to determine the accuracy of the method.

In Figure B-10 (I), the actual velocity depth function and the average velocity depth function ( $V_{avg}(z)$ ) are in excellent agreement. For depths below 20 km, the  $V_a(z)$  has velocity steps. However, the  $V_{avg}(z)$  does not show this. The average  $V_{avg}(z)$  tends to smooth out the velocity steps, resulting in a smooth velocity gradient.

Comparison for M2 show less correlation (Fig. B-10,(II)), although the upper 5 km structures are in good agreement. The average  $V_{avg}(z)$  is closely related to the actual  $V_a(z)$  at down dip. This discrepancy can be explained by the error in picking the lower bound of the tau-p envelope in Figure B-7 (II). The error involved here will affect the upper limit of the velocity-depth bounds of Figure B-9 (II). But in general, the average  $V_{avg}(z)$  shows good correlation in terms of velocity gradient.

The average  $V_{avg}(z)$  in comparison to the actual  $V_a(z)$  of M3 shows inconsistency for the actual  $V_a(z)$  derived at 100 km distance (Fig. B-10, III). However, when compared to the actual  $V_a(z)$  derived at 0 km distance, both models show good correlation for velocity structures above 12 km. Below this depth ( $> 12$  km) similarity occurs in terms of velocity gradients for these two models. The explanation for the inconsistencies in Figure B-10, (II) is applicable here.

To summarize, this appendix verifies the validity of the software used and the  $\tau(p)$  method for interpretation of flat lying structures. For velocity structures that have small lateral variations as in M2, care must be taken in interpreting the results, since only apparent  $V(z)$  can be derived due to the violation of the assumption of flat lying structures. For structures that have strong lateral variations (M3), it is recommended that these variations be removed before making attempts to interpret the  $\tau(p)$  results.

## LIST OF FIGURES (APPENDIX B)

Figure B-1. Flat lying velocity model (M1) extending to 100 km. The numbers within the model indicate velocity specifications of each layer in units of km/sec.

Figure B-2. Dipping-layer velocity model (M2), with a dip of 4 degrees in interface 3 (interface 1 is defined at the surface,  $z=0$  km). The velocity specification is the same as in M1, but with the existence of a dip in interface 3, velocity gradient in layer 2 increases as range increases. The opposite is true in layer 3.

Figure B-3. Velocity model (M3) with depths of 35 km. Model indicate lateral heterogeneities in layer 1 and 2. In real data this layer discontinuity may be caused by existence of faults. Velocity specifications in each layer is in km/sec.

Figure B-4. Unreversed digitized travel-time data with their associated errors in brackets for M1 (first arrivals at 2 km spacing).

Figure B-5. Digitized travel-time data with their associated errors in brackets for up and downdip calculations for M2 (first arrivals at 2 km spacing).

Figure B-6. Digitized travel-time data with source at 0 and 100 km with their associated errors in brackets for M3. The travel-time data is at 2 km spacing.

Figure B-7. The tau-p envelope determined from the reparameterized data sets. The circles indicate picks that are used to determined the envelope.

(I). tau-p envelope for M1,

(II) tau-p envelope for M2, and

(III) tau-p envelope for M3.

Figure B-8. Time ( $T(p)$ ) and distance ( $X(p)$ ) curves used in the inversion routines for M1, M2, and M3.

Figure B-9. Extremal velocity-depth bounds (bold lines) with the velocity-depth functions of the velocity models constructed from Figures B-1,2,3 drawn in for comparison.

(I) Velocity-depth bounds for M1,

(II) Velocity-depth bounds for M2. The velocity-depth function for the dipping model is calculated at downdip and updip (dashed lines).

(III) Velocity-depth bounds for M3. The velocity-depth function for M3 is calculated at each end of the model (Figure B-3) with velocity-depth function calculated at 100 km, drawn in as dashed lines.

Figure B-10. Comparison between the average velocity-depth functions derived from the extremal bounds (bold lines) and the actual velocity-depth functions from the models, defined in the same manner as in Figure B-9.

(I) Comparison for M1,

(II) Comparison for M2, and

(III) Comparison for M3.

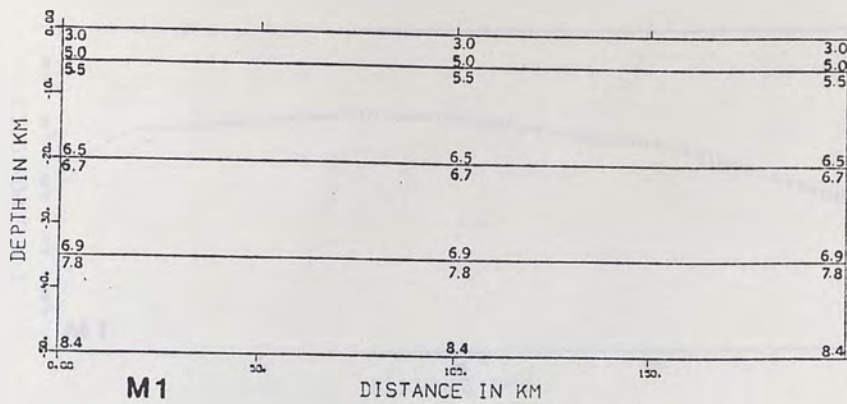


FIGURE B-1

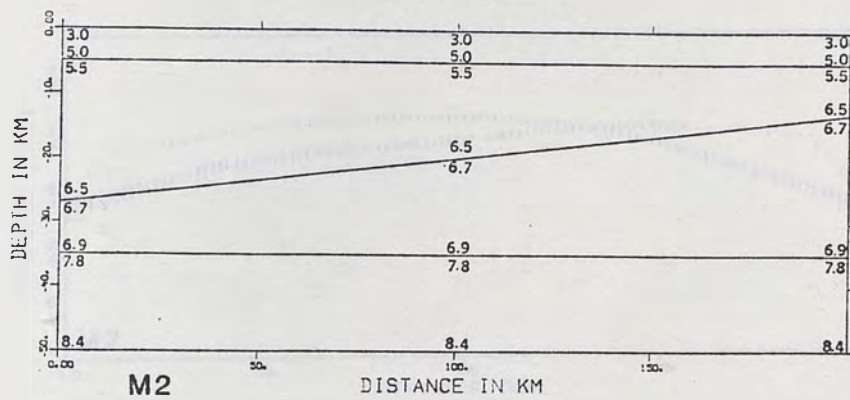


FIGURE B-2

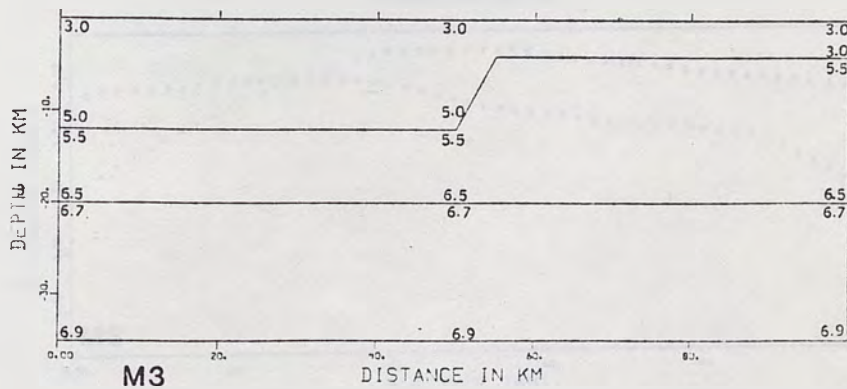


FIGURE B-3

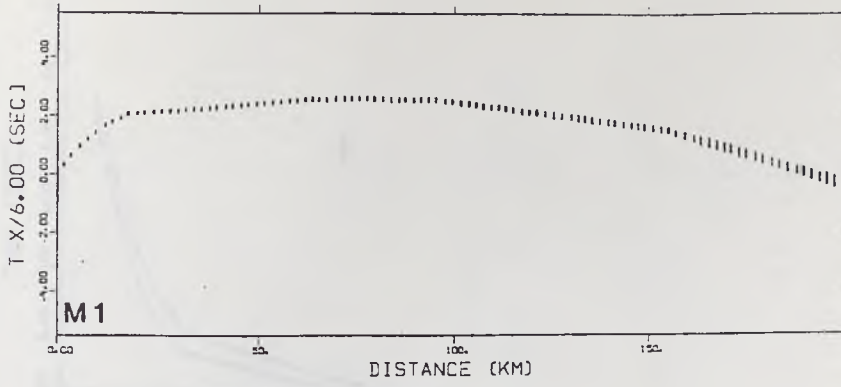


FIGURE B-4

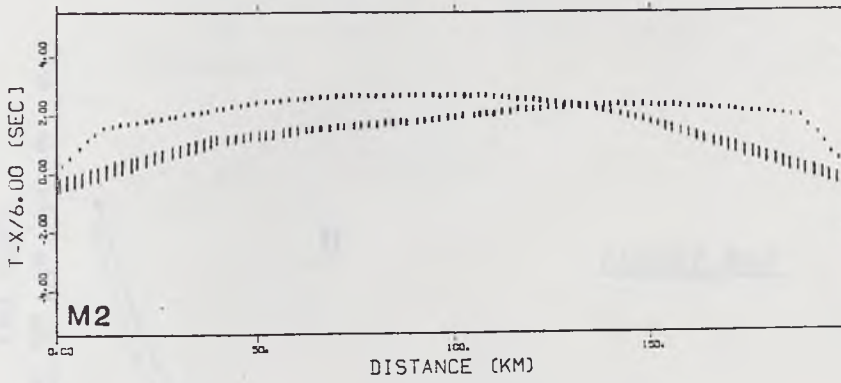


FIGURE B-5

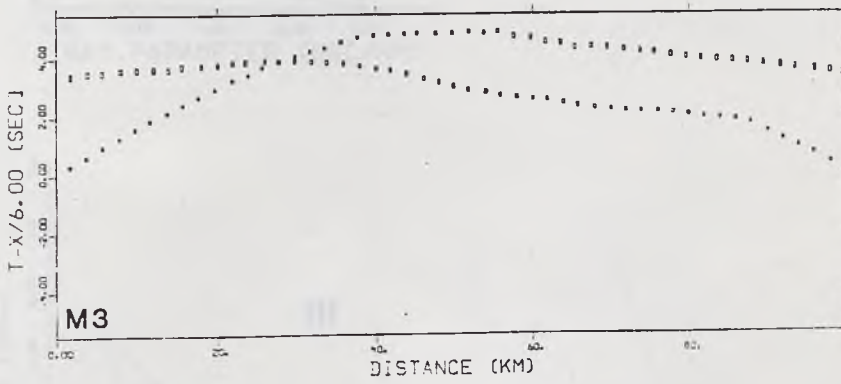


FIGURE B-6

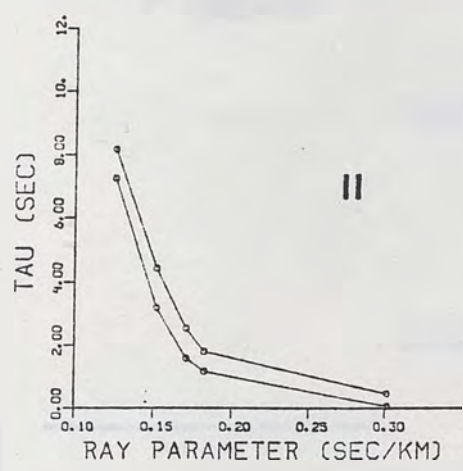
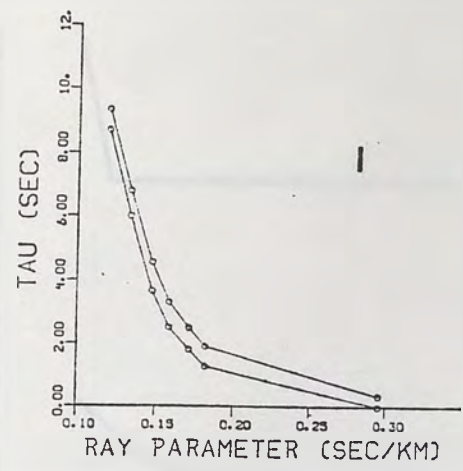
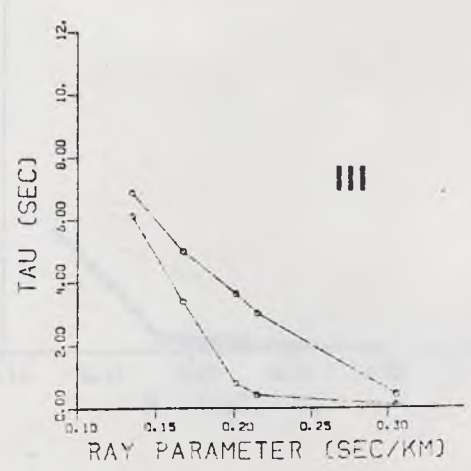


FIGURE B-7





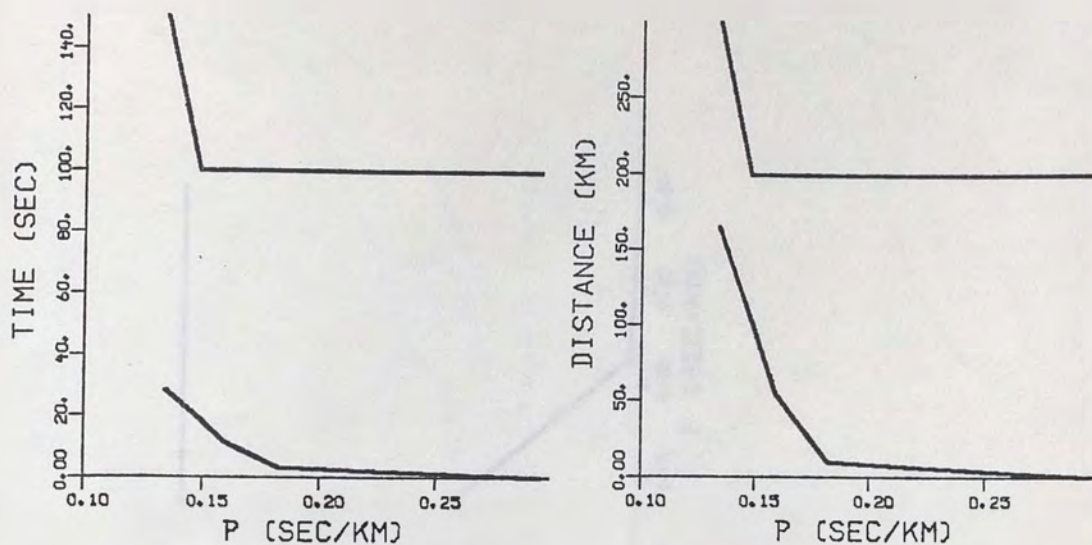
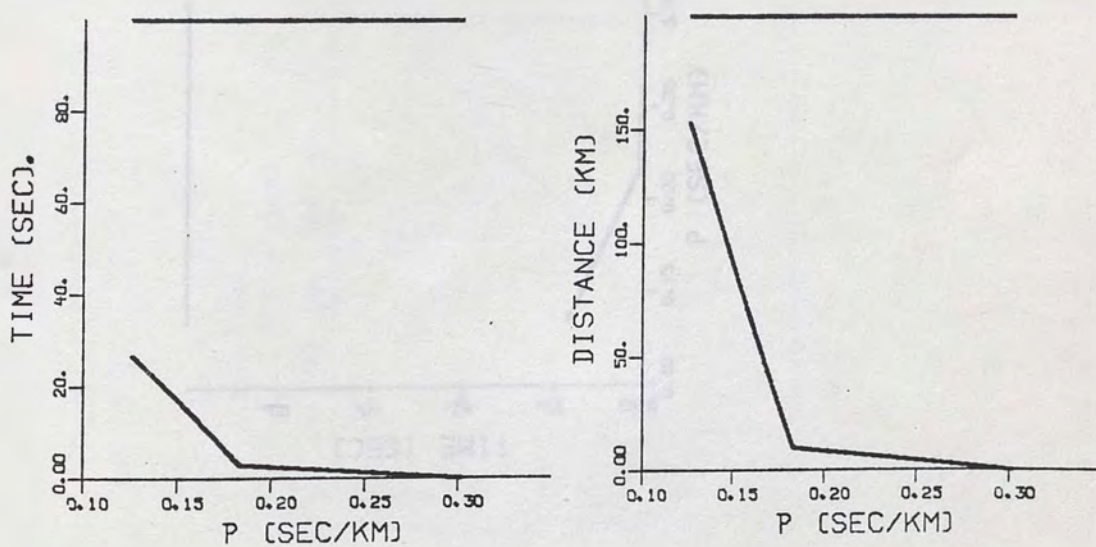


FIGURE B-8 (M1)

FIGURE B-8 (M2)



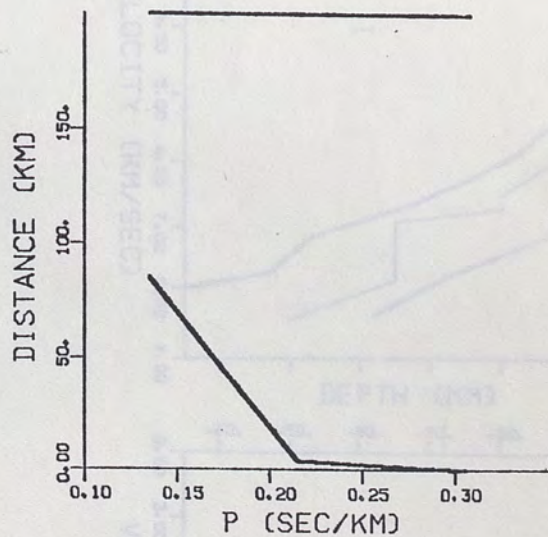
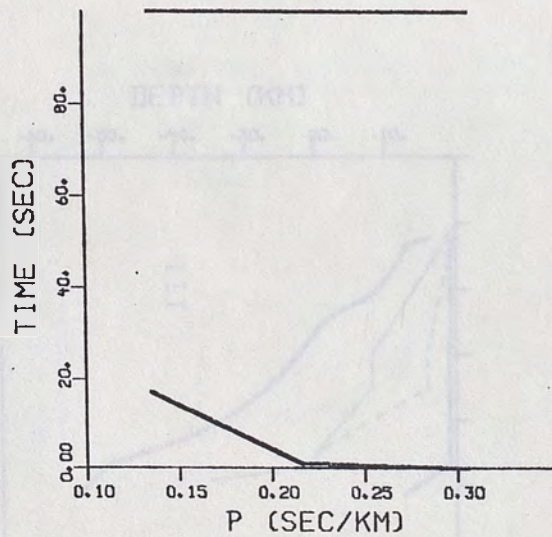


FIGURE B-8 (M3)

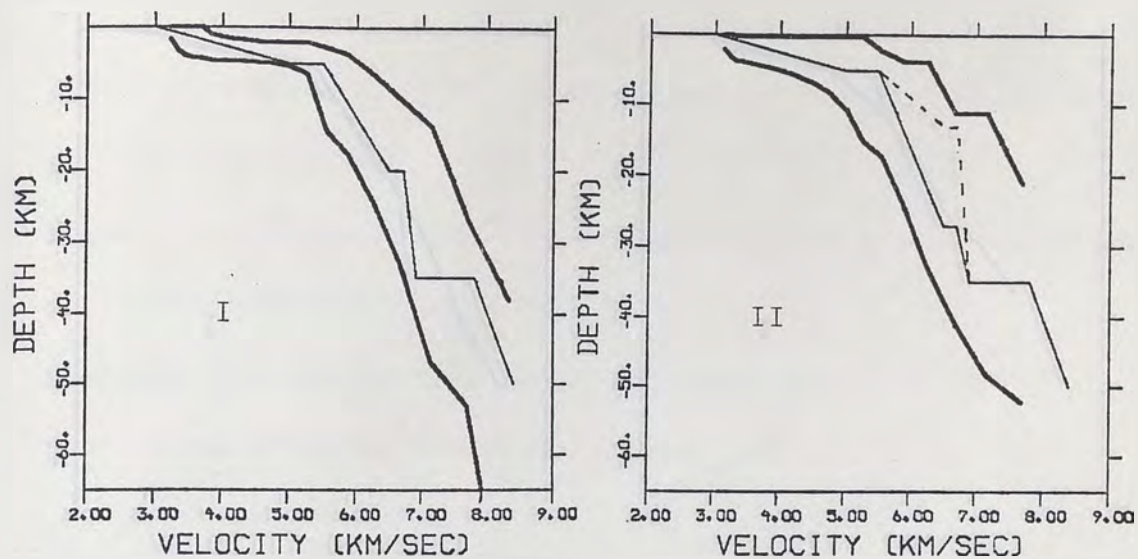
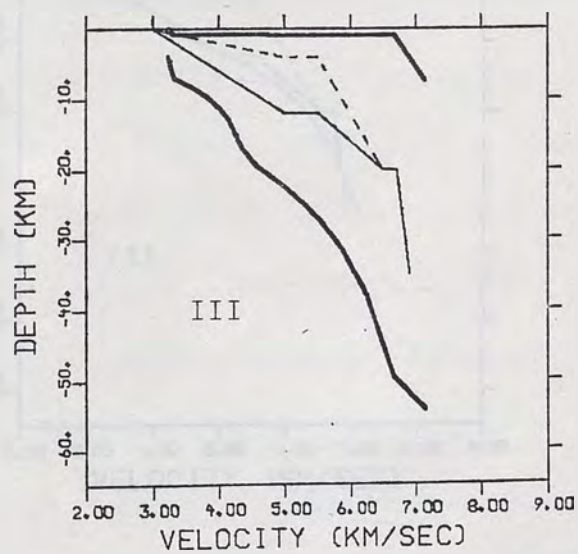


FIGURE B-9



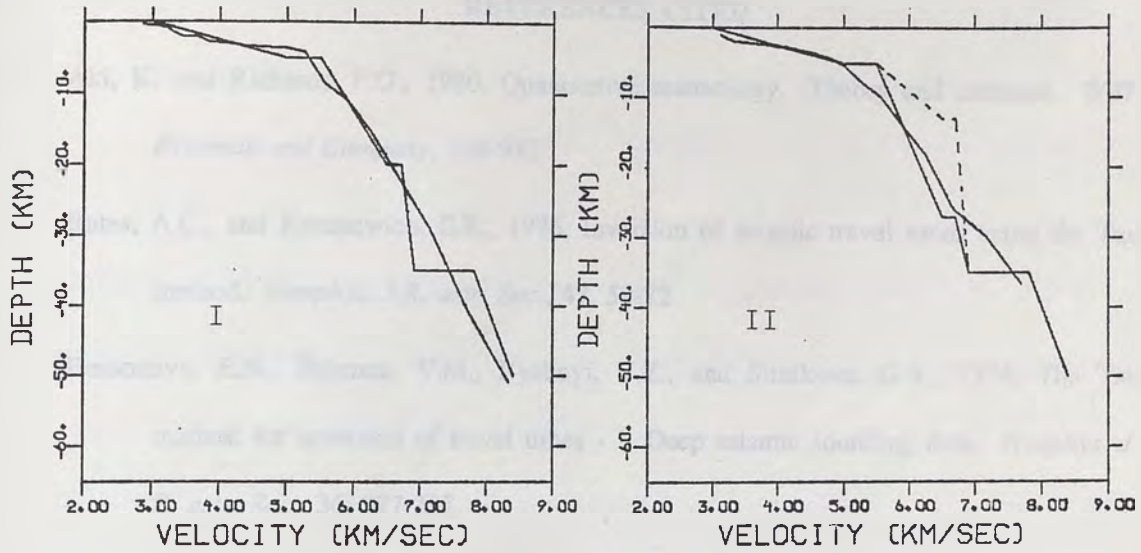
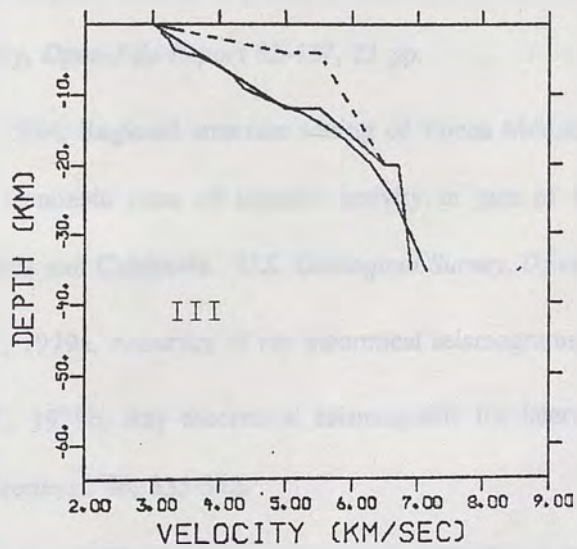


FIGURE B-10



## REFERENCES CITED

- Aki, K. and Richards, P.G., 1980, Quantitative seismology. Theory and methods. *W.H. Freeman and Company*, 559-932
- Bates, A.C., and Kanasewich, E.R., 1976, Inversion of seismic travel times using the Tau method. *Geophys. J.R. astr. Soc.*, **47**, 59-72
- Bessonova, E.N., Fishman, V.M., Ryaboyi, V.Z., and Sitnikova, G.A., 1974, The Tau method for inversion of travel times - I. Deep seismic sounding data. *Geophys. J. R. astr. Soc.*, **36**, 377-398
- Boynton, G.R., and Vargo, J.L., 1963, Aeromagnetic map of the Topopah Spring quadrangle and part of the Bare Mountain quadrangle Nye County, Nevada. *U.S. Geological Survey, Geophysical Investigation MAP GP-440*.
- Carr, W.J., 1982, Volcano-tectonic history of Crater Flat, southwestern Nevada, as suggested by new evidence from drill hole USW-VH-1 and vicinity. *U.S. Geological Survey, Open-File Report 82-457*, 23 pp.
- Carr, W.J., 1984, Regional structure setting of Yucca Mountain, southwestern Nevada, and late Cenozoic rates of tectonic activity in part of the southwestern Great Basin, Nevada and California. *U.S. Geological Survey, Open-File Report 84-854*, 109 pp.
- Cervený, V., 1979a, Accuracy of ray theoretical seismograms. *J. Geophys.*, **46**, 135-149.
- Cervený, V., 1979b, Ray theoretical seismograms for laterally inhomogeneous structures. *J. Geophys.*, **46**, 335-342.
- Cornwall, H.R., 1967, Geology and mineral deposits of southern Nye County, Nevada. *Nevada Bureau of Mines and Geology, Bull. 77.*, 49 pp

- Eaton, G.P., Wahl, R.R., Prostka, H.J., Mabey, D.R., Kleinkopf, M.D., 1978, Regional gravity and tectonic patterns: Their relation to late Cenozoic epeirogenic and lateral spreading in the western Cordillera. *Geological Society of America Memoir 152*, 51-91.
- Garmany, J., 1979, On the inversion of travel times. *Geophys. Res. Lett.*, **6**, 277-279.
- Garmany, J., Orcutt, J.A., and Parker, R.L., 1979, Travel-time inversion: a geometrical approach. *J. Geophys. Res.* **84**, 3615-3622.
- Healey, D.L., Miller, C.H., 1962, Gravity survey of the Nevada Test Site and vicinity, Nye, Lincoln, and Clark counties, Nevada. *U.S. Geological Survey TEI-827, Open-File Report*, 36 pp.
- Healey, D.L., Wahl, R.R., and Currey, F.E., 1980, Complete Bouguer gravity map of Nevada-Goldfield and Mariposa sheets. *Nevada Bureau of Mines and Geology, Map 68*.
- Healey, D.L., Wahl, R.R., and Oliver H.W., 1980, Complete Bouguer gravity map of Nevada-Death Valley sheet. *Nevada Bureau of Mines and Geology, Map 69*.
- Hoffman, L.R. and Mooney, W.D., 1984, A seismic study of Yucca Mountain and vicinity, southern Nevada; data report and preliminary results. *U.S. Geological Survey, Open-File Report 83-588*, 50 pp.
- Kane, M.F., and Bracken, R.E., 1983, Aeromagnetic map of Yucca Mountain and surrounding regions, southwest Nevada. *U.S. Geological Survey, Open-File-Report 83-616*, 19 pp.
- Kennett, B.L.N., 1976, A comparison of travel-time inversions. *Geophys. J. R. astr. Soc.*, **44**, 517-536

- Kennett, B.L.N., and Orcutt, J.A., 1976, A comparison of travel time inversions for marine refraction profiles. *J. Geophys. Res.* **81**, 4061-4070.
- King, J.L., and Tucker, B.E., 1984, Observed variations of earthquake motion across a sediment-filled valley. *Bull. Seism. Soc. Am.* **74**, 137-151.
- MacKenzie, K., McClain, J., and Orcutt, J.A., 1982, Constraints on the crustal structure in eastern Iceland based on extremal inversions of refraction data. *J. Geophys. Res.*, **87**, 6371-6382.
- May, B.T., and Hron, F., 1978, Synthetic seismic sections of typical petroleum traps. *Geophysics*, **43**, 1119-1147.
- McGovern, T.F., 1983, An evaluation of seismic reflection studies in the Yucca Mountain, Nevada Test Site. *U.S. Geological Survey, Open-File-Report 83-912*, 57 pp.
- McMechan, G.A. and Mooney, W.D., 1980, Asymptotic ray theory and synthetic seismograms for laterally varying structures: theory and application to the Imperial Valley, California. *Bull. Seism. Soc. Am.* **70**, 2021-2035.
- Milkereit, B, Mooney, W.D., and Kohler, W.M., 1985, Inversion of seismic refraction data in planar dipping structure. *Geophys. J. R. astr. Soc.*, **82**, 81-103.
- Monfort, M.E., and Evans, J.R., 1982, Three-dimensional modeling of the Nevada Test Site and vicinity from teleseismic P-wave residuals. *U.S. Geological Survey, Open-File-Report 82-409*, 66 pp.
- Orcutt, J.A., Dorman, L.M., Spudich, P.K.P., 1977, Inversion of seismic refraction data. *The Earth's Crust., Geophys. Monogr. Ser.*, vol.20, edited by J.G. Heacock, 371-384.

- Orcutt, J.A., MacKenzie, K., and McClain, J., 1980, The role of  $X(p)$  constraints in linear, extremal inversion of explosion profile data. *Bull. Seism. Soc. Am.* **70**, 2103-2116.
- Orcutt, J.A., 1980, Joint linear, extremal inversion of seismic kinematic data. *J. Geophys. Res.* **85**, 2549-2660.
- Pakiser, L.C., Structure of the crust and upper mantle in the Western United States. *J. Geophys. Res.* **68**, 5747-5756.
- Pakiser, L.C., and Hill, D.P., Crustal structure in Nevada and southern Idaho from nuclear explosions. *J. Geophys. Res.* **68**, 5757-5766.
- Pankratz, L.W., 1982, Reconnaissance seismic refraction studies at Calico Hills, Wahmonie, and Yucca Mountain southwest Nevada Test Site, Nye County, Nevada. *U.S. Geological Survey, Open-File-Report 82-478*, 25 pp.
- Prodehl, C., (1970), Seismic refraction study of crustal structure in the Western United States. *Bull. Geol. Soc. Am.*, **81**, 2629-2646.
- Prodehl, C., (1979), Crustal structure of the Western United States. *U.S. Geological. Surv. Profess. Paper 1034*, 74 pp
- Rogers, A.M., Harmsen, S.C., Carr, W.J., and Spence, W., 1983, Southern Great Basin seismological data report for 1981 and preliminary data analysis. *U.S. Geological Survey, Open-File Report 83-669*, 240 pp.
- Snyder, D.B., and Carr, W.J., 1982, Preliminary results of gravity investigations at Yucca Mountain and vicinity, southern Nye County, Nevada. *U.S. Geological Survey, Open-File Report 82-701*, 36 pp.
- Spengler, R.W. and Rosenbaum, J.G., 1980, Preliminary interpretation of geologic results obtained from boreholes UE25a-4, -5, -6, and -7, Yucca Mountain, Nevada Test



- Site. *U.S. Geological Survey, Open-File Report 80-929*, 33 pp.
- Stewart, J.H., 1980, Geology of Nevada, *Nevada Bureau of Mines and Geology, special publication 4*, 136 pp.
- Sutton, V.D., 1984, Data report for the 1983 Seismic-Refraction Experiment at Yucca Mountain, Beatty and vicinity, southwestern Nevada. *U.S. Geological Survey, Open-File Report 84-661*, 62 pp
- Talwani, M., Worzel, J.L, and Landisman, M., (1959), Rapid gravity computations for two-dimensional bodies with application to the Mendocino submarine fracture zones. *J. Geophys. Res.* **64**, 49-59.
- Telford, W.M., Geldart, L.P., Sheriff, R.E., and Keys, D.A., 1976, Applied Geophysics, *Cambridge University Press, New York*, 860 pp.
- Tucker, B.E., King, J.L., Hatzfeld, D., Nersesov, I.L., 1984, Observations of hard-rock site effects. *Bull. Geol. Soc. Am.*, **74**, 121-136.
- Tucker, B.E., and King, J.L., 1984, Dependence of sediment-filled valley response on input amplitude and valley properties. *Bull. Geol. Soc. Am.*, **74**, 153-165.